DEVELOPMENT AND CHARACTERIZATION OF SALT HYDRATE AND NANOCELLULOSE COMPOSITES FOR THERMAL ENERGY STORAGE

by

Daniel C Blake

A dissertation submitted in partial fulfillment
of the requirements for the degree

of

Doctor of Philosophy

in

Materials Science

MONTANA STATE UNIVERSITY
Bozeman, Montana

December 2025

ACKNOWLEDGEMENTS

I would like to thank the researchers who have helped me with experiments, answered questions or provided valuable discussion – William Otto, Navid Anjum, Sangeet Karna, Saptaparni Chanda, Seth Kane, Hayden Pritchard, Susan Brumfield. Many faculty members have provided me with help and guidance during the research, particularly I would like to thank Doreen Brown and Kathy Campbell. I would like to thank my committee members – Dr. Cecily Ryan, Dr. Erik Grumstrup, Dr. John Kirtley, Dr. Adam Gladen – for their help and guidance throughout my doctorate journey. Finally, I would like to thank my advisor Dr. Dilpreet Bajwa, for his mentorship. This work was sponsored by a grant from the United States Department of Energy: award number DE-EE0009678.

TABLE OF CONTENTS

TABLE OF CONTENTS CONTINUED

TABLE OF CONTENTS CONTINUED

LIST OF TABLES

LIST OF TABLES CONTINUED

LIST OF FIGURES

LIST OF FIGURES CONTINUED

LIST OF FIGURES CONTINUED

LIST OF FIGURES CONTINUED

ABSTRACT

Salt hydrates have demonstrated thermal energy storage capabilities via reversible bonding of water molecules. Materials exhibit an energy density of 400-870 kWh/m^3, operate at low temperatures (<150˚C), are generally low-cost, but are prone to degradation. Previous efforts to improve stability have primarily focused on impregnating a porous host matrix with salt. However, salt expansion during hydration leads to degradation of the host matrix and salt leakage. Cellulose nanocrystals (CNCs) have shown promise in strengthening the structural frameworks of composites across numerous applications. CNCs have generated significant interest due to their high mechanical strength, high aspect ratio, high surface area, liquid-crystalline nature, and hydrophilicity, which support interaction between salt and water. $CaCl_2$, $MgSO_4$, and $SrCl_2$ were employed in the study, as well as several blends of species ($MgSO_4$:$SrCl_2$; $SrCl_2$:$CaCl_2$; $MgSO_4$:$CaCl_2$). Salts and CNCs are combined to produce composites with varying mass ratios (60:40, 80:20, 90:10). Material performance is evaluated using simultaneous thermal analysis. $SrCl_2$:CNC and $SrCl_2$:$CaCl_2$:CNC ($SrCl_2$:$CaCl_2$–90:10) are the most promising materials that were developed based on energy density and uniformity. $SrCl_2$-based formulations possess high energy storage capabilities exceeding 600 J/g and demonstrate unique interactions with CNC through water molecules. CNCs were produced from waste sugar beet pulp (SBP) to develop a more sustainable and cost-effective process. SBPCNC-containing formulations exhibit lower energy density than those using control CNC, attributed to reduced purity, zeta potential magnitude, crystallinity, and a larger aspect ratio. FTIR results indicate that the salt:CNC chemical interaction is mediated by electrostatic forces between CNC and the water molecules of the salt hydrate. The interpretations are supported by Raman spectroscopy, which also indicates unique salt:CNC lattice vibrations and/or CNC effects on water vibrations—the hydrophilic properties of CNC increase drying resistance by binding free water and water molecules in salt hydrates. The composite materials form through mechanical and electrostatic interactions, with strong chemical affinity between the components, which supports material stability.

Keywords: Salt hydrates; Cellulose nanocrystal; Composite development; Thermal energy Storage; Thermochemical material

CHAPTER ONE

INTRODUCTION

The need for reliable, long-term energy has been steadily increasing globally, driving efforts to replace the dwindling fossil fuel resources with sources that may slow the rate of global carbonization. By doing so, the efficiency of energy use in infrastructure may be enhanced either by replacement or the construction of a system in which a combination of energies is employed. Sources such as wind, solar, hydro, and biomass have received significant attention in recent years as the primary methods for decarbonization [1]. However, concerns such as reliability, accessibility, and cost have decelerated the development of these technologies since their emergence [2]. Alternative forms of renewable energy, such as thermochemical systems, have received recent attention as novel means of harnessing energy that can be stored and subsequently released through reversible reactions [3]. Supplementing energy systems with sustainable sources has become a universal effort as the rate of global carbonization increases annually. Numerous nations have prioritized decarbonization efforts to reduce CO_2 emissions.

Thermal energy may be stored via three known pathways: latent, sensible, and thermochemical [4]. Latent storage occurs when energy is drawn from the surroundings to induce a phase change in a material [5]. Sensible storage occurs when the temperature of a material increases due to heat diffusion from its surroundings [6]. These pathways are commonplace but less efficient than thermochemical pathways, which involve chemical reactions that are usually reversible [7]. The benefits of thermochemical energy storage (TCES) include, but are not limited to: greater energy density, long-term storage, and minimal heat loss [7]. Salt hydrates generally undergo reversible thermochemical reactions with water, involving hydration (discharging) and dehydration (charging) [8]. The relationship is represented below by the following equation in

which *A*/*B* is the cation/anion pair, *x*/*y* are the quantities of atoms that form the neutral salt, and *n* is the moles incorporated into the hydrate structure:

Eq.1

$$A_xB_y + nH_2O \leftrightarrow A_xB_y \cdot nH_2O + heat$$

Salt hydrates are not only naturally rechargeable but also rarely hazardous and emit no CO_2. The hydration process results in the incorporation of water molecules into the salt's crystal lattice, which ultimately releases heat as a byproduct of bond formation [9]. The dehydration process requires energy from the surrounding material to break these bonds. The release of heat associated with hydrate formation may be accomplished by simple immersion and solvation of the binary salt, which is often highly soluble [10]. However, TES systems involving these thermochemical materials (TCMs) are more efficiently driven by the *adsorption* of water vapor [11]. The reverse reaction is customarily achieved by evaporation or *desorption*. The storage and subsequent release of thermal energy by these materials is desirable due to high energy density (latent heat per unit volume), small volume change between dehydrated and hydrated phases, relatively high thermal conductivity, and low toxicity [12, 13]. These benefits, along with the mild operating conditions associated with the use of hygroscopic salts for TES, have encouraged more research into the numerous candidates known to exist ($MgSO_4$, CaCl2, SrBr2, etc.) [14]. The energy density of these materials may be defined as the energy produced by the heat released during the complete hydration process per unit volume and is often reported as kWh/m^3 [15]. Factors that are known to affect the energy density of these materials include, but are not limited

to: reaction enthalpy (per mole H_2O), adsorption rate, adsorption capacity, and thermal conductivity [16].

The hydration mechanism of hygroscopic salts has been proposed to occur in 2 key stages: the adsorption of water vapor from the atmosphere onto the material surface, followed by the inclusion of water molecules from the surface into their final lattice positions [17]. It is the second step, which may be defined as rate limiting. Salt hydrates often exhibit intermediate or partially hydrated phases in which a stable lattice forms between the anhydrous and fully hydrated phases [18]. All phases are accessible via water adsorption, but *deliquescence* may occur beyond the fully hydrated phase [19]. Moreover, the deliquescence point varies among salts, so some salt hydrates are more appropriate than others for TES applications based on their water-adsorption properties. The reaction enthalpy, which defines the energy released, is the heat produced by the conversion of salt TCMs from an anhydrous state to their fully hydrated solid state [20]. This is known as the hydration enthalpy (ΔH_{hyd}); initiated by the onset of hydration and terminated by the onset of solvation [21]. ΔH_{hyd} is best determined by hydrating the subject material to the maximum water uptake prior to deliquescence. The hydrated material is then dehydrated by differential scanning calorimetry (DSC) to calculate the energy required to isolate the adsorbed water [22]. Complete hydration of these materials is accelerated by reducing particle size, thereby increasing surface area and creating more adsorption sites [23]. Therefore, it is more beneficial to use salt hydrate crystals with a lower particle size distribution (i.e., submicron) for TES [24].

The interactions between salt ions and water molecules in the formation of hydrated states are most similar to the bonding of ligands to a metal center. The water molecules act as ligands and surround the metal cation of the salt, forming dative bonds, a type of polar covalent bond in which the same atom donates both electrons. These dative bonds form between the oxygen atoms

of water molecules and the metal cation of salts, with the donating atom being the water oxygen [25]. Water molecules also interact with salt hydrates through strong ion-dipole interactions and hydrogen bonding with some anions (e.g., SO_4^{2-}). However, it is dative bonds that establish water molecules as integral parts of the crystal structure. There are two varieties of water molecules in salt hydrates: adsorbed water and crystallized water. Adsorbed water attaches to the surface of salt hydrates by a physical adsorption event and may be detached via heating, whereas crystallized water is bound via dative (and hydrogen) bonding. The ion-dipole interactions assist in the initial coordination of water molecules in salt hydrates, as the partial positive charge of hydrogen in water molecules is attracted to the salt anion, and the partial negative charge of oxygen is attracted to the salt cation. These interactions initially form a hydration boundary around individual salt ions, which eventually become fixed within the solid salt lattice as dative bonds form.

As salt hydrates increase in hydration state, their crystal structures change and are commonly less dense than in the anhydrous state. The materials generally exhibit a noticeable volume change during phase change. However, it is usually lower than that of many organic materials used in thermal energy storage devices (such as paraffin wax or fatty acids) [26]. The expansion is a direct result of the density difference between the hydrated and anhydrous phases of the salts, as water molecules occupy space within the newly formed crystal structure. The extent of the volume change may be approximated from differences in molar mass and density between the anhydrous and hydrated states, and varies among salts. For example, the volume change in $CaCl_2$ is reported as high as 15% (from anhydrous to hexahydrate) while the volume change of KF_2 is reported as only 0.55% (from anhydrous to tetrahydrate) [27]. Moreover, the expansion of crystal structure can be an issue in applications such as TES, as repeated stress from these volume changes can cause salts to break down via swelling, cracking, and, in some cases, pulverization.

These physical changes are known to reduce the TES performance of salt hydrates by creating a less efficient structure for heat transfer and diffusion, ultimately decreasing energy storage capacity over long-term cycling [28].

Research has attempted to address these issues by developing composites that better withstand volumetric changes and resist physical degradation, thereby improving the long-term stability of salt hydrates in TES. These materials may be confined and stabilized in a host matrix or composite structure to mitigate these issues, which can be achieved through external or internal structural support. For example, Zhou et al. reported a composite system comprising $Al_2(SO_4)_3 \cdot 18H_2O$ and $FeSO_4 \cdot 7H_2O$, stabilized with carbon nanotubes (CNT). After 100 dehydration cycles, the particles containing CNT did not exhibit any volume expansion or cracking, whereas the particles without CNT did [29]. The stabilizing effect was attributed to the formation of a network of CNT throughout the salt blend. These findings emphasize the benefits of developing salt hydrate composites with an internal stabilizing network rather than an external one (e.g., encapsulation or a porous host matrix). Ideally, composites should exhibit high heat storage density, low volume expansion during phase change, chemical stability, and energy savings. Additionally, materials should be odorless, nontoxic, and nonflammable. The purpose of composites is to address the shortcomings of salt hydrates alone when it comes to thermal energy storage, particularly material cycling.

Salt hydrates have demonstrated thermal energy storage (TES) capabilities via reversible bonding of water molecules. Materials are generally low-cost and exhibit high energy density via reaction with an abundant resource, but are prone to degradation over use. The development of composites using various additives has been explored to produce TES materials with greater stability during hydration-dehydration cycles. The creation of salt TCM composites has developed

as a means to enhance energy output and cycling stability by increasing the surface area of the salt crystals and offering structural support [30]. Previous efforts to extend the stability of salt hydrates have primarily focused on impregnating salt into a porous, rigid host matrix (e.g., activated carbon foam) [31]. However, the expansion of salts during hydration has led to degradation of the host matrix and salt leakage [32]. It has also become apparent that diffusion of water within these porous composites is limited by the quantity and size of pores [32]. Although the use of these frameworks for TES materials has improved characteristics such as adsorption/desorption rates and stability, the long-term stability desired is still not achieved, and energy density is even reduced due to lower adsorption enthalpies of the host matrices [33, 34]. Impregnation of CNC into salt TCMs may fully expose and even enhance the number of adsorption sites by increasing the material's surface area. Therefore, the addition of CNC is hypothesized to enhance salt performance while minimizing reductions in energy density.

CNCs are nanoparticles commonly extracted from woody biomass via acid hydrolysis methods [35]. These nanomaterials have generated significant interest in recent years due to their high mechanical strength, high aspect ratio, high surface area, and liquid-crystalline nature [36]. CNCs may also undergo chemical surface modification to adjust their properties [37]. For these reasons, CNC has been selected as a nucleation agent for the formulation of salt:CNC composite materials for TES. The dimensionality of CNCs makes them suitable for use as nucleation agents, with an average width of 5-20 nm and a length of 100-600 nm [38]. Its water-stable crystalline form allows reliable nucleation of salt crystals while providing structural support to prevent deliquescence [39]. Moreover, CNC provides additional assistance to salt hydrates by enhancing material hydrophilicity, which may increase adsorption rates and/or induce adsorption at lower RH

[40]. For these reasons, CNC is used to promote nanoscale crystal growth of TCMs and to improve their stability and water-uptake capacity.

Furthermore, the use of CNC maintains the low toxicity of study materials and provides an opportunity to produce a high-value product from otherwise waste organic matter [41, 42]. The addition of CNC further supports sustainability by using renewable materials. Lastly, optimizing materials for climate regulation has significant potential to conserve energy and reduce costs. Cellulose nanocrystals (CNCs) have shown promise for strengthening structural frameworks in composites across a broad range of applications. Additionally, the hydrophilicity of CNCs enhances salt performance by facilitating interactions with water. It is suggested that TES capacity and stability of salt hydrates may be improved by CNC impregnation.

The material function of salt:CNC composites is based on the energy storage capacity of the salt hydrate component, whereas the CNC serves as a structural support to maintain cycling stability. The hydrophilicity of CNC is also expected to enhance the diffusion of water molecules, thereby improving the maximum TES capacity of the salt fraction. Lastly, CNC is characterized by a water-stable crystalline form, so nucleating the salt crystals with CNC provides deliquescence resistance during water uptake by preventing total loss of crystal structure. Electrostatic interactions between salt ions and CNC result in the formation of an electrical double layer of salt ions around CNC particles. Therefore, there is a persistent internal network that aids structural support and prevents material degradation (i.e., salt deliquescence). These discoveries are especially evident in salts that are particularly prone to deliquescence, such as $CaCl_2$, and extend the cycling stability of additional salts, such as $SrCl_2$. Moreover, material strengths include eliminating salt leakage concerns by exploiting an internal structural support matrix rather than an external one (i.e., expanded graphite). Still, these composite materials pose several real-world

challenges that remain to be addressed, such as slow reaction kinetics, low thermal conductivity, and the identification of an appropriate reactor. The slow reaction kinetics between the salt and water vapor are primarily due to the formation of a passivating layer of the hydrated phase on the surface of the concealed anhydrous salt, which creates a barrier that slows further hydration. It then becomes essential for additional water vapor to diffuse beyond the hydrated surface layer to reach the unreacted salt beneath, and the kinetics of this diffusion are known to be much slower than the surface reaction [43]. Therefore, the material system requires more time to store and release heat and can even lead to an incomplete conversion of salts to their fully hydrated form (i.e., maximum heat release). There can also be a significant difference in the temperatures and/or pressures required to hydrate and dehydrate materials, depending on the salt, which can limit overall TES efficiency. The solid-gas reaction may be hindered by slow diffusion of water molecules within salt particles and/or poor thermal conductivity. Lastly, many salt hydrates are known to be corrosive and can damage reactor components, depending on the system [44]. For these reasons, it is important to identify the ideal materials and reactor to achieve the highest performance of salt hydrates for TES.

To reemphasize, salt hydrates are attractive materials for TES but have shown rapid loss of energy density after use (e.g., hand warmers). Therefore, the development and optimization of salt-based composites are necessary to achieve acceptable efficiency and lifespan for these rechargeable systems. The combination of salt hydrates and CNCs has not been investigated under the lens of TES by other research groups before, to our knowledge. The performance of new salt blends is also investigated during composite development. The primary objective is to extend the TES lifetime of high-performing salt hydrate by impregnating salt crystals with CNC. The ability of CNC to optimize energy storage and release of salt hydrates provides additional value to the

study. Simultaneous objectives are to identify and develop promising salt:CNC candidates that offer stable, long-term energy storage (90% thermal reliability over 5000 cycles), high energy density (≥250 kWh/m^3), and increased adsorption rate for climate regulation. In addition, the study aims to establish a novel application of CNC by harnessing its structural and hydrophilic properties to enhance energy storage capabilities. Process sustainability and cost reduction are demonstrated by using sugar beet pulp (SBP) waste as feedstock for CNC production provided by American Crystal Sugar.

The novelty of the work lies in using cellulose nanocrystals as an internal framework to stabilize salt hydrates during hydration-dehydration cycles, a strategy that, to our knowledge, has not been attempted before. It is found that the salt:CNC composites can extend the cycling stability of salt hydrate TES more than any other composite tested so far. Moreover, salt:CNC composites are characterized using various analytical techniques to understand component interactions better and optimize material performance. Although other salt hydrate composites have been developed to address the previously discussed challenges, there is little research on the interactions among composite components. The data and interpretations presented in this work provide a more thorough understanding of how salt hydrates may be stabilized during long-term cycling and elucidate how CNC contributes to salt hydrate TES performance. The research schematic begins by identifying promising salt hydrates and salt blends for thermal energy storage. These salts are then used in composite development with cellulose nanocrystals to form materials to be tested alongside salt controls. Material testing includes quantifying dehydration enthalpy as a measure of energy density and cycling materials to determine whether CNC impregnation extends the performance lifetime. The composites are then characterized using various analytical techniques to determine how CNC affects the performance of salt hydrates in TES.

CHAPTER TWO

SALT HYDRATE BIO-COMPOSITES FOR THERMAL ENERGY STORAGE: A CONCISE REVIEW

Contribution of Authors and Co-Authors

Manuscript in Chapter 2

Author: Daniel Blake

Contributions: Investigation, Analysis, Writing – Original draft, Visualization

Co-Author: Adam Gladen

Contributions: Supervision, Writing – Review, Editing

Co-Author: Dilpreet Bajwa

Contributions: Supervision, Writing – Review, Editing

Manuscript Information

Daniel Blake, Adam Gladen, and Dilpreet Bajwa

Reviews on Advanced Materials Science

Status of Manuscript:
_____ Prepared for submission to a peer-reviewed journal
_____ Officially submitted to a peer-reviewed journal
_____ Accepted by a peer-reviewed journal
__X__ Published in a peer-reviewed journal

Publisher: Journal of Energy Storage; 133:117874, DOI: https://doi.org/10.1016/j.est.2025.117874

Abstract

As global energy demand increases, there is a concerted effort to replace expensive and hazardous sources with renewable energy systems. In 2022, the U.S. reported total energy use of approximately 100.4 quadrillion BTUs, with buildings accounting for a significant share (29%). In response, the energy sector has faced challenges in reducing costs and extending the lifespans of sustainable energy storage devices. Salt hydrates have demonstrated thermal energy storage (TES) capabilities via the thermochemical pathway, through reversible bonding of water molecules, and the latent pathway, through reversible melting and crystallization. Promising candidates have demonstrated energy densities ranging from 400 to 870 kWh/m^3 and low operating temperatures <150˚C, but are prone to degradation with use. The development of composites using various additives has been explored to produce TES materials with greater performance stability. The provided review focuses primarily on TES enhancement in salt hydrate-based composites using additives derived from biological sources (bio-composites). The bio-based additives discussed include activated carbon, cellulose nanofibrils, cellulose nanotubes, cellulose nanospheres, and cellulose nanocrystals. The benefits and shortcomings of bio-composites are investigated and compared to elucidate how salt hydrate TES may be enhanced through an environmentally friendly approach. The review also highlights novel applications of biomaterials and their contributions towards a more sustainable future. Various properties related to TES performance are discussed, such as phase and cycling stability, hydration ability (hydrophilicity), energy storage capacity, and thermal conductivity.

Keywords: Salt hydrates; Biomaterials; Carbon nano additives; Composite development; Thermal energy Storage; Thermochemical material

Abbreviations

AC	Activated carbon
ACF	Activated carbon foam
ACP	Activated carbon particle
C_{60}	Carbon 60
CMC	Carboxyl methyl cellulose
CMF	Cellulose microfiber/fibril
CNC	Cellulose nanocrystal
CNF	Cellulose nanofiber/fibril
CNT	Carbon nanotube
CNS	Carbon nanosphere
CO	Coconut oil
DSC	Differential scanning calorimetry
DSP	Disodium phosphate
FTIR	Fourier transform infrared spectroscopy
LES	Latent energy storage
MWCNT	Multi-walled carbon nanotube
MCNC	Metal-grafted cellulose nanocrystal
MAH	Maleic anhydride
NP	Nanoparticle
PCF	Phase change fiber
PCM	Phase change material
PEG	Polyethylene glycol
PS	Polystyrene
PW	Parrafin wax
RH	Relative Humidity
SAT	Sodium acetate trihydrate
SES	Sensible energy storage
SWCNT	Single-walled carbon nanotube
TCES	Thermochemical energy storage
TCM	Thermochemical material
TES	Thermal energy storage
TGA	Thermogravimetric analysis
wt.	weight

Symbols

C_p	Heat capacity
ΔH_o	Standard reaction enthalpy per mole
ΔH_c	Crystallization enthalpy
ΔH_m	Melting enthalpy
p_o	Standard pressure
p_{eq}	Equilibrium partial pressure
R	Ideal gas constant
ΔS_o	Standard reaction entropy per mole
T	Temperature
T_c	Crystallization temperature
T_m	Melting temperature
T_s	Solidification temperature

Introduction

As demand for reliable, long-term energy has increased, efforts are underway to replace dwindling fossil fuels with resources that may slow the rate of global carbonization. The development and application of renewable energy have become increasingly necessary to displace reliance on environmentally hazardous sources (e.g., petroleum) or to minimize use by supplementation [45]. Sources such as wind, solar, hydro, and biomass have received significant

attention as primary methods for decarbonization. However, they are met with concerns of reliability and accessibility in addition to cost and the need for storage [46]. Thermal energy storage development has primarily focused on phase changing and thermochemical systems [47]. However, thermochemical energy storage systems have received more recent attention as novel means of harnessing energy by reversible reactions [48]. There is great potential in the energy density that can be generated per unit volume of material, which eases cost constraints. Still, materials that can operate under mild conditions are needed to address the remaining concerns.

Salt hydrates have become an attractive material for use in thermochemical systems due to their ability to store latent energy through a reversible reaction with water [49]. The thermodynamics of the adsorption and bonding of water to these materials is similar to transitions such as freezing and melting. However, temperature has an inverse effect: as the material (or its environment) cools, the condensation or adsorption of atmospheric water vapor onto the material's surface is encouraged. Adsorption of water may also be driven by the surrounding relative humidity (RH). The hydration process occurs by incorporating water molecules into the salt crystal lattice, which ultimately releases heat as a product of bond formation [49]. The dehydration process requires energy from the surrounding material to break these bonds, which can be provided by heating. The storage and release of thermal energy by these materials is desirable due to high energy density (heat per unit volume), small volume change between dehydrated and hydrated forms, and low toxicity [49]. These benefits and mild operating conditions have encouraged broad research into the numerous candidates known to exist ($MgSO_4$; $CaCl_2$; $SrBr_2$; etc.) [50].

In addition to investigating individual salts, the fabrication of composites has advanced to enhance energy output and cycling stability, primarily by reducing salt crystal aggregation and providing structural support [51]. Most TES salt hydrate composite research has employed an inert,

porous host matrix to provide submicron pockets for crystallization [51]. Although the use of these frameworks in TES materials has improved characteristics such as water uptake/release rates and rechargeability, complications in other important properties remain (energy density, deliquescence, etc.) [52]. Investigations into ideal materials and other methods to improve the use of salt hydrates in TES systems continue; the current state of the field and knowledge are discussed, particularly recent technological developments in composites.

TES Pathways

Thermal energy may be stored via three known pathways: latent, sensible, and thermochemical [46]. Latent energy storage (LES) is expressed when energy is drawn from the surroundings to induce a phase change in a material. Sensible energy storage (SES) is expressed when the temperature of a material is raised by the diffusion of heat from its surroundings. These pathways are common but less promising than thermochemical energy storage (TCES), which involves a reversible chemical reaction that can produce heat. Among these reactions that offer TCES, there is a subcategory that may operate via the adsorption of gaseous species, such as water vapor. Salt hydrates exhibit the process via water adsorption [49]. The benefits of TCES include:

1. Greater energy density
2. Long-term storage
3. Minimal heat loss

Although TCES is the most promising method for TES, the vast majority of modern research has focused on LES systems, mainly because of their simpler design. An LES system comprises three primary components: a phase change material (PCM), a container for the PCM, and a heat-exchange surface between the PCM and the heat source/sink [52]. PCMs are materials that undergo

a phase transition. However, PCMs of interest are limited to materials that exhibit a solid-liquid phase transition at moderate operating conditions (< 100°C). The main advantages of PCMs include:

1. High energy storage density
2. Short temperature operating range – constant temperature during phase transition
3. Vast range of materials to tailor properties to specific applications (i.e., organics, inorganics, eutectics)

The superior popularity of PCMs is mainly due to the third advantage. The review presented here discusses research focused on the development of salt hydrate-based PCMs. SES systems are the simplest but are highly dependent on specific heat and perform poorly during long-term storage [53]. Salt hydrates also provide considerably greater energy density via TCES and LES pathways. Therefore, salt hydrate composites operating via the SES pathway are barely discussed.

In TCES, hygroscopic salts undergo reversible thermochemical reactions with water, involving hydration (discharging) and dehydration (charging). The relationship is represented by the following equation in which the variables *A* and *B* are the cation/anion pair, *x* and *y* are the quantities of atoms that form the neutral salt, and *n* is the moles incorporated into the hydrate structure:

Eq.1

$$A_xB_y + nH_2O \leftrightarrow A_xB_y \cdot nH_2O + heat.$$

The release of heat associated with hydrate formation may be accomplished by simple immersion and solvation of the binary salt, which is often highly soluble [54]. However, TES

systems involving these thermochemical materials (TCMs) are more efficiently facilitated via *the adsorption* of water vapor [50]. The reverse reaction is customarily achieved by evaporation or *desorption*. TCES is not only the optimal pathway for TES due to the previously stated benefits; the possibility of storing energy at near-ambient conditions with minimal hazards has enhanced the value of salt TCMs [55]. However, TCES systems have encountered drawbacks in maintaining energy storage over long-term use (the repetitive reversible reaction of *Eq. 1*). Salt hydrate TCMs are prone to material degradation or deliquescence between hydration cycles, which occur when the adsorbed moisture is sufficient to transform the solid material into a solvated liquid. It is a challenge to develop a salt TCM system that addresses concerns about loss of material quality over extended use.

In LES, hygroscopic salts may be present in either the solid or dissolved state. The process that defines energy storage in solid form is the melting transition. As salt transitions from solid to liquid with the introduction of heat, energy is stored through an endothermic process. Consequently, energy is released during the exothermic transition from liquid to solid, otherwise known as freezing. The process that defines the energy storage and release for hygroscopic salts in solution is the crystallization transition. When salt dissolves in water, energy is often released through the exothermic process of breaking its crystal structure. Therefore, the crystallization of aqueous salt drives the storage of thermal energy through conservation of energy. Salt PCMs have received considerable focus in modern research, especially in the composite realm. However, the materials exhibit the same drawbacks as salt TCMs during long-term use (repetitive phase transition cycles). Salts hydrates lack the structural integrity to retain the latent energy of the original crystal structure between phase changes and are therefore not suited for extended use. Salt PCMS are also known to experience supercooling and sedimentation issues when in solution.

Supercooling phenomena may occur when a highly soluble salt is dissolved, which discourages the formation of its crystal structure. The output of heat does not occur at the desired temperature or is delayed as a result. Sedimentation phenomena may occur when moderately soluble salt is dissolved at a concentration approaching its maximum solubility. Under these circumstances, dissolved particles tend to flocculate and sediment, causing phase instability in the salt solution. The reduction in dissolved particles results in a loss of energy storage during the crystallization transition.

Adsorption – TCES Pathway

Adsorption in salt TCMs involves the binding or condensation of vapor onto a solid substrate and is accompanied by the simultaneous release of energy via the formation of chemical bonds [56]. The energy capacity is defined by the chemical potential associated with bond formation [57]. The laws of thermodynamics govern the direction of a reaction and are a combination of enthalpic and entropic effects, with enthalpy correlated to the given chemical potential [58]. Hygroscopic salts often exist in hydrated form due to atmospheric humidity, in which the materials in the subclass reach equilibrium with surrounding water vapor. For example, Sogütoglü et al. reported in 2019 on the adsorption performance of various salts that exhibit reversible hydration behavior, such as $CuCl_2$, K_2CO_3, $MgCl_2$, and LiCl [59]. The experiment (performed at a vapor pressure of 10 mbar) provided evidence of earlier hydration in LiCl and $MgCl_2$ than in K_2CO_3 and $CuCl_2$ when cooled from 65°C to room temperature. These differences in salt hydrate TCMs, among others (e.g., energy density), require careful investigation of what is available to determine the materials best suited for TES. Adsorption in salt hydrate TCMs enables heat release from the induced crystal transformation. Many compounds within the subclass also

experience intermediary or partially hydrated phases in which there is a stable lattice formed between the anhydrous and fully hydrated phases. All phases are accessible through adsorption of water vapor, but risk *deliquescence* beyond the fully hydrated phase [55]. The deliquescence point, in terms of relative humidity (RH) and water uptake, has been known to vary between hygroscopic salts. In 2018, Sato and Hattanji reported on the varying deliquescence (v. RH) of several rock types containing differing salts: NaCl, Na_2SO_4, and $MgSO_4$ [60]. The practical deliquescence relative humidity (DRH) at 20°C was found to be 75.6% for NaCl, 83.3-95.1% for Na_2SO_4, and 92.7% for $MgSO_4$. However, the study also reported that NaCl has a greater water-uptake capacity than both sulfate salts, due to a lower relative viscosity after solvation. The impact of increased viscosity post-deliquescence slows the rate of hydration results and ultimately leads to less adsorption over time.

The hydration mechanism of hygroscopic salts has been proposed to occur in 2 key stages [61]:

1. Adsorption of water vapor from the atmosphere onto the salt surface
2. Inclusion from the surface to the final lattice position

It is the second step, which may be defined as rate-limiting: the adsorption of water onto $MgSO_4$ and Na_2SO_4 had slowed significantly following the initial hydrating phase. The equilibrium partial pressure (p_{eq}) defines the threshold concentration of water vapor to initiate adsorption and is determined by the following equation in which p_o is standard pressure (Pa), R is the ideal gas constant (J mol^{-1} K^{-1}), T is temperature (K), and $\Delta S_o/\Delta H_o$ are the standard reaction entropy and enthalpy per mole of water [62]:

Eq.2

$$p_{eq} = p_o \exp(-\Delta S_o/R)\exp\,(\Delta H_o/RT)$$

Complete hydration of these materials is accelerated by reducing particle size, thereby increasing surface area and creating more adsorption sites [63]. Therefore, it is beneficial to use salt hydrate crystals with a low particle size distribution (i.e., submicron) for TES.

Mechanism of Energy Release

The energy density of these materials may be defined as the energy per unit volume quantified by the heat released during complete hydration or a phase transition, and is often reported in kWh/m^3. For TCMs, factors known to affect the energy density of materials include, but are not limited to: reaction enthalpy (per mole H_2O), adsorption rate, adsorption capacity, and thermal conductivity [63]. The energy density of various common salt TCMs is shown in *Table 2.1*. The mechanism of energy release in top-performing salt TCMs begins with exposure to water, typically via the adsorption of atmospheric vapor. These materials have also been known to reversibly adsorb other gaseous species, such as CO_2 and NH_3, but have not shown as much potential as their relationship with H_2O for energy storage [64, 65]. H_2O and NH_3 are known as chemical sorbents in relation to salt TCMs and are characterized by large reaction enthalpies [66]. The use of H_2O has been more common in salt-based TES systems due to familiarity and encouraging preliminary results across a wide range of materials. The nonhazardous nature of water provides even more reasoning to investigate these salt/H_2O systems as well.

The reaction enthalpy, which defines the energy released, is the heat produced by the conversion of salt TCMs from their anhydrous state to their fully hydrated solid state. This is known as the hydration enthalpy (ΔH_{hyd}), which spans the onset of hydration (initiation) and the onset of solvation (termination) [67]. Rammelberg et al. showed the variety in ΔH_{hyd} values

between CaO, $CaCl_2$, and $MgCl_2 \cdot 2H_2O$ via dual TGA/DSC analysis [67]. The pre-hydrated materials were exposed to a constant vapor pressure of 19 hPa and a constant temperature of 30°C, which allowed the enthalpies of each transition to be measured. Complete hydration was achieved upon the plateau of mass. The respective ΔH_{hyd} values were reported as follows: CaO = 1823 J/g; $CaCl_2$ = 2629 J/g; $MgCl_2 \cdot 2H_2O$ = 1551 J/g. Notably, $CaCl_2$ continues to prove its value as a component of TCMs and will be further discussed.

Table 2.1 Corresponding energy densities of common hydration steps in popular salt hydrates for TES [19]

Salt Hydrate	Hydration Step	Energy Density (kWh/m^3)
$CaCl_2 \cdot 6H_2O$	$CaCl_2 \cdot H_2O + 5H_2O \rightarrow CaCl_2 \cdot 6H_2O$	601
$LaCl_3 \cdot 7H_2O$	$LaCl_3 \cdot H_2O + 6H_2O \rightarrow LaCl_3 \cdot 7H_2O$	591
$MgCl_2 \cdot 6H_2O$	$MgCl_2 \cdot 4H_2O + 2H_2O \rightarrow MgCl_2 \cdot 6H_2O$	307
$MgSO_4 \cdot 7H_2O$	$MgSO_4 \cdot H_2O + 6H_2O \rightarrow MgSO_4 \cdot 7H_2O$	558
$SrBr_2 \cdot 6H_2O$	$SrBr_2 \cdot H_2O + 5H_2O \rightarrow SrBr_2 \cdot 6H_2O$	628

For PCMs, factors known to affect the energy density of materials include, but are not limited to, crystal nucleation rate, crystal growth rate, specific heat, thermal conductivity, and congruent v. incongruent melting. Congruent melting of hygroscopic salts occurs when the salt is soluble in its hydrated water at melting. In contrast, incongruent melting occurs when the salt is not fully soluble in its water of hydration at the melting point. Semi-congruent melting may also occur, in which the solid and liquid phases during melting have different compositions due to the transformation of salt hydrates to less-hydrated forms (such as $MgCl_2$ in *Table 2.1*). The energy density of various common salt PCMs is shown in *Table 2.2*. The mechanism of energy release, as previously described, is initiated by material cooling. The solid-liquid transition is most popular because of its minimal volume change between phases and its lower transition temperature than other phase transitions, such as liquid-vapor or liquid-gas. Solid-solid transitions are common among salt hydrates but are known to have a lower transition energy than the heat of fusion. The

enthalpy of fusion, which defines the energy released, equals the heat transferred to the surroundings as the PCM transitions from liquid to solid. Consequently, thermal energy is stored when heat is supplied to a PCM, causing it to change state from solid to liquid. The PCMs should be included in the review, as significant research has been published on the development of PCM composites using bio-based components, such as cellulose derivatives. However, the primary focus of the discussion is given to TCMs for the aforementioned advantages.

Table 2.2 Corresponding melting point and enthalpy of common PCMs for TES [68]

Material	Melting Point (°C)	Melting Enthalpy (kWh/m^3)
Water	0	85.1
$CaCl_2 \cdot 6H_2O$	30	59.4
$NaCH_3CO_2 \cdot 3H_2O$	58	106.7
$MgCl_2 \cdot 6H_2O$	117	65.4
$Na_2SO_4 \cdot 10H_2O$	32	74.3

Materials

Pure Salts and Salt Blends

The basis for all thermochemical salts that are still common in research today is their associated energy density and material cost. N'Tsoukpoe et al. performed an exceptional screening of popular salt TCMs in 2014, which remain heavily involved in research today [69]. The study initially evaluated 125 different salt hydrate materials for household/commercial use, including their safety, toxicity, flammability, and other significant hazards. The primary screening had reduced the initial list from 125 compounds to 45. The remaining candidates were further evaluated using basic TGA techniques to verify the reversibility of dehydration. The secondary screening had further reduced the list of potential candidates from 45 to 17. These 17 promising candidates among modern salt TCM research include: $Al_2(SO_4)_3 \cdot 18H_2O$; $CaBr_2 \cdot 6H_2O$; $CaCl_2 \cdot 6H_2O$;

$Ce(SO_4)_2 \cdot 4H_2O$; $K_2CO_3 \cdot 1.5H_2O$; $KOH \cdot 2H_2O$; $LaCl_3 \cdot 7H_2O$; $La(NO_3)_3 \cdot 6H_2O$; $LiCl \cdot H_2O$; $LiNO_3 \cdot 3H_2O$; $MgBr_2 \cdot 6H_2O$; $MgCl_2 \cdot 6H_2O$; $MgSO_4 \cdot 7H_2O$; $Na_2S_2O_3 \cdot 5H_2O$; $SrBr_2 \cdot 6H_2O$; $SrCl_2 \cdot 6H_2O$; $Zn(NO_3)_2 \cdot 6H_2O$. These salts exhibit significant reversibility between hydrated and dehydrated phases at 100°C and therefore meet the necessary criteria for use in TES systems. Additional salt hydrates may also demonstrate proper behavior for use as TCMs [70]. However, the aforementioned materials have been most commonly reported in studies and continue to be investigated individually or in composite systems to optimize their use [71].

Recently, the formation of salt blends from promising TES candidates has enabled the tailoring of desired material properties, such as thermal stability, deliquescence conditions, and energy density. Li et al. demonstrated the technique in 2020 by developing a $MgSO_4$:$SrCl_2$ composite salt for low- to mid-temperature TES [72]. $MgSO_4$ tends to deter water adsorption by forming a viscous film on the material surface, leading to incomplete hydration and reduced adsorption capacity. $SrCl_2$ exhibits exceptional properties for TCM applications and operates at optimal conditions (<100°C), but it is not nearly as cost-effective. The investigation concluded that the composite salt showed overall improved performance. Compared with the individual salts, $MgSO_4$:$SrCl_2$ (20:80) exhibited higher water uptake, a lower desorption temperature, and a higher energy density, while reducing material cost. Additionally, the salt blend demonstrated improved stability between hydrated and dehydrated states, maintaining 75.1% of its original heat storage capacity after 20 cycles, outcompeting the pure components.

Since their initial realization, many investigations into the performance of salt hydrates as TES materials have successfully narrowed the options to a few suitable for applications. Although the energy density among promising candidates is acceptable, as are the operating conditions, the primary concern that remains is the reduction in energy density between cycles or material

degradation [73]. A secondary concern is the thermal conductivity of the final product [74]. As reported by Li et al., the stability of salt TCMs can be extended by forming a composite material comprising multiple components. The $MgSO_4$:$SrCl_2$ composite salt shows promise for material development among known salt hydrates that may function as TES materials, but still demonstrates a significant reduction in heat storage capacity over repeated cycling. An array of novel research since then has delved into the formation of various salt-composite TCMs containing components that may provide additional structure, such as porous host matrices or nucleation/thickening agents [75]. The review that follows focuses on studies in which the performance of salt PCMs and TCMs has been improved by combining them with a component sourced from biological materials (*biocomposite*). Attention has been given to bio-composites because of their contributions to sustainability and hazard prevention, as well as reducing material costs [76].

Bio-based Composites

The development of composite TCMs using hygroscopic salts has opened many new avenues of research for optimizing material performance. The benefits of these composites may include, but are not limited to: degradation resistance and reduced phase segregation, enhanced thermal conductivity, increased specific surface area, prolonged cycling stability, and additional options for material property tuning [77]. The main disadvantage of composite formation is the resulting reduction in energy density due to the introduction of a non-salt component. Material types such as porous host matrices can provide energy by simply adsorbing or condensing water vapor [78]. However, the primary energy density contribution of the resulting TCM is still limited by the salt mass percentage in the final composite. The use of porous host matrices to produce salt composites for TES has introduced additional complications, including reduced water vapor

adsorption and diffusion kinetics due to elevated viscosity at the material surface; salts may also cause pore destruction as they expand during hydration [79]. Porous matrices are briefly discussed due to the popularity of the method for composite formation, but only those that may be sourced from biological means. The remaining composites reviewed use novel additives and techniques to enhance the stability of salt TCMs and resist deliquescence or phase separation. The influence of these methods on other important properties, such as thermal conductivity and adsorption kinetics, is also discussed.

Activated Carbon

Research presented by Druske et al. uses two methods of salt impregnation to infuse the pores of activated carbon foam (ACF) [80]. The subjected salts include $CaCl_2$ (anhydrous), $CaCl_2 \cdot 6H_2O$, and KCl, as well as several combinations of $CaCl_2$:KCl in varying mass ratios (2:1; 1:1; 1:2). Salt impregnation was accomplished by 'soaking' of host matrices in molten salts or 'wet impregnation' via saturation of host matrices by an aqueous salt solution under vacuum. The results show a direct relationship between impregnation success and the impregnating medium: immersion of the host matrix in molten salt achieved a higher salt content in the final composite than immersion in aqueous salt, or 'wet impregnation'. However, ACF could achieve only a maximum salt content of 63 wt% due to its open-pore structure, which allows salt leakage during impregnation and drying. The relatively low salt content reduced energy density and hindered water uptake/release compared with $CaCl_2$. Activated carbon may also be used as an internal component rather than an external one in TCM composites. For example, Yang et al. investigated the use of activated carbon particles (ACP) as an additive to salt hydrates to enhance the thermal stability, conductivity, and adsorption capacity of LiOH (monohydrate) [81]. Notably, ACP was

found to improve water uptake and thereby increase energy storage relative to pure LiOH. The results and properties of these salt-based composites with activated carbon are compared in Table *2.3*.

Thermophysical Properties

Although wet impregnation did not achieve higher salt content in resulting composites, the matrices submerged in molten salt experienced the least efficient adsorption kinetics. The phenomenon is best explained by partial pore blocking. The soaking method may allow deeper penetration of salt, but it can overfill (or, in some cases, seal) the pores of the host matrix, reducing water vapor diffusivity. The main benefit of ACF is increased heat conduction. The thermal conductivity of $CaCl_2$/ACF is 1.03 W/m·K, while the value is reported as 0.54 W/m·K for $CaCl_2$ and 0.55 W/m·K for ACF. LiOH/ACP is also characterized by increased thermal conductivity, but it is not as significant as the enhancement in $CaCl_2$/ACF because the conductivity of pure LiOH was reported as 1.69 W/m·K. However, using ACP offers greater benefit as an additive in salt TCMs because of its ability to greatly enhance water uptake (and energy storage) while providing some improvement in thermal conductivity. These findings further support the focus on internal additives rather than an external matrix (i.e., ACF).

Table 2.3 Comparison between salt-based composites using ACF and ACP additives.

Additive	Salt	Salt Mass %	Energy Storage	v. Pure Salt	Conductivity	Water Uptake	Reference
ACF	$CaCl_2$	63%	701 J/g	~68% ↓	1.03 W/m·K	~61% ↓	Druske
ACP	LiOH	50%	1236 J/g	~87% ↑	1.72 W/m·K	6% ↑	Yang

Micro & Nano-Fibrillated Cellulose Composites

Cellulose nanofibrils (CNF) and microfibrils (CMF) can form entangled fiber networks and gel above their critical concentrations. The introduction of CNF/CMF to salt hydrate slurries has aided in preventing phase separation in another form of TES via phase change materials (PCMs) by increasing viscosity and contributing a structural framework [82]. PCMs release and store energy via LES, which facilitates energy storage through a physical state transition (e.g., melting/crystallization). The investigation of particularly CNF in stabilizing salt dispersion by inducing gelation has been pursued by many researchers in recent years. CMF is not as effective as CNF at providing phase stability due to fewer fiber entanglements and, consequently, less sedimentation prevention. For example, Oh et al. in 2020 revealed the ability of CNF and CMF to provide phase stability in a saturated solution of sodium acetate trihydrate (SAT) at concentrations upwards of ~0.8 wt% using CMF and ~0.6 wt% using CNF [82]. These limits were determined by visual observation, in which the thickening effects of CMF and CNF were displayed.

Fibrillated cellulose has been used in similar SAT PCM systems, with additional additives to enhance heat conduction or nucleation. Shen et al. fabricated a PCM system in which CNF was added to reduce supercooling and enhance phase stability, silver nanoparticles (AgNPs) were added to enhance thermal conductivity, and Na_2HPO_4 (DSP) was added to reduce supercooling further [83]. It should be noted that composites containing AgNPs were prepared by a combination of 0.5wt% CNF suspension (100g) and $AgNO_3$ solution of varying concentration (0.01, 0.02, 0.03 M) to infuse AgNPs and CNF. $NaBH_4$ was then added to CNF/$AgNO_3$ mixtures to yield CNF/AgNPs. Research by Li et al. developed a similar SAT PCM system, adding carboxymethyl cellulose (CMC) as a thickening agent and Al_2O_3 nanoparticles as a nucleation and thermal-

conductivity agent. However, no thermal conductivity measurements were reported, and KCl was used as a secondary nucleation agent to reduce SAT supercooling [84]. The results of these studies are compared in *Table 2.4.*

Table 2.4 Comparison between SAT-based composites using CNF or CMF additives.

Thickening Agent	Nucleation Agent	Metal NP	Supercooling	Reference
0.8% CNF; 0.6% CMF	-	-	2.9˚C	Oh et al.
1.0% CNF	2.0% DSP	0.077-0.296% Ag	1.2˚C	Shen et al.
4.0% CMC	8.0% KCl	1.0% Al_2O_3	0.1˚C	Li et al.

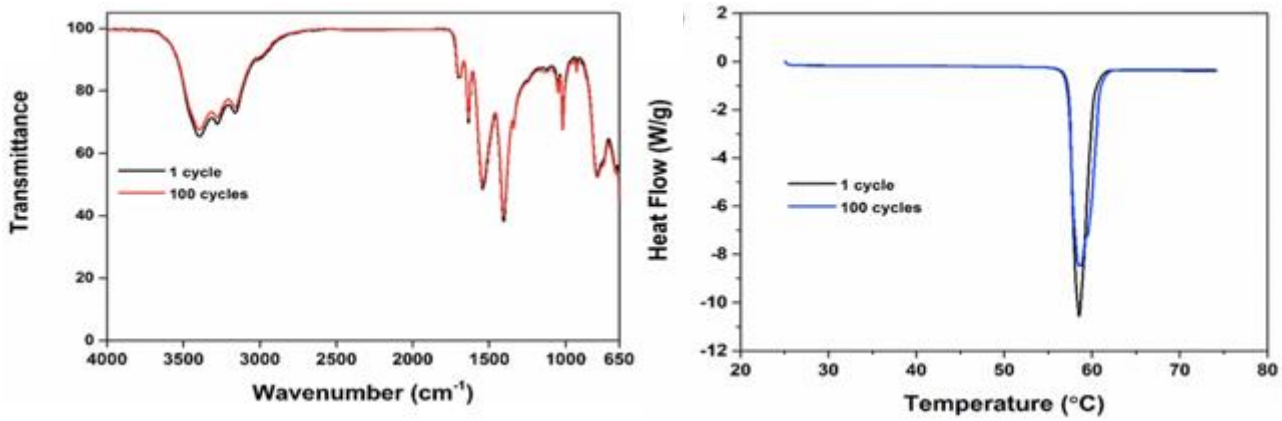

Figure 2.1 SAT+2%DSP+1.0%CNF/AgNP0.02 IR spectroscopy (left) and DSC (right) scans of 100 cycle stability test

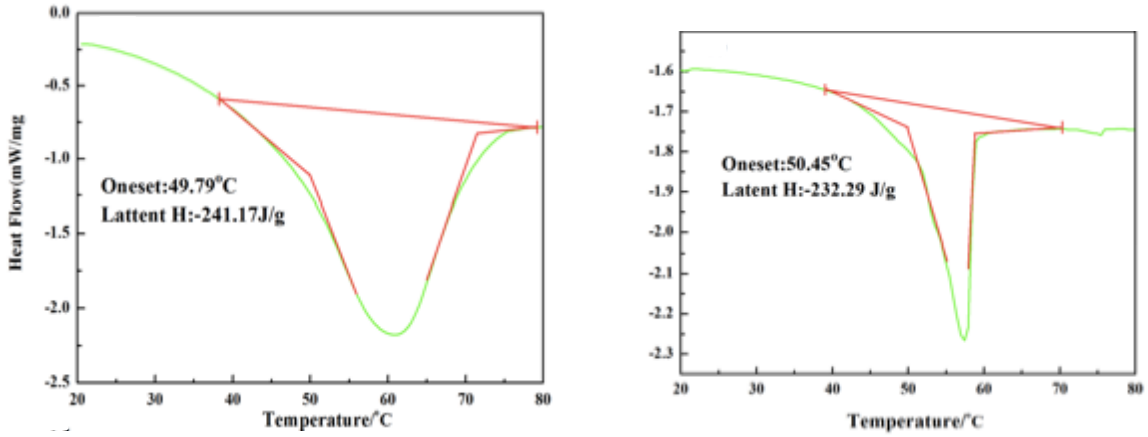

Figure 2.2 SAT+8%KCl+1%Al_2O_3+4%CMC DSC data. 1st scan (left) v. 50th scan (right)

Thermophysical Properties

The effects of CNF/CMF alone are revealed by the experiments conducted by Oh et al., which report the degree of supercooling. The addition of these fiber entanglements has a negligible effect on supercooling but significantly extends the heat release period and maintains a stable temperature for ~40min. In contrast, the PCM without CNF steadily cools after its transition. These differences indicate that CNF increases the PCM's specific heat and promotes full heat release by enhancing the dispersion of salt particles. PCMs without CNF addition are more prone to significant sedimentation, which can conceal anhydrous salt. The distributive effects of the CNF network can sequentially address these issues and enable fully hydrated SAT in solution.

Shen et al. applied a similar concentration of CNF in saturated SAT and effectively reduced supercooling by adding DSP [83]. Interestingly, DSC cooling curves reveal that AgNPs produced from a 0.02 M $AgNO_3$ solution exhibit the least supercooling observed in the study (1.2°C) when the CNF/AgNPs content equals 1.0%. These results suggest that there is a maximum threshold of AgNP concentration beyond which interparticle interference may occur. These results verified the use of SAT+2%DSP+1.0%CNF/$AgNP_{0.02}$ for the remainder of the experimentation as the most promising composite.

SAT+2%DSP+1.0%CNF/$AgNP_{0.02}$ possesses thermal conductivity of 0.580 W/m·K, while that of pure SAT is 0.441 W/m·K, indicating a 31.6% increase. The ability of these additives to affect thermal conductivity at low concentrations is significant for advancing salt hydrate applications in TES. Moreover, the produced PCM composites show negligible differences in melting point (57.4°C v. 57.6°C SAT) and phase change enthalpy (269 kJ/kg v. 270 kJ/kg SAT). These results build upon the research reported by Oh et al. in SAT/CNF PCM systems and provide evidence of PCM enhancement by CNF for phase stability, by AgNP for thermal conductivity, and

by DSP for nucleation assistance. The investigation by Li et al. is of similar scientific value but presents additional additive options for performance enhancement, such as CMC rather than CNF and KCl/Al_2O_3 rather than DSP. Although the effects of Al_2O_3 on thermal conductivity have not been reported, it is anticipated that the impact is positive. Li et al. also completely resolved the supercooling issue with a combination of 8% KCl, 4% CMC, and 1% Al_2O_3 additions.

The effects of CMC or CNF on material cycling stability are particularly significant. Energy storage stability between operating cycles was evaluated via DSC by comparing the enthalpy of phase transition between the 1st and 50th (*Fig. 2.2*) or 1st and 100th cycles (*Fig. 2.1*) of PCMs (Li v. Shen). Data presented by Li et al. verifies phase stability enhancement of SAT by CMC as only 3.6% loss in evolved latent heat is observed from the initial 241.17 J/g (*Fig. 2.2*). However, data by Shen et al. reveals that their SAT PCM system using CNF achieves a greater magnitude of energy storage and extended stability over 100 cycles as only 2.23% loss is observed from the initial 269 J/g and no change observed via FTIR (*Fig. 2.1*). Therefore, it is apparent that CNF is more effective as an additive for extending PCM cycling stability.

Carbon Nanotube & Carbon Nanosphere Composites

Carbon nanospheres (CNS) and multi-walled carbon nanotubes (MWCNTs) are forms of carbon that exhibit large surface areas, high thermal conductivity, and chemical stability. These forms of nanocarbon exhibit excellent hydrophilicity when their surfaces are functionalized with oxygen-containing groups. For the aforementioned reasons, Yang et al. compared the performances of the following to properly investigate the effects of CNS and MWCNT on the TES performance of LiOH monohydrate: LiOH·H_2O (control), LiOH·H_2O/AC (control), LiOH·H_2O/CNS, LiOH·H_2O/MWCNT [81]. LiOH·H_2O/AC was used as a control group, along

with pure $LiOH \cdot H_2O$, to clearly demonstrate the advantages of carbon *nano*materials. MWCNT and CNS possessed diameters of 100nm and 200nm, respectively. All composites were produced in a 1:1 mass ratio by aqueous combination at a 1g/mL loading. In another study, Zhou et al. investigated the use of carbon nanotubes (CNTs) to enhance thermal conductivity in hygroscopic salts [85]. These subjected salts included $Al_2(SO_4)_3 \cdot 18H_2O$ and $FeSO_4 \cdot 7H_2O$, which were combined by aqueous dissolution at a 2:1 mass ratio with 1 wt% CMC to support phase stability. Formulations containing CNT were prepared by an identical procedure, with the addition of 5 wt% CNT. Composites and controls were dried and powdered for analysis. Additionally, composites of carbonate salt PCMs were developed by Tao et al. using single- or multi-walled carbon nanotubes (SWCNTs and MWCNTs) to enhance the specific heat and thermal conductivity [86]. Li_2CO_3 and K_2CO_3 were combined in a 47:53 mass ratio (roughly) to produce the study salt. Sodium dodecyl sulfate (SDS) was combined with carbon nanomaterials at a 1:1 mass ratio prior to salt introduction to better disperse nanoparticles. The results of the three studies are displayed and compared in *Table 2.5*.

Thermophysical Properties

Results by Tao et al. reveal that 1.5% is the optimal concentration of carbon nanomaterials in the Li_2CO_3:K_2CO_3 system to impact composite TES performance. The melting point and enthalpy of composite PCMs were determined via DSC to assess the impact on total TES capacity, which includes both latent and sensible heat storage (*Fig. 2.3*). Graphene and C_{60} were also tested as thermal enhancers. The specific heat of composites is improved, thereby increasing the sensible heat storage capacity. However, the salt composition is reduced by the addition of nanomaterials, which, by default, negatively impacts latent heat storage. Therefore, these carbon nanomaterials

may enhance material-specific heat capacity and thermal conductivity, except for C_{60}, but may have a negligible, if not negative, impact on TES heat capacity. SWCNT is regarded as the most optimal additive due to its excellent contribution to thermal properties. Overall, CNTs are proven to most effectively enhance heat conduction, which is attributed to their column-like structure. CNT improves the performance stability in the $Al_2(SO_4)_3$:$FeSO_4$ system over 100 cycles of heating and cooling (*Fig. 2.4*). The composite with CNT displays 2 J/g loss (422.4 to 420.4 J/g) in absorbed heat, while the loss amounts to 10.54 J/g without CNT (416.00 to 405.46 J/g). Therefore, CNTs have also been shown to improve the stability of salt hydrates across charging cycles.

It should be noted that LiOH systems function as TCMs, whereas Li_2CO_3:K_2CO_3 and $Al_2(SO_4)_3$:$FeSO_4$ function as PCMs. Since TCMs operate via TCES rather than LES in PCMs, the energy densities reported by Yang et al. are significantly greater. These numbers are even more impressive when salt content is factored in. Interestingly, the study by Tao et al. reports a thermal conductivity enhancement much greater than that reported by Yang et al. when using MWCNT as an additive. The reasoning here is that the dispersive effects of the SDS additive allow MWCNTs in the Li_2CO_3:K_2CO_3 to be more evenly distributed and better aligned. The alignment of CNTs is particularly significant to thermal conductivity. The superiority of CNS in improving the performance quality of $LiOH{\cdot}H_2O$ is clear. MWCNT, however, is encouraged as an additive in salt PCM or TCM systems, depending on the preparation procedure.

Table 2.5 Comparison between salt-based composites using CNS or CNT additives [81,85, 86].

Additive	Salt	Additional Additive	Energy Density	Thermal Conductivity
50% CNS	LiOH	-	2020 J/g	15.4% ↑
5% CNT	$Al_2(SO_4)_3$:$FeSO_4$	1% CMC	422.4 J/g	26.2% ↑
50% MWCNT	LiOH	-	1804 J/g	3.5% ↑
1.5% MWCNT	Li_2CO_3:K_2CO_3	SDS – 50% (w/w)	565 J/g	50% ↑
1.5% SWCNT	Li_2CO_3:K_2CO_3	SDS – 50% (w/w)	575 J/g	57% ↑

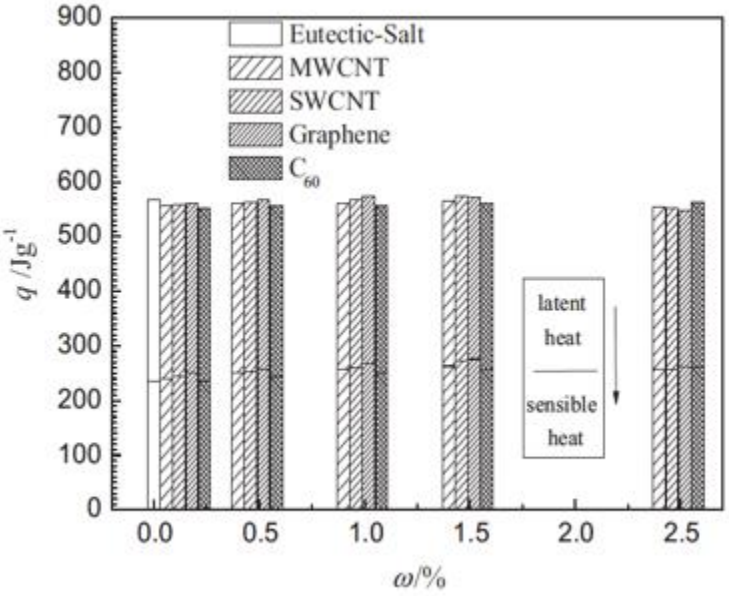

Figure 2.3 Heat storage capacity measurements of composite PCMs v. percent composition

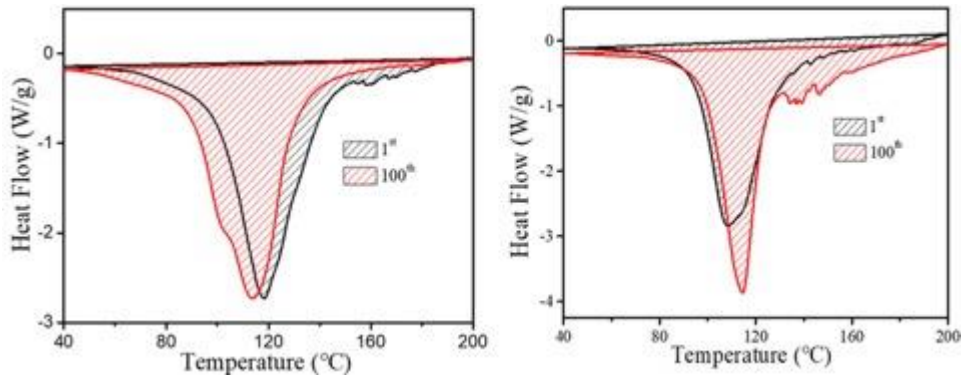

Figure 2.4 DSC data of $Al_2(SO_4)_3$:$FeSO_4$+5%CNT+1%CMC comparing 1st and 100th operating cycle. With CNT (left) and without (right)

Cellulose Nanocrystal Composites

Composite PCM capsules are commonly composed of a subjected PCM coated by a thin layer of a polymer material. The primary benefit of producing PCMs for TES by encapsulation is the high surface area, which is most efficiently achieved by emulsifying the PCM, then

emulsifying and polymerizing the coating material onto its surface. The method ensures a low capsule diameter (<100μm) and prevents PCM leakage through a protective seal. Zhang et al. investigated the use of CNC as an emulsifier and shell component in the formation of polystyrene (PS) coated paraffin wax (PW) and coconut oil microcapsules for TES [87]. PS is added to preheated PW or coconut oil, followed by an aqueous CNC dispersion. The solution is then emulsified by ultrasonication under nitrogen to prepare PS via emulsion polymerization. The resulting composite PCM slurry is allowed to cool and dried to obtain PW+PS/CNC or CO+PS/CNC powder.

Other forms of polymer-based composite PCMs have been developed by exploiting CNC's shape-stabilization effects. Recent publications have highlighted the ability of CNC to enhance thermal energy storage behavior of polyethylene glycol (PEG) via molecular grafting [88-90]. The PEG polymer chains are effectively constrained by the grafted connection to CNC, thereby preventing material leakage during melting transitions. Fan et al. demonstrated the technique in 2020 by grafting PEG onto the surface of CNC in the presence of a maleic anhydride crosslinker (MAH) [88]. Several composites were prepared with reaction times ranging from 4 to 16 h at 4-h intervals. Abdalkarim et al. performed a similar study in 2021, adding metal nanoparticle-grafted CNC (MCNC) [89]. Phase change fiber (PCF) composites were prepared using mechanical homogenization with 50% PEG and 50% Poly(3-hydroxybutyrate-co-3-hydroxyvalerate) (PHBV) by weight. PHBV was added as a supporting material in the composite, whereas PEG served as the energy storage material. PCF composites were also prepared with MCNC addition of 3% and 5% based on the mass of PHBV, which is then homogenized with PEG. Fe_3O_4 nanoparticles were grafted onto CNC to produce MCNCs. PCFs containing 3% and 5% MCNC were characterized and tested alongside the control PCF (PEG/PHBV) and 5% Fe_3O_4-PCF. Dardari et al. have also

demonstrated these concepts by grafting copper NPs (Cu-NPs) onto CNC in PEG-based PCMs [90]. CNC/Cu-NPs were combined with PEG at a mass ratio of 90:10 (PEG: CNC/Cu-NPs), and the energy density was evaluated.

Recent research by Gladen and Bajwa investigated the use of CNCs to provide a structural framework for salt-based TCMs rather than standard porous host matrices [91]. The component addition primarily addresses issues such as incomplete hydration and reduced energy density associated with their use. CNCs are known to exhibit significant mechanical properties, including high tensile strength and modulus, as well as excellent hydrophilicity. These benefits, along with the high surface area of particles (~500 m^2/g), suggest that CNC can effectively enhance the cycling stability of salt TCMs by providing structural support against deliquescence and nucleation assistance while promoting energy release (hydration). Various composites of CNC-impregnated $CaCl_2$ were produced to investigate the impact of CNC on salt hydrate TES cycling stability. CNC:$CaCl_2$ formulations were prepared by individually dispersing anhydrous salt and CNC in aqueous media via mechanical stirring, followed by ultrasonication. Solutions were then combined by dropwise addition of dispersed CaCl2 to the dispersed CNC solution at the following mass ratios (CNC:$CaCl_2$): 1:1; 1:2; 1:4; 1:10. The combined solutions were dried under ambient conditions to obtain CNC-impregnated $CaCl_2$. Composite performance was tested under ambient temperature (~19°C) and two humidity levels (40% and 70% RH) for 20 minutes. The different humidity levels allow for the hydrophilic effects of CNC to be assessed. Materials were then dehydrated from ambient temperature to 105°C at 5°C/min using DSC to quantify the energy stored. TG-DSC data were acquired using STA to relate observed mass changes to thermodynamic events during dehydration properly.

A follow-up study by Karna revisited the 1:4 and 1:10 formulations, using an improved experimental approach [92]. 1:10 CNC:salt was adjusted to 1:9 so that formulations would represent composites containing 20% and 10% CNC by weight. CNC:salt formulations were produced by an identical procedure, with the CNC solution added dropwise to the salt solution. The composite solution was also ultrasonicated to ensure that particles were well mixed and evenly dispersed before drying into the final material. Additional CNC:salt formulations were introduced to the study to discover which CNC:salt systems are most promising, such as CNC:$CaCl_2$:MgSO4; CNC:$SrCl_2$:$CaCl_2$; CNC:$SrCl_2$:$MgSO_4$; CNC:$SrCl_2$; CNC:$MgSO_4$, in addition to CNC:$CaCl_2$. During hydration, CNC:salt materials were allowed to reach equilibrium, as indicated by a plateau in sample mass at 70% RH. It was discovered that the minimum time required for any sample to reach equilibrium was accomplished by pure $CaCl_2$ (225min; 3.75h). The finding reveals that the $CaCl_2$ and CNC:$CaCl_2$ samples in the previous study were insufficiently hydrated, as the maximum hydration time allowed at the time was 45 minutes.

Thermophysical Properties

TES application of the novel PCM capsules was tested by cycling the composite slurries between water baths of 25°C/85°C for PW+PS/CNC and 0°C/40°C for CO+PS/CNC. Samples were submerged in each bath for 10 minutes per cycle [87]. PCM properties and TES application of PW+PS/CNC and CO+PS/CNC were assessed by DSC to qualitatively and quantitatively analyze the enthalpies of melting and cooling. The stability of the CNC was assessed by comparing DSC analyses between the initial and 100^{th} scans. Additionally, several PW/CNC slurries were tested to investigate the effects of CNC on PW microcapsule stabilization thoroughly. The droplet size decreases as the CNC concentration used to stabilize the droplets increases from 0.1 to 0.5

wt%. The DSC scans of the slurries revealed that a CNC dispersion of at least 0.5 wt% is required to achieve effective stabilization of PW performance in TES. PW+PS/CNC slurry possessed a low latent heat capacity (C_p) of 31.9 J/g when compared with pure PW (191.8 J/g), but displays 99.4% stability over 100 scans. PW+PS/CNC powder possessed a latent C_p of 160.3 J/g and a high encapsulation ratio of 83.5%, which indicates the importance of PS in producing stable PW microcapsules.

CO+PS/CNC slurry was investigated, particularly for use in ambient thermal regulation, given its low-temperature phase transitions. The melting and solidification temperatures of CO+PS/CNC were reported as 23.4°C (I) and 7.7°C (T_s), whereas PW+PS/CNC undergoes this transition at higher temperatures: 59.7°C (I) and 55.7°C (T_s). The measured C_p of CO+PS/CNC by DSC indicates an extremely low latent heat capacity for coconut oil compared to PW. However, CO+PS/CNC formulations exhibited superior thermal regulation compared to pure water. Both materials are proven to enhance thermal regulation. PW+PS/CNC is recommended for use in the mid-temperature range, while CO+PS/CNC is recommended for use in the low-temperature range or at ambient temperature. These methods have yet to be applied in research with salt hydrates.

Table 2.6 Summary of energy storage and crystallinity (%) data of PEG and CNC grafted PEG by Fan et al [88].

PCM	T_m (˚C)	ΔH_m (J/g)	T_c (˚C)	ΔH_c (J/g)	Crystallinity (%)
PEG	53.1	150.2	33.2	146.5	83.2
PCM-4h	41.3	23.0	4.2	21.3	21.2
PCM-8h	42.9	30.4	6.5	25.0	29.4
PCM-12h	47.1	82.3	9.8	78.5	61.1
PCM-16h	45.7	50.7	6.0	43.8	55.7

Thermal data for PEG-based PCMs are shown in *Table 2.6*, along with percent crystallinity. T_m and ΔH_m are the melting temperature and enthalpy; T_c and ΔH_c are the

crystallization temperature and enthalpy. The primary benefit of grafting CNC is demonstrated by the thermal reliability testing of PCM-12h, which shows no loss in ΔH_m and a slight increase in ΔH_c over 120 cycles. Thermal conductivity also slightly improves in PCM-12h relative to PEG. Upon heating in an oven set to 50˚C from ambient temperature (25.2˚C), PCM-12h attained a temperature of 34.3˚C, whereas PEG was 33.1˚C [88].

Similar trends were observed in PEG:CNC/Cu-NP composites, which reported a phase transition energy of ~100 J/g, whereas pure PEG is reported as ~147 J/g [90]. These findings reveal an energy density loss of greater than 10% when PEG is substituted by 10% mass CNC or CNC/Cu-NPs, indicating that CNC addition may disrupt the crystallization of PEG chains. However, thermal reliability tests of study materials revealed that PEG experiences an energy density loss of 37.2% over 60 cycles, whereas the PEG:CNC/Cu-NPs maintains a stable response with only 1.1% ΔH_m loss. Other significant improvement in PCMs containing grafted metal NPs is seen during thermal conductivity tests.

Table 2.7 Summary of energy storage data for PEG and PCF composites by Abdalkarim et al. [89].

Material	T_m (˚C)	ΔH_m (J/g)	T_c (˚C)	ΔH_c (J/g)	ΔH_m (J/g): 25 cycles	ΔH_c (J/g): 25 cycles
PEG	65.6	180.5	48.5	168.4	179.5	166.5
PCF	62.9	74.8	48.3	77.5	71.5	73.9
PCF/MCNC3%	62.4	69.2	48.3	66.1	68.6	65.3
PCF/MCNC5%	62.5	81.3	47.3	77.6	80.4	75.5
PCF/Fe_3O_4-5%	61.5	83.1	46.4	79.5	81.6	76.9

The results about energy storage performance of PEG PCM composites developed by Abdalkarim et al. are summarized in *Table 2.7* [89]. It is apparent that the presence of 50% PHBV reduces the overall phase transition energy by more than 50%. Therefore, the presence of PHBV alone disturbs the crystallization of PEG. The grafting of PEG to MCNCs is also observed to

disturb PEG crystallization by restricting polymer chain mobility and further reducing the phase transition energy. However, the addition of 5% MCNC causes H_m to rise above and ΔH_c to meet what is measured by the pure PCF. Interestingly, the addition of 5% Fe_3O_4 NPs to the PCF results in greater energy storage than the addition of 5% MCNCs. The contribution of Fe_3O_4 is attributed to the formation of micro-phase separation between PEG and PHBV caused by the presence of the metal NPs. Energy storage performance was then tested over 25 cycles to assess thermal reliability. The cycling performance of PCFs containing 3% MCNCs is nearly equivalent to PEG, whereas other composites experience a greater loss in transition energy.

Although the discussed PCM composites are not appealing energy storage materials relative to pure PEG, their real appeal lies in alternative charging methods, such as magnetic or solar heating [89]. Pure PEG and composite PCFs were exposed to an alternating magnetic field for 10 minutes (2.5 W; 710 A/m), and the resulting material temperature was measured. Thermal conductivity was not directly measured in PCFs fabricated by Abdalkarim et al., but the PCFs' temperatures increased more rapidly with increasing Fe_3O_4 NP content when exposed to solar radiation. The thermal conductivity of CNC/Cu-NP composites fabricated by Dardari et al. was measured and exhibited a 253% increase with 7% (wt.) addition of Cu-NPs to PEG/CNC [90]. The measurements are summarized in Table *2.8*.

Table 2.8 Summary of thermal conductivity date for PEG, CNC, and PEG-based composites by Dardari et al. [90].

Material	PEG	CNC	PEG/CNC	PEG:CNC/Cu-NPs
σ (W/m·K)	0.245	0.421	0.329	0.835

Magnetic energy storage efficiency was determined based on the energy stored relative to the energy used to generate the alternating magnetic field [91]. Composite PCFs containing 3%

and 5% MCNCs attained an energy storage efficiency of 31.1% and 32.4%, respectively, and PCF/Fe_3O_4-5% attained an energy storage efficiency of 35.7% whereas the magnetic heating efficiency of pure PEG is 0%. For solar heating, pure PEG and composite PCFs were exposed to solar radiation (100 mW/cm^2) via a xenon arc lamp for several minutes until the material temperature began to plateau. Solar energy storage efficiency was calculated as magnetic energy storage efficiency. Composite PCFs containing 3% and 5% MCNCs attained an energy storage efficiency of 48.7% and 58.5%, respectively, and PCF/Fe_3O_4-5% attained an energy storage efficiency of 66.8% whereas pure PEG is unresponsive to solar heating. It is found that as the Fe_3O_4 NP content increases, the efficiency of both magnetic and solar heating improves, driven by magnetic interactions and the material's dark color.

As for TCMs with CNC, initial results reported by Gladen and Bajwa indicate greater water uptake in all developed composites (except 1:10) at 70% RH. 1:2 possesses the greatest enthalpy (118 J/g) when hydrated under 70% RH, but is lowest under 40% (37 J/g) [92]. Additionally, 1:10 outperforms pure $CaCl_2$ (44 J/g v. 39 J/g) and exhibits the second-highest enthalpy, behind 1:1 (46 J/g), when hydrated at 40% RH. Although the reported energy output is low relative to other material systems reviewed, later investigation reveals that CNC:salt materials require an extended hydration time of at least five hours for water uptake to reach equilibrium [93].

Using the improved experimental approach reported by Karna, it is apparent that samples require 5-8h of hydration to reach water-uptake equilibrium at 70% RH, except for pure $CaCl_2$. A summary of experimental data is provided in *Table 2.9*. The reported energy densities are significantly higher due to sufficient hydration. The most promising formulations contain $SrCl_2$. The energy density of pure $SrCl_2$ is also the highest among the salt controls tested in the study. These findings suggest that CNC:salt materials for TCES should be developed using $SrCl_2$ as a

primary salt constituent. The 10:90 variety of CNC:$SrCl_2$ has the highest energy density under experimental conditions, followed by CNC:$SrCl_2$:$CaCl_2$ 10:90 and then 20:80. It should be noted that all samples reached equilibrium, except for $SrCl_2$:$CaCl_2$ and $CaCl_2$-based formulations, which deliquesced.

CNC:$SrCl_2$ and CNC:$MgSO_4$:$SrCl_2$ formulations were selected for cycling, whereas CNC:$SrCl_2$:$CaCl_2$ was omitted because of deliquescence observations during material screening. 80:20 composites were selected because the study's hypothesis posits that the structural integrity provided by CNC improves stability between hydration cycles. 20:80 (CNC:salt) CNC:$SrCl_2$ and CNC:$MgSO_4$:$SrCl_2$ composites were subjected to hydration using experimental conditions of 70% RH for 180 minutes. Materials were dehydrated by DSC using a heating rate of 2°C/min from ambient temperature to 110°C. The hydration-dehydration steps were repeated for 10 cycles. CNC:$SrCl_2$ maintained a desorption enthalpy of 600-700 J/g and exhibited a positive energy density trend as water uptake levels increased during cycling. The CNC:$MgSO_4$:$SrCl_2$ maintained an enthalpy of 450-500 J/g and also experienced a positive energy density trend as water uptake increased. It should be noted that the enthalpy values reported here are lower than those reported in *Table 2.9* due to the reduced hydration time of 180 min. (3h). The positive water uptake trend is attributed to the development of diffusion pathways in the composite, which encourage greater conversion of salt to its hydrated form (*Eq. 1*).

In general, adding CNC to polymer-based PCMs or salt-based TCMs has been proven to enhance cycling stability. For the energy output of PCMs, PW+PS/CNC is stable over 100 cycles; PEG grafted CNC (PCM-12h) is stable over 120 cycles; PCF/MCNC3% is stable over 25 cycles; PEG:CNC/Cu-NPs is stable over 60 cycles [88-90]. For TCMs, CNC:salt composites are stable over 10 cycles [92-93] and may demonstrate improved performance as cycling progresses and

diffusion pathways for water are formed. Although the cycling stability of CNC:salt materials has not yet been proven reliable for as many TES cycles as the discussed PCMs, these investigations are underway and have shown promising preliminary results [94]. Current research by Gladen and Turnaoglu has initiated an extended cycling experiment to demonstrate thermal reliability over 5000 cycles.

Table 2.9 Summary of hydration data reported by Karna via improved experimental approach [93].

Formulation	CNC:salt or salt:salt	Energy Density (J/g)
$CaCl_2$	-	313
CNC:$CaCl_2$	10:90	752
CNC:$CaCl_2$	20:80	365
$MgSO_4$	-	584
CNC:$MgSO_4$	10:90	786
CNC:$MgSO_4$	20:80	543
$SrCl_2$	-	718
CNC:$SrCl_2$	10:90	935
CNC:$SrCl_2$	20:80	763
$SrCl_2$:$CaCl_2$	50:50	333
CNC:$SrCl_2$:$CaCl_2$	10:90	895
CNC:$SrCl_2$:$CaCl_2$	20:80	823
$SrCl_2$:$MgSO_4$	80:20	425
CNC:$SrCl_2$:$MgSO_4$	10:90	761
CNC:$SrCl_2$:$MgSO_4$	20:80	712
$MgSO_4$:$CaCl_2$	47:53	316
CNC:$MgSO_4$:$CaCl_2$	10:90	576
CNC:$MgSO_4$:$CaCl_2$	20:80	704

Additionally, the energy density of TCM composites using CNC is proven to be enhanced and significantly greater than PCM composites using CNC, with a relatively high energy density (CNC:$SrCl_2$ 10:90 – 935 J/g v. PW+PS/CNC – 160.3 J/g). The addition of CNC to the reviewed PCM composites is shown to affect energy density negatively. However, the most significant enhancement to thermal conductivity is achieved by PCM composites engaging CNC/Cu-NPs.

Furthermore, the reviewed PCM composites containing metal nanoparticles can be charged via magnetic and/or solar heating, a distinct advantage. In general, the composite development of CNC-impregnated salt TCMs is promising, as CNC can positively impact material energy density *and* cycling stability.

Composite Component Interactions

As is conveyed by the reviewed research, the primary benefits of engaging nanocellulose and other bio-based supports in the development of PCM and TCM composites include, but are not limited to: degradation resistance, reduced phase segregation, enhanced thermal conductivity, increased specific surface area, prolonged cycling stability, and additional options for material property tuning [78]. Material types such as porous host matrices can provide energy by simply adsorbing or condensing water vapor [79]. For example, de Gennaro et al. reported research in 2022 on the use of zeolites in the capture and storage of thermal energy via water adsorption. However, the zeolite requires much higher temperatures to achieve dehydration (~300°C) and has an even lower thermal conductivity than most salt hydrates (>0.2 W/m·K) [95]. The low energy storage capacity and high cost relative to salt hydrates have also diminished the appeal of these materials for thermal energy storage, although their water uptake per gram is impressive [96]. However, the primary factor of concern for materials in TES is energy density.

There is little interaction between TCM salts and any porous host matrices tested in research. As shown by Druske et al., salt impregnation within the pores of ACF achieved only 63 wt% salt content due to salt leakage during soaking and subsequent drying, resulting in the final product. The open-pore structure of these components, along with the lack of salt-binding, indicates the ineptitude of ACF and other porous matrices in forming PCMs and TCMs for TES, particularly

PCMs, due to salt leakage. Additionally, salt hydrates have been shown to degrade porous host matrices, such as ACF, due to the volume changes they induce, even though these are minimal [97]. Using host matrices to produce salt composites for TES has also presented other complications, such as reduced adsorption and water vapor diffusion kinetics due to elevated viscosity at the material surface [98]. Therefore, the composite-component interactions between the salt hydrate and the porous host matrix may be more negative than positive in terms of material stability and performance. To resolve these issues, it may be worthwhile to investigate porous host matrices that are chemically modified to provide potential binding interactions with salt hydrates, as well as matrices that accommodate salt volume expansion to prevent degradation. The other bio-based supports reviewed have shown positive interactions with salt TCMs and PCMs. These materials are further discussed in terms of two main aspects: phase stability (PCMs) and resistance to deliquescence (TCMs).

Phase Stability

The stability of the material phase is most relevant to PCM performance, as a phase change drives the energy storage mechanism. Therefore, the phase must remain stable by preventing separation in salt PCMs (i.e., sedimentation) and preventing disruptions in crystallinity in polymer PCMs. CNF and CMF are predominantly effective at preventing separation in salt PCMs, particularly CNF. CMF is not as effective as CNF in providing phase stability because of lower fiber entanglements and, consequently, less sedimentation prevention. The ability of these fibers to form an entangled network of structural support has been shown to maintain the suspension of concentrated salt solutions at concentrations below 1% by weight [82-84]. It has been observed and is intuitive that any reduction in the PCM composition (%) results in a loss of energy density;

it is important to use additives that are effective at low concentrations, such as CNF. Cellulose nanofibrils (CNF) and microfibrils (CMF) can form entangled fiber networks and gel above their critical concentrations. The introduction of CNF/CMF to salt hydrate slurries has aided in preventing phase separation in phase change materials (PCMs) in other ways, too, such as increasing viscosity and contributing a structural framework [82-84]. Salt PCMs without CNF tend to experience significant sedimentation, potentially concealing anhydrous salt. The distributive effects of the CNF network can sequentially combat sedimentation, thereby allowing fully hydrated SAT to remain in solution. These findings indicate that interactions between CNF and salt PCMs are most supportive of phase stability, providing structural support while aiding material energy storage and release.

For polymer-based PCMs, the ideology is similar. However, CNF would not be as effective in these materials. In these PCMs, it has been proven that crystallinity percentage is the primary factor in thermal energy storage. The reviewed research indicates that the transition energy of polymer PCMs is correlated with overall material crystallinity. The phase transition enthalpy (ΔH) decreases drastically upon addition of CNC when ungrafted, but increases as PEG is crosslinked to CNC [88]. However, it appears there is a maximum threshold of crystallinity when CNC is grafted to PEG, approximately 25% lower than that of pure PEG. The values follow the same trend as the changes in transition enthalpy (*Table 2.7*), which indicates the importance of maintaining high crystallinity in polymer PCMs. As previously discussed, the loss in transition energy is attributed to excessive crosslinking between CNC and PEG, which imposes greater restriction on the movement of PEG side chains. These restrictions then counteract melting during heating and crystallization during cooling. The crystallization of PEG is disrupted by both non-grafted and grafted CNC particles, as the maximum % crystallinity achieved with CNC is 61.1% [88]. The

disruption is further evident by the subsequent drop in crystallization temperature upon the addition of CNC. Although it has been proven that CNC is not an ideal additive in polymer PCMs due to its impact on energy density, it is worthwhile to investigate further other additives, such as CNTs, that have been reviewed. The dimensionality of CNT is better suited to applications in polymer PCM composites because it is, on average, smaller than CNC in both length and width [99]. There is also research reporting that CNTs not only increase thermal conductivity in a paraffin wax-based PCM but also increase transition energy [100]. There is little research on the use of CNS in such materials, but it is anticipated that the spherical shape would be more disruptive to polymer crystallinity than the rod-like forms of CNT and CNC. Moreover, CNS has a larger dimensionality than CNT on average, so CNT is most suitable as an additive in polymer PCMs because disruption of the polymer matrix is minimal compared to other reviewed additives. The interactions between CNT and a polymer matrix are most supportive of phase stability while providing structural support and maintaining or benefiting energy density.

Deliquescence Resistance

Deliquescence resistance may be interpreted as phase stability, but is discussed separately as the interactions between components in PCMs and TCMs differ. In salt TCMs, component interactions are intended to facilitate the diffusion of water throughout the matrix, preventing the complete solvation and dissolution of superficial salt via adsorbed vapor, also known as deliquescence. This phenomenon forms a liquid barrier on the surface of salt TCMs and ultimately prevents complete and uniform transition to the hydrated phase [101]. In salt PCMs, the role of bio-based supports has been to prevent sedimentation rather than deliquescence. The interactions these material qualities share are the provision of structural support to the salt or polymer matrix.

Bajwa and Gladen have shown that CNC can confer deliquescence resistance in salt TCMs by maintaining a solid phase and distributing water uptake through CNC's structural and hydrophilic contributions. In the preliminary study presented by Gladen and Bajwa, the hydrophilicity of CNC is proven to enhance adsorption kinetics in 1:1 and 1:2 CNC:$CaCl_2$ composites by the increased specific enthalpy of desorption relative to pure $CaCl_2$ [92]. Therefore, CNC impregnation is supported in providing positive physical and chemical interactions that help salt TCMs resist deliquescence.

Formulations containing $CaCl_2$ are more prone to deliquescence under high RH. The success of salt impregnation by CNC in promising 20:80 (CNC:salt) varieties using the improved procedure by Karna was investigated using transmission electron microscopy. The captured images verify nucleation of CNC within the salt body among all observed samples (i.e., CNC:$SrCl_2$:$CaCl_2$; CNC:$SrCl_2$:$MgSO_4$; CNC:$SrCl_2$; CNC:$CaCl_2$) [102]. These findings provide further evidence that CNC impregnation in salt hydrates provides structural support and enhances water diffusion, ultimately allowing greater conversion of salt to the hydrated form via *Eq. 1* while resisting deliquescence. High-performing 20:80 composites were also subjected to a cycling experiment to investigate the effect of CNC on material stability during extended use, focusing on energy storage and deliquescence. CNC:$SrCl_2$ and CNC:$MgSO_4$:$SrCl_2$ both showed a positive water-uptake trend as cycling progressed, resulting in greater energy storage and release. The structural support provided by CNC has facilitated the development of these water-uptake and diffusion pathways. Previous research has shown that salt hydrates lacking structural support tend to conceal anhydrous or partially converted salt via deliquescence events, hindering water uptake beyond the surface [103]. Diffusion pathways are supported by the structural support provided and, in turn, encourage greater conversion of salt to its hydrated form (*Eq. 1*). These interpretations

are supported by research reported by Anjum et al., which investigated the impact of performance cycling on the structure of CNC:salt composites [104].

Forming diffusion pathways while maintaining structural integrity has proven essential to maintaining material performance stability. As water is allowed to transport throughout the material, moisture buildup on the material surface is reduced by RH and salt, preventing deliquescence events. Additionally, ACP was found to have a similar impact in the LiOH system developed by Yang *et al.*, as both water uptake and energy release were improved relative to pure LiOH [81]. Although the effects of CNSs and CNTs on the cycling stability of LiOH were not investigated, improved hydration kinetics of LiOH in composites reported by Yang support the interpretation that the development of a diffusion pathway is assisted by structural support. Furthermore, the hydrophilic functionality of CNT and CNS provides additional assistance for water diffusion within and away from the material surface. These observations of other internal additives suggest that the interaction related to deliquescence resistance is comparable to that of CNC in salt TCMs, primarily because CNT, CNS, and CNC are all known to be hydrophilic unless chemically modified. ACP is hydrophobic, but Yang et al. modified it with surface oxygen groups to render it hydrophilic for TES of LiOH [81].

These similarities among carbon-based additives indicate that salt TCM composite components undergo a consistent chemical interaction that depends on the magnitude and sign of the additive's surface charge. Any differences in performance depend primarily on differences in dimensionality, rather than surface chemistry. Dissolved salt can also form an electrical double layer around CNC and other particles due to their surface charge. These findings are evident in zeta potential measurements, which convey the reduction or 'shielding' in surface charge of CNCs when salt concentration is increased [105]. Salt crystals are then nucleated by the charged additive,

which provides a uniform distribution of structurally enhanced composite material. As seen with salt TCMs using CNC, the uniform distribution of carbon-based supports is essential when forming diffusion pathways and resisting deliquescence. ACP, CNT, and CNS are anticipated to provide a similar support role to salt TCMs, but require further analysis of their cycling behavior to determine the extent of this support. CNF and CMF have not been discussed in relation to deliquescence because the concern applies only to TES, which operates via the adsorption of water vapor. The larger dimensions of CNF and CMF indicate a higher surface area, which is known to reduce adsorption rates and is therefore not beneficial for the performance of salt TCMs [106].

A larger surface area is associated with a higher surface energy, which is known to favor particle interactions. These interactions increase with increasing nanoparticle content and may induce additive aggregation as concentration increases [107]. $LiOH \cdot H_2O$/CNS and $LiOH \cdot H_2O$/MWCNT possess significantly larger surface areas in comparison to $LiOH \cdot H_2O$ (276 m^2/g and 140 m^2/g v. 15 m^2/g) [81]. These values correspond with the order of increasing surface area in carbon nanoadditives: CNS – 381 m^2/g; MWCNT – 343 m^2/g. Heat storage performance tests revealed a lower water-uptake capacity of pure $LiOH \cdot H_2O$ compared to the composites, as LiOH (anhydrous) achieved only 42% conversion to $LiOH \cdot H_2O$ after one hour of hydration. The heat storage density of $LiOH \cdot H_2O$ only reached 661 kJ/kg of the theoretical 1440 kJ/kg as a consequence of incomplete conversion to the hydrated state (RH not reported). Meanwhile, all composites achieved full hydration within one hour [81]. Therefore, it is apparent that additives that increase surface area promote greater hydration and energy density.

CNC supports the same concept: salt data reported by Karna et al. indicated that the greatest measured energy density is achieved by 10:90 composite varieties across all CNC:salt formulations except CNC:$MgSO_4$:$CaCl_2$ [93]. The higher performance of 10:90 formulations is

attributed to the combined effects of increased salt content (v. 20:80 varieties) and the presence of high-surface-area CNCs, which nucleate salt crystals and facilitate the diffusion of water throughout the material (v. salt control). Moreover, the 20:80 varieties also outperform the salt control throughout all sample sets except CNC:$MgSO_4$ [93].

Interpretations and Recommendations

Table 2.10 Rankings of carbon nanoadditives among relevant properties to optimal TCM or PCM performanc

Rank	Performance Stability	Hydrophilicity	Energy Storage	Thermal Conductivity
1	CNC	CNC	CNS	CNS
2	CNT	CNT	CNT	CNT
3	CNF	CNS	CNC	ACP
4	CNS	ACP	ACP	CNC
5	ACP	CNF	CNF	CNF

Much research has been reported since the initial realization of salt hydrate TCMs and PCMs, but investigations continue to optimize material performance. The reviewed experiments have provided valuable insight into the performance of available materials, allowing the identification of promising candidates such as $MgSO_4$, SrCl2, SAT, LiOH, $Al_2(SO_4)_3$, FeSO4, and $CaCl_2$. However, the most valuable information has been provided by methods that enhanced the TES-relevant properties shown in *Table 2.10*; often accomplished through composite formulations. Forms of nanocellulose have proven highly useful in improving stability (CNC; CNT; CNF) and even thermal conductivity (CNT; CNS). A ranking of the reviewed nanocellulose additives studied in the development of composite TCMs and PCMs is presented in *Table 2.10*, based on various relevant properties related to TES performance. It is determined that CNT, CNS, and CNC are the most promising nanocellulose additives among recently developed salt hydrate TES composites, depending on the material system. Other nanoadditives, such as metal or

graphene NPs, also demonstrated successful enhancement of thermal properties, with potential impacts on nucleation and alternative charging pathways (i.e., magnetic/solar). Remarkably, the introduction of these other nanoadditives exhibited optimal performance at concentrations as low as 1%.

It has been found that the nanocellulose surface area and energy storage are directly related in salt TCM composites. Nanoadditives rarely increase material energy density and often reduce it due to the lower composition of the TCM or PCM component. However, nanocellulose may positively impact the TES of salt TCMs by facilitating crystal nucleation and/or enhancing hydrophilicity. Salt TCMs without nucleation agents tend to have lower energy density due to larger crystallite sizes, which slows the diffusion of water molecules beyond the material surface. The slowed kinetics may even cause surface deliquescence before complete hydration is achieved. Therefore, high-surface-area nanocellulose composites promote greater and more reliable energy release in TCMs by providing abundant nucleation sites. Energy storage of PCM composites is directly related to the PCM content, specific heat, and thermal conductivity. Forms of nanocellulose that make significant contributions to specific heat and thermal conductivity, and that prevent phase separation at minimal mass fractions (5% or less), are more advantageous for PCM composite development (CNT; CNS). PCM content is then optimized to maximize energy density. Introduction of additives at higher mass fractions may also disrupt crystallinity within the given PCM, ultimately reducing the transition energy. Nanoadditives that increase the material-specific heat capacity of composites enhance the composites' SES and, therefore, may increase overall energy storage. Nanoadditive contributions to thermal conductivity improve TES composite performance by accelerating heat transfer, enabling shorter phase transition time (PCM) or drying time (TCM). As noted, nanoadditive assistance to phase or cycling stability depends on

the material system, but is recommended as follows: CNF in salt PCMs; CNT or CNC in salt TCMs. CNS is not recommended to enhance cycling stability in salt TCMs, as no cycling experiments were performed.

Future Directions

Various biomaterials have been shown to enhance the TES performance of salt TCMs/PCMs. Porous host matrices have proven useful but are best suited for applications that require a persistent solid form. Carbon nanomaterials, in particular, are promising components for further composite development. In the works presented here, CNF is most effective in PCMs due to its phase-stabilizing network. TCMs, however, are most compatible with other carbon nanoadditives (CNC, CNT, CNS) due to their contributions to salt crystal nucleation and thermal properties. CNT/CNS can effectively enhance thermal conductivity at low concentrations (~1%) and support hydration performance at higher concentrations (~50%). CNC similarly promotes adsorption in salt TCMs and has been shown to extend cycling stability in both salt TCMs and polymer PCMs, but does not contribute to heat transfer. However, CNC may be grafted with metal nanoparticles to enhance thermal conductivity. These results call for further research on the effects of CNT, CNS, and CNC on the cycling stability of salt TCMs (CNS and CNC in particular). These studies are valuable and should be conducted using additional biomaterials to determine which produces the most effective and sustainable composite with salt hydrates. Lastly, there is limited research available on the RH requirements for complete hydration of salt TCMs per candidate, as well as the time requirements per RH to reach equilibrium. Further study of these parameters is needed to define the material's operating conditions properly. In doing so, salt-based composites may provide an effective and

reliable source of sustainable energy via TES in low- to mid-temperature systems as TCMs or PCMs.

CHAPTER THREE

CELLULOSE NANOCRYSTAL STRUCTURAL STABILITY UNDRE CONTROLLED RELATIVE HUMIDTY AND TEMPERATURE

Contribution of Authors and Co-Authors

Manuscript in Chapter 3

Author: Daniel Blake

Contributions: Investigation, Analysis, Writing – Original draft, Visualization

Co-Author: William Smith

Contributions: Writing – Review, Editing

Co-Author: Adam Gladen

Contributions: Supervision, Writing – Review, Editing

Co-Author: Dilpreet Bajwa

Contributions: Supervision, Writing – Review, Editing

Co-Author: Tugba Turnaoglu

Contributions: Writing – Review, Editing

Manuscript Information

Daniel Blake, Adam Gladen, and Dilpreet Bajwa

Reviews on Advanced Materials Science

Status of Manuscript:
_____ Prepared for submission to a peer-reviewed journal
__X__ Officially submitted to a peer-reviewed journal
_____ Accepted by a peer-reviewed journal
_____ Published in a peer-reviewed journal

Abstract

Cellulose nanocrystals (CNCs) have emerged as promising materials for composite development in recent years due to their valuable properties, including high tensile strength and stiffness, biocompatibility, and renewability. Given its outstanding qualities, CNC has potential applications across many fields. As each application requires different storage and/or operating conditions for temperature and humidity, it is essential to understand the stability limits and the degradation pathways via thermal, physical, and biological means. In this study, CNCs were investigated under extreme humidity – 97-100% relative humidity (RH) – and temperature conditions of 40˚C or 60˚C for 2 weeks. The samples were characterized using optical and electron microscopy to analyze morphological features and confirm microbial growth and degradation in treated samples. CNCs were also analyzed using differential scanning calorimetry, x-ray diffraction, and zeta potential analysis. Results were interpreted to determine how the properties of CNCs may be affected by warm, humid storage conditions, including thermal stability, crystallinity, morphology, and surface charge, before and after exposure to extreme conditions. It was found that humid isotherm treatments caused a slight, but insignificant, decrease in thermal stability and a reduction in thermal decomposition energy as the isotherm treatment intensified. Isotherm-treated CNCs were also characterized by reduced dry mass and percent crystallinity, as well as increased agglomeration tendency. The morphology of isotherm-treated CNCs changed with respect to crystal clusters, introducing cracking and smoothing surface features, but showed no change in individual crystals.

Keywords: Cellulose nanocrystal, degradation, high humidity, isotherm, material characterization

Introduction

Cellulose nanocrystals (CNCs) are a prominent material that has attracted significant attention in composite research in recent years. CNC is a valuable product commonly derived from biomass; therefore, it is renewable and biodegradable [108]. CNCs have numerous desirable properties, such as high tensile strength and rigidity, a water-stable crystalline form, water solubility, and the ability to be hydrophilic or hydrophobic depending on their functionalization [109]. Additionally, CNCs are submicron in size (often 10-20nm in width and 100-500nm in length); thus, their small particle size offers a nanoscale impact as additives in composite material development [110]. CNCs may be dispersed with materials such as polymers, glass, etc. in a uniform manner, which allows for the properties of CNC to be shared with other composite component(s) such as: surface-grafting CNC on an ethylene based co-polymer to increase tensile modulus [111], or inserting an interphase layer of CNC in glass fiber and polymer composites to enhance mechanical performance [112]. The crystalline portions of CNC exhibit a higher density of hydrogen bonding, which enhances the material's durability and resistance to physical degradation [113]. Furthermore, CNC addition has demonstrated an immense potential to improve overall sustainability in composite development [114].

CNC is commonly produced via acid hydrolysis methodology of some pretreated biomass, in which amorphous cellulose and other lignocelluloses are dissolved to obtain the crystalline cellulose [115]. The properties and characteristics of CNC depend heavily on both the biomass source and the purification and extraction methods used to obtain crystalline cellulose [116]. For example, woody biomass, such as white pine, is known to have higher cellulose content and a higher degree of crystallinity than herbaceous biomass, such as wheat grass [117]. Woody biomass

is often preferred for CNC production due to its higher theoretical yield of crystalline cellulose. The production of CNC was optimized in 2004 by Bondeson et al. using reaction conditions of 64% (w/w) aqueous sulfuric acid for 45 minutes to one hour, depending on the biomass and pretreatment [118]. The hydrolyzed nanocellulose product is then washed thoroughly with deionized water to remove residual acid. Despite washing, CNC might remain slightly acidic due to functional groups, such as carboxylates, sulfates, and hydroxyls, incorporated onto crystalline cellulose chains during hydrolysis. These functional groups are also instrumental for CNC to exhibit hydrophilic behavior. However, alternative reaction pathways can be used to obtain CNCs with other functional groups, such as hydrophobic groups [119]. This study focuses on *traditional* CNC, produced via sulfuric acid hydrolysis of cellulose fibers derived from pine wood pulp and cotton fiber [120].

Due to its desirable properties, CNC has been utilized in various composites throughout the years for various applications. Using CNC as an additive to enhance material properties has exhibited much potential to improve sustainability in composite development while also enhancing material performance [121]. CNC has already been used in various thermal energy composite materials developed over the years. Recent publications have highlighted CNC's ability to enhance the thermal energy storage (TES) behavior of polyethylene glycol (PEG) via molecular grafting of CNC onto polymer chains. These composites are known as phase change materials (PCMs) because a liquid-solid phase transition of PEG allows thermal energy storage. In 2020, Fan et al. demonstrated that grafted CNC can enhance performance and stability by restricting the mobility of PEG chains and hindering PCM leakage [122]. In 2021, Abdalkarim et al. performed a similar study using metal nanoparticle-grafted CNC, which was then grafted to PEG [123]. In both studies, CNC grafting is proven to support consistency in the quantity of thermal energy storage and energy

release. Additionally, CNC has been used to create a more stable structural framework for salt-hydrate-based thermochemical materials (TCMs) [124]. For some salts, the transition between hydration levels of the crystal structure is known to release heat via reversible chemical phenomena [125].

Eq.1

$$A_xB_y + nH_2O \leftrightarrow A_xB_y \cdot nH_2O + heat$$

Despite the distinct advantages of hygroscopic salts in TCM applications, several issues hinder their effectiveness, including particle agglomeration, phase instability, and deliquescence, which adversely affect cyclic stability and thermal performance [126]. As such, CNC has been tested as a component in the development of salt hydrate composites to provide additional structural stability to salts during hydration and to assist water adsorption and diffusion through its hydrophilic properties. In these TCM composites, salt hydrate crystals are nucleated by CNCs to provide a more structurally sound framework. The result demonstrated that the addition of CNCs enhanced cycling performance and stability. In an associated study, the salt:CNC formulations were exposed to a high relative humidity (RH) atmosphere to induce the conversion of anhydrous or partially hydrated salts to their fully hydrated states, without triggering deliquescence [127]. Beyond thermal energy storage materials, there are applications of CNC where a high-humidity environment may be encountered. For example, enhanced humidity sensors include CNC-based composite films, CNC/plant-based epoxy polymer composites with humidity-sensitive properties, and humidity-responsive photonic films using CNC, glycerol, and PEG [128-130].

Cellulosic materials—both natural and anthropogenic—are recognized as a carbon substrate for both consumption (electron transport) and habitation (solid growth media). Cellulose nanocrystals enhance the biodegradation of biopolymer composites, suggesting they have the potential to biodegrade in their pure form [131]. Many bacteria and fungi have enzymes capable of hydrolyzing cellulose and liberating oligomeric and monomeric sugars under both aerobic (in air) and anaerobic (in the absence of oxygen) conditions, across a range of temperatures from 10°C to 45°C [135]. Cellulolytic enzyme activities have optimal temperature and pH ranges from 50°C to 75°C and pH 5.0-5.5, respectively, but vary by specific organism and enzyme system [132, 133]. These enzyme systems may be more effective against either crystalline or amorphous cellulose or exhibit activity against both [134]. Hydration of salt:CNC composites is expected to occur in the range of 20°C to 50°C in humid air. The salt:CNC composites' most significant susceptibility to biodegradation occurs under aerobic conditions, at high humidity (>90% RH) and around 45°C, within the optimal range for microbial and fungal cellulolytic enzyme activity. Idaho National Lab (INL) used these conditions – 45°C, in air, and at (RH=100%) and just under (at RH=96%) saturation conditions—to evaluate the biodegradation potential of these CNC samples. At this time, we have used only the "native" microflora present in these samples; no attempt has been made to synthesize, handle, or analyze these CNC materials under sterile conditions.

Although the efficacy of CNC has been demonstrated many times, the stability and/or degradation pathways, particularly in high relative humidity environments, have not yet been investigated to the best of the authors' knowledge. Conditions with high RH and above-ambient temperatures are more favorable for microbiological growth and consequent biodegradation. Thus, it is necessary to determine whether CNC is susceptible to microorganisms to develop high-quality composites that employ CNC, especially under warm, humid atmospheric conditions. As such, in

this study, the stability of CNC is studied at elevated temperatures of 30˚C, 45˚C, 60˚C, and high humidity of 96-100% RH to investigate the possible biological growth and degradation in two separate experiments:

1. Water adsorption (physical degradation) – 30˚C and 60˚C treated from 0-100% RH (i.e., 0-1 water activity)
2. Microbial growth detection (biodegradation) – 45˚C treated at 96-100% RH for 2 weeks

The research presented here is reported to aid the development and understanding of salt:CNC composites for use in mid- to low-grade TES and climate control in small buildings and homes. However, the provided study is likely to assist in both understanding and the development of future composites that incorporate CNC, particularly those that may be exposed to a high RH atmosphere. It is hypothesized that CNC displays minimal biological growth and degradation after two weeks due to its acidic nature. Since CNC is primarily produced via acid hydrolysis, the material often retains an acidic quality from the treatment, due to functional group alteration and potential binding of residual acid and/or hydrogen transfer to these groups. Therefore, biological growth and degradation are inhibited by the unfavorable environment. CNC may exhibit physical degradation due to water adsorption and the hydrostatic pressure applied during water diffusion throughout CNC particles [135].

Materials and Methods

The CNCs in this experiment were received from the USDA Forest Products Laboratory (Madison, WI) and used as received for the control sample. CNCs were stored in a sealed chamber at 45˚C for two weeks in a high-moisture environment to test the shelf life and storage stability of

the material. CNCs were also tested at 30˚C and 60˚C using an isotherm generator to examine moisture content as a function of water activity. These test parameters were selected based on worst-case conditions for TES applications in buildings and are also likely to promote biological growth [136]. The sample chambers containing the CNC samples were heated to 105°C overnight (16 hours) before the storage experiment was conducted. Dried CNCs were size-reduced in a ball mill (Retsch, PM100) at 300 RPM for 3 minutes using a 500 mL cup with 16 zirconium 2 cm diameter balls. CNCs were tested and analyzed for their water activity and biological stability. These samples are referred to as *treated CNCs* for the remainder of the article. During biological sample preparation, sterile conditions were maintained to determine whether CNC material contains spores of bacteria and/or fungi originating in the material or introduced during preparation and/or transportation. During the two-week storage experiment, samples of CNC were incubated at temperatures and water activities relevant to the conditions in which the material would be applied in building heating applications. No attempt was made to perform the incubations under sterile conditions, as sterile conditions cannot be maintained in the intended application of these CNC materials. Storage tests were designed to evaluate CNC for physical and chemical degradation as well as potential biodegradation during the adsorption phase.

Adsorption Tests

The adsorption isotherms of pure CNC were measured at 30 and 60°C. The as-received CNC, with no adsorption exposure, was designated as the control sample for these tests. Adsorption isotherms of CNCs were analyzed using an isotherm generator (AquaSorp, Decagon Devices) (Pullman, WA) to understand the relationship between moisture content and water activity at different temperatures of 30°C and 60°C. The isotherm generator utilizes the Dynamic

Dewpoint Isotherm (DDI) method to generate complete isotherms. The DDI method directly measures gravimetric water activity independent of the water activity equilibrium measurement. In this method, adsorption is measured by passing saturated wet air over the sample, and desorption is measured by passing desiccated dry air over the sample. Two isotherm models and associated parameters were obtained from the isotherm generator: Brunauer–Emmett–Teller (BET) and Guggenheim-Anderson-de Boer (GAB). Results from the BET model are reported here but are only applicable to water activity up to 0.5. GAB is a multi-parameter model that estimates moisture content (m) as g/100g solids. Where m_0 is the monolayer water content, k and c (or c_1) are constant parameters. The constant k accounts for the properties of the water molecules in subsequent layers, bridging the gap between the monolayer and liquid water. The symbol c refers to the BET constant, which is a dimensionless parameter related to the heat of adsorption and condensation of the vapor or gas; c_1 refers to the Guggenheim constant, which is related to the heat of sorption of the monolayer [137].

Additionally, the BET method provides an estimate of the change in surface interaction energy (Q_s). The results of the isotherm models are summarized in *Table 3.1*, and the resulting isotherms are graphically shown in *Figures 3.1 and 3.2*. Moisture content is provided through the following equations, in which *Eq. 1* corresponds to BET and *Eq. 2* corresponds to GAB:

Eq. 1

$$m = \frac{(cm_0a_w)}{(1-a_w)(1-\ln(1-a_w)^c)}$$

Eq. 2

$$m = \frac{(c_1km_0a_w)}{(1-ka_w)(1-ka_w+c_1ka_w)}$$

Mass Loss and Microbiological Growth Detection

Size-reduced CNCs were dried at 45°C in a desiccator chamber for 72 hrs. Three chambers were prepared for the tests under different relative humidity conditions: a) control at dry conditions (~0% RH); b) saturated conditions (100% RH); and c) Sub-saturation (96% RH). Approximately 200 mL of distilled water was added to the bottom of the desiccator, and a ceramic platform was placed on top before sealing the chamber for the saturated conditions. Control dry conditions were prepared by placing desiccant at the bottom of the desiccator chamber, beneath the ceramic platform. The sub-saturated condition was obtained by using a slurry of K_2SO_4 at the bottom of the desiccator chamber instead of water or desiccant; the sealed chambers were placed in an oven at 45°C. The CNC material was placed in the desiccant chamber on pre-weighed aluminum foil pans (n=5) in replicates. The CNC was stored for 14 days. The samples were reweighed after storage, and a portion was dried at 105°C.

Differential Scanning Calorimetry

The thermal stability of CNCs was tested via DSC (Waters, Multi-Sample X3 DSC) (New Castle, DE) using a heating and cooling ramp rate of 5˚C per minute from 30˚C to 350˚C and vice versa.

X-ray Diffraction Analysis

CNC crystallinity was measured via powder XRD analysis (Bruker, D8 Advance Powder XRD) (Billerica, MA) using the Segal method to estimate the amorphous fraction of cellulose Iβ. The estimation is then used in *Eq. 3*, where *CI* is the crystallinity index, I_{200} is the intensity of the 200 plane of crystalline cellulose, and I_{am} is the maximum intensity of the 'amorphous halo'

occurring between crystalline peaks at approximately 18˚ 2θ [138]. The calculation yields a percentage and represents the portion of CNC that is indeed crystalline.

Eq. 3

$$CI = \frac{I_{200} - I_{am}}{I_{200}} \times 100$$

Zeta Potential Measurement

CNC surface charge and flocculation tendency were determined via zeta potential measurements (Zeta-Meter, System 4.0) (Harrisonburg, VA) by calculating the average of 50 individual particle charge readings. Samples were prepared following the traditional CNC methodology by dispersing CNCs in 50 mmol NaCl (aqueous) at 0.25 wt%. The solution is then loaded into the Zeta-Meter cell for zeta potential measurement.

Scanning Electron Microscopy

CNC morphology of clusters was depicted via SEM (Zeiss, SUPRA 55VP; Oberkochen, Germany) at a working distance of 3.5mm and electron beam voltage of 1kV to reveal potential damage or effect on crystal clusters. Samples were used as-received with no additional preparation prior to imaging.

Transmission Electron Microscopy

CNC morphology of individual crystals was depicted via TEM (Zeiss, LEO 906; Oberkochen, Germany) using an electron beam voltage of 100kV and 3% uranyl acetate stain to assist contrast during imaging. The samples were prepared in deionized water using a

concentration of 0.25 wt%. TEM imaging also supports conclusions drawn from zeta potential experiments by allowing visualization of flocculation tendency in an aqueous environment.

Results

Adsorption Tests

The moisture content of CNC at 30°C for $a_{n\,aw}$ of 0.6 ranged from 11.56% to 13.87% based on the dry CNC weight, as shown in *Figure 3.1*. The moisture content of CNC at 60°C for $a_{n\,aw}$ of 0.6 ranged from 11.91% to 14.17% based on the dry CNC weight, as shown in *Figure 3.2*. Since $a_w < 0.6$ is preferred for food or similar materials which may spoil in a warm and humid environment, it is suggested that the material should be operated at a moisture content less than 11.6% or relative humidity less than 60% at room temperature (i.e. 25°C) to moderate temperature of 60°C when the addition of preservatives or creating sterile conditions is not feasible [139]. The BET isotherms are shown up to aw = 0.5 because the data become less reliable at aw > 0.5.

The surface interaction energy is higher at 60°C than at 30°C for both adsorption and desorption (BET method). The monolayer moisture content (m_0) ranges from 6.25% to 9.22% across all methods, as shown in *Table 3.1*. The GAB method reports a lower m_0 on average than BET, but BET reports a greater prediction error for m_0. The symbol R^2 indicates the correlation of the adsorption data with the models, and the symbol E denotes the prediction error, which is a statistic that defines the residual error of the predicted moisture content relative to the actual moisture content for these tests. The GAB method yields the highest and most consistent R^2 values and lower E values on average, indicating that it is best suited to model the water adsorption of CNC. The BET method is valuable because GAB does not account for surface interaction energy, which is significant for interpreting observations, as will be discussed later.

Table 3.1 Equation 1 and 2 parameters relating to GAB and BET adsorption isotherms in Fig. 3.1 and 3.2

Method		*60°C Adsorption*	*60°C Desorption*	*30°C Adsorption*	*30°C Desorption*
GAB	c_1	41.449	29.252	22.972	22.653
	k	0.794	0.727	0.794	0.748
	m_0	6.250%	8.440%	6.410%	7.990%
	R^2	0.995	0.999	0.983	0.998
	E	±0.391%	±0.207%	±0.756%	±0.288%
BET	c	18.396	17.989	10.812	12.708
	m_0	7.520%	9.220%	7.940%	9.150%
	R^2	0.967	0.983	0.872	0.979
	E	±0.340%	±0.296%	±0.853%	±0.365%
	Q_s	8066 J/mol·K	8004 J/mol·K	6000 J/mol·K	6407 J/mol·K

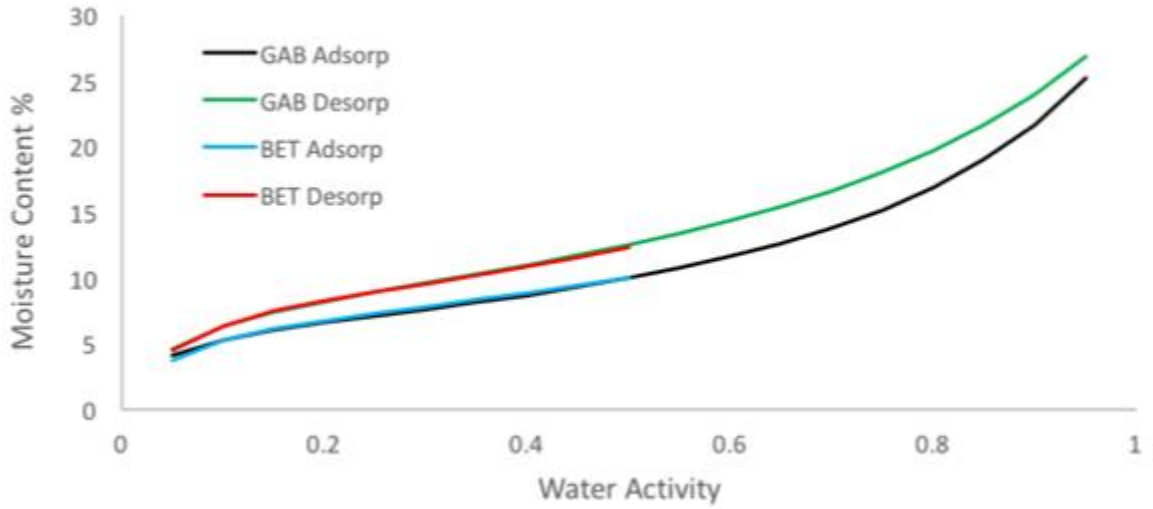

Figure 3.1 GAB and BET moisture content % vs. water activity for 30°C treated CNC

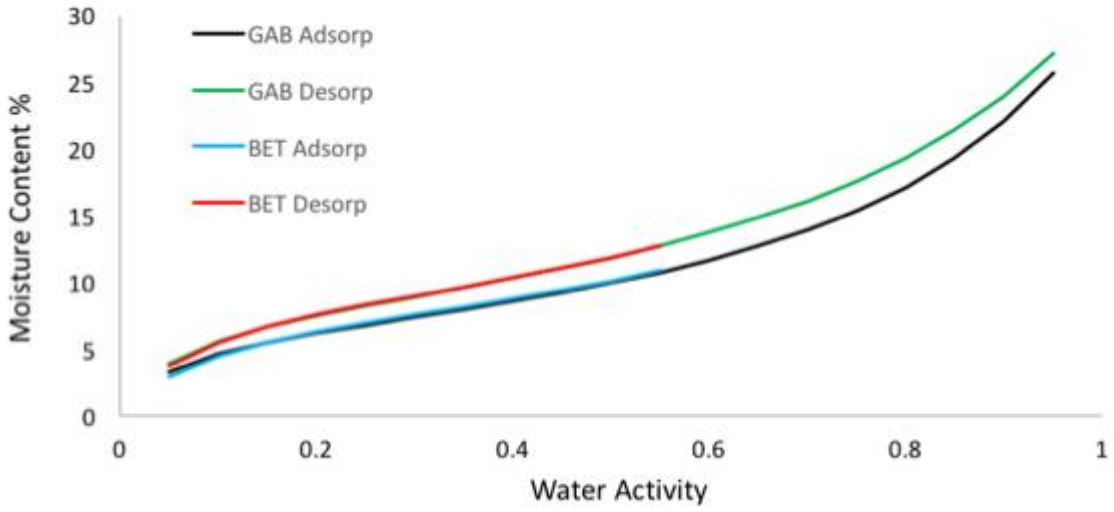

Figure 3.2 GAB and BET moisture content % vs. water activity for 60°C treated CNC

Differential Scanning Calorimetry

Thermal stability testing of CNC samples by DSC reveals that some degradation in material properties has occurred. As shown in *Figure 3.3a*, the thermal decomposition of control CNC occurs at ~272°C. However, the thermal decomposition of treated samples occurs at ~253°C in 60°C isotherm-treated CNC (*Figure 3.3b*) and at ~252°C in 30°C isotherm-treated CNC (*Figure 3.3c*). These results indicate that the thermal decomposition of CNC occurs at a lower temperature after the treatments. The exceptionally sharp, narrow peak observed before thermal decomposition in all thermograms corresponds to the dehydration of adsorbed moisture within the samples, which may occur at temperatures between 100°C and the thermal decomposition temperature, depending on the amount of water and the CNC binding energy [140]. It is also apparent that the energy required to degrade CNC thermally decreases from control CNC in 30°C isotherm-treated (230.32 to 129.85 J/g) and even further in 60°C isotherm-treated samples (84.91 J/g).

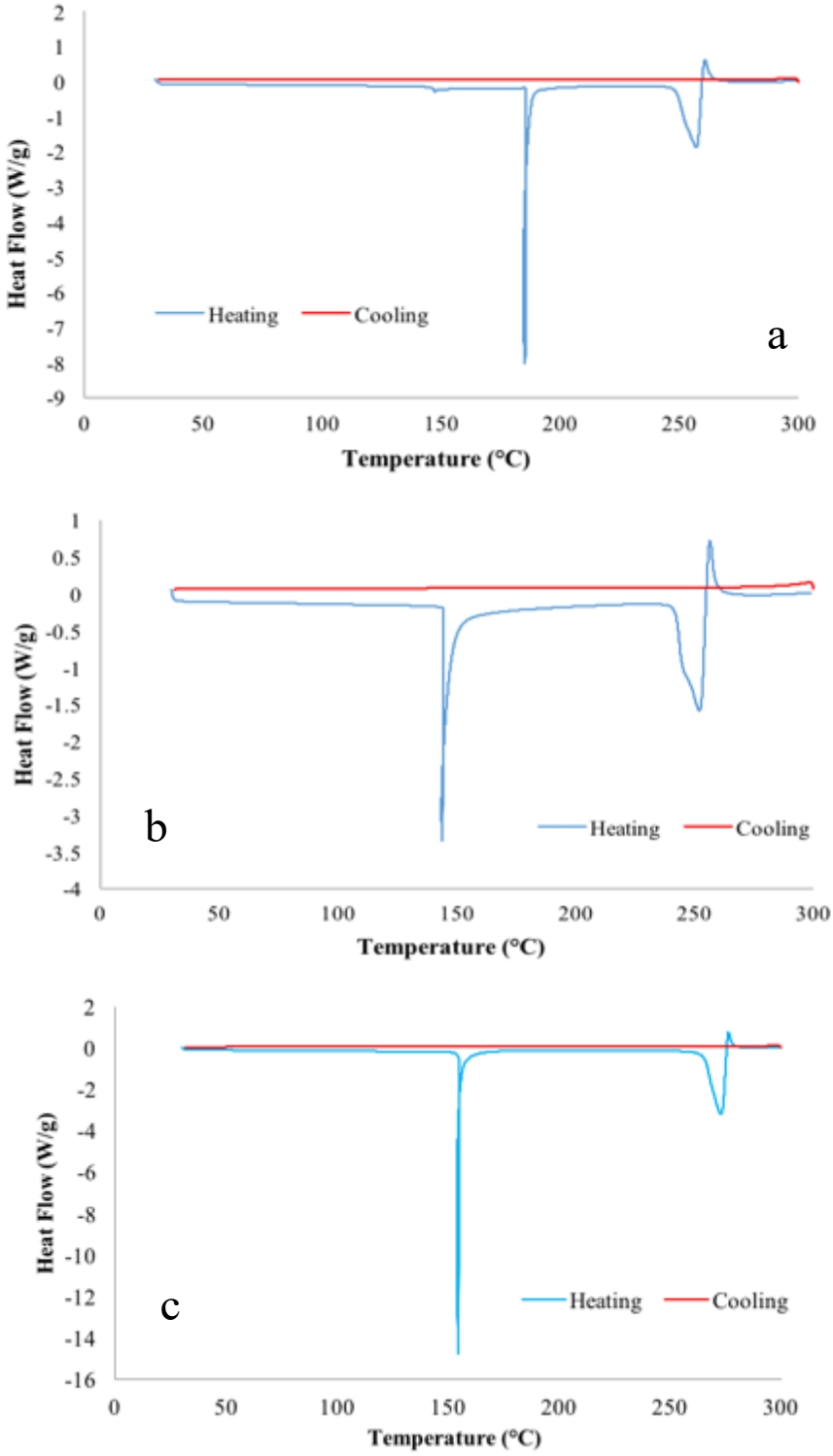

Figure 3.3 DSC heating (blue) and cooling (red) scans of: (a) 60°C treated CNC, (b) 60°C treated CNC, and (c) control CNC from 30°C to 300°C using ramp rate of 10°C/min.

X-ray Diffraction Analysis

In addition to thermal stability, the crystallinity of CNCs before and after experimental treatments was investigated (*Fig. 3.4)*. The crystalline fraction of CNCs was measured via an XRD scan from 5° to 70° 2θ to capture all relevant crystalline peaks. It should be noted that the curved baseline shown beneath each XRD pattern is representative of the estimated amorphous fraction by the XRD software (Bruker, DIFFRAC.SUITE). The crystalline peaks of CNC across all samples appear at identical 2θ values, as shown in *Figure 3.4*, indicating that the lattice parameters and, therefore, the crystal structure of CNC were not altered by the treatments. XRD spectra of treated CNCs samples also contain additional 'stray' peaks appearing most prominently at ~20° and ~27°, and less prominently at ~50° and 60° 2θ. Moreover, analysis using XRD software (JADE) revealed that the treated CNC samples contain quartz contamination. While the crystal structure is unaffected by the treatments, the crystalline fraction of treated CNC is reduced relative to the control, as determined by the Segal method (Eq. 3). The CNC control crystallinity is approximately 79.1%.

In contrast, the 30°C-treated CNC is 66.2%, and the 60°C-treated CNC is 66.7%. It should be noted that all crystallinity values are reported to ±6.5 % in the original published method [141]. It should also be noted that there is no concern that quartz contamination could skew the baseline of the amorphous 'halo' in Segal method calculations, as quartz contributes a negligible amorphous fraction [142]. A significant response in XRD was observed because of quartz's high crystalline order relative to CNC [143].

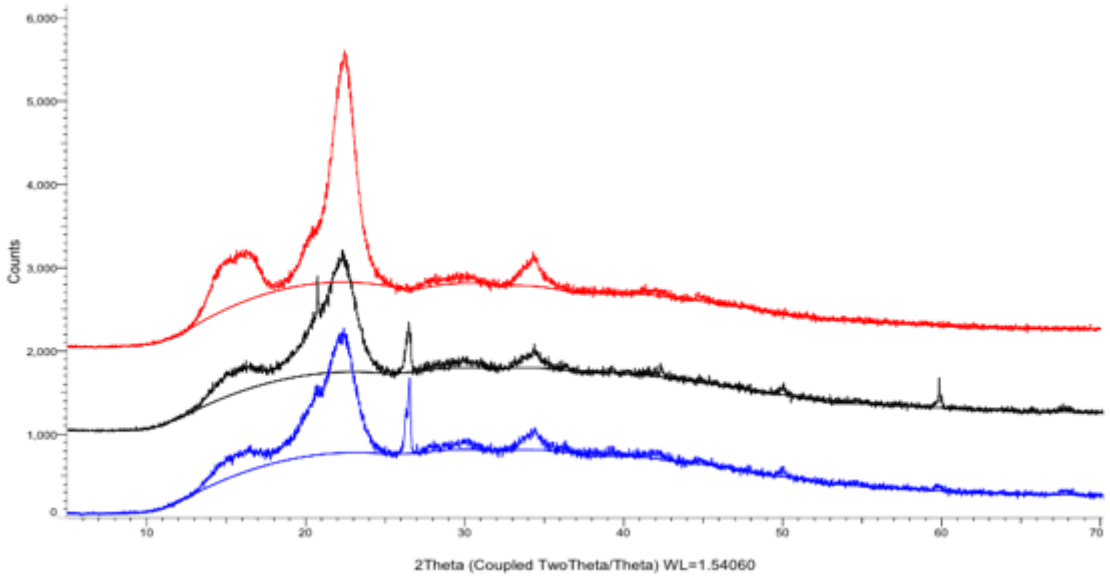

Figure 3.4 Stacked XRD patterns from 5° to 70° 2θ of control CNC (red); 30°C treated CNC (black); 60°C treated CNC (blue)

Scanning Electron Microscopy

SEM imaging reveals some change in the topographical texture of CNC clusters compared to control crystals (*Fig. 3.5*). As shown in *Figure 3.5a*, the individual CNC crystals in the control sample are more distinct, and CNC particles appear incredibly defined, with a higher visible surface area and rougher surface features. Conversely, the individual CNC crystals in treated samples are not visible, and surface features appear smoother with less visible surface area, as shown in *Figure 3.5b* and *Figure 3.5c*. These findings suggest that reorganization of individual crystals occurred within CNC clusters during treatments and is attributed to water adsorption. Other morphological differences observed between the control and study samples include the introduction of 'cracking' in CNC clusters, which may also be attributed to hydrostatic forces during water adsorption [144].

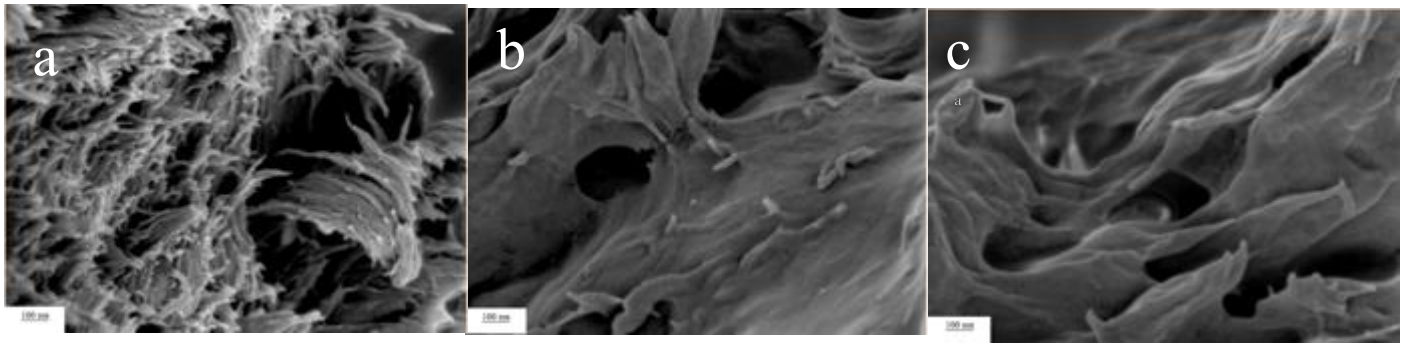

Figure 3.5 SEM images of CNC samples acquired at 56170x magnification: (a) control; (b) 30°C treated; (c) 60°C treated

Zeta Potential

Table 3.2 presents zeta potential measurements for the study and control CNCs, showing a significant trend in the average zeta potential of the colloids. It is reported that isotherm-treated CNCs exhibit lower zeta potential magnitudes and greater flocculation tendency than control CNCs [145]. The zeta potential magnitude decreases further as the isotherm treatment temperature increases from 30°C to 60°C. Therefore, it can be assumed that the degradation process due to exposure to a warm, humid atmosphere may be heightened or accelerated as temperature increases, with respect to particle stability.

Table 3.2 Zeta potential data for control CNC and treated CNCs.

Sample	Avg. Zeta Pot.	Std. Deviation	Counts
Control CNC	-64.63 mV	± 9.52	50
30°C CNC	-48.92 mV	± 5.95	50
60°C CNC	-36.17 mV	± 3.62	50

Transmission Electron Microscopy

TEM imaging reveals an identical morphology of individual CNCs when dispersed in an aqueous solution of low concentration (i.e., 0.25 wt%). Images in *Figure 3.6* show CNCs

approximately 100-200 nm in length and 10-20 nm in width, indicating that there is no significant impact on crystal size during the experimental degradation process after 2 weeks. However, the TEM images provide further evidence of an increased tendency toward aggregation in 30°C-treated CNCs and even more so in 60°C-treated CNCs relative to the control. It is clearly apparent that some attractive intermolecular interactions of CNCs are hindering the dispersibility in its preferred media for dissolution. Therefore, CNC functionality may have been affected during the high RH treatments, ultimately leading to a loss of surface charge [146].

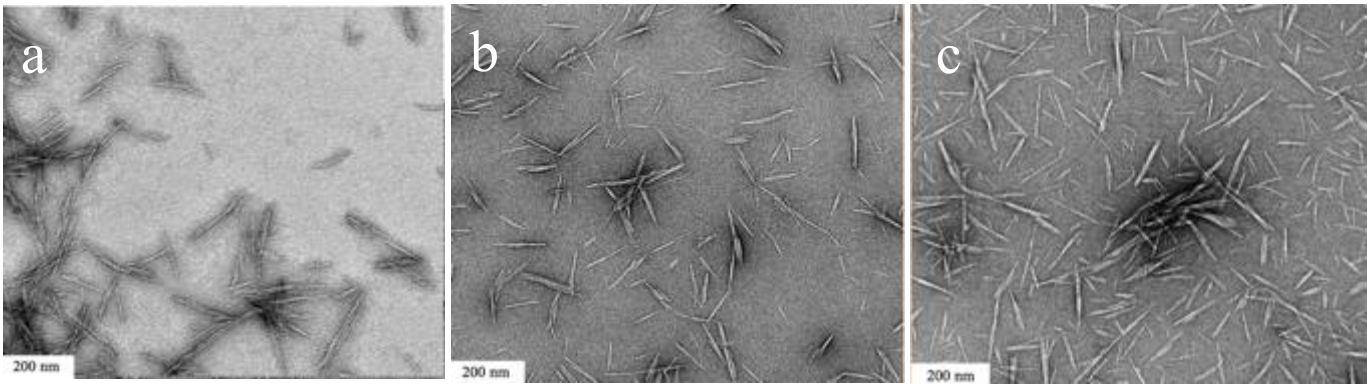

Figure 3.6 TEM images of CNC samples acquired at 15000x magnification: (a) control; (b) 30°C treated; (c) 60°C treated

Mass Loss and Microbiological Growth

The mass loss measurements after exposure to the 45°C treatment are 1.7% ±0.3% for the control CNC sample. The mass loss for the sample stored under saturated conditions (RH 100%) was 2.7% ±1.4%. The mass loss for the CNC sample stored at a humid sub-saturated (RH 97%) condition was 4.02% ± 2.46%. Mass losses were determined using five replicate measurements, which provide a residual error estimate for these values. The increasing error trend as mass loss increases indicates that there is no significant difference in mass loss between the varying-humidity treatments for 45°C/2-week treated CNC. The direct source of the mass loss

cannot be identified without further analysis [147]. Likely, mass loss is primarily due to the hydrolysis of cellulose induced by water molecules at high humidity [148]. The microbiological growth detection of 45°C/2-week humidity-treated CNC was inconclusive.

Discussion

Thermophysical Degradation

DSC analyses have revealed a lower thermal degradation temperature in adsorption-tested CNC samples, along with a decreasing trend in thermal decomposition enthalpy. The loss in crystallinity was verified and quantified by XRD, which showed no significant difference between the temperature treatments (30°C – 66.2%; 60°C – 66.7%). However, the decreasing trend in the thermal decomposition enthalpy with increasing treatment temperature indicates a reduction in the energy required to break down CNC. The reduction in crystallinity did not significantly affect the decomposition temperature, as the treated samples decomposed at a similar temperature of 252-253°C. These findings suggest that the rate of degradation is not significantly affected by elevated isotherm temperatures from 30°C to 60°C during short-term storage. The reduction in crystallinity observed during isotherm treatments is most significant because it negatively affects CNC thermal stability and is expected to compromise the material's mechanical properties by weakening its structural integrity [149]. Crystalline regions were likely degraded via an alternative pathway, as the reduction in crystallinity was observed in samples subjected to water adsorption modeling rather than microbiological growth testing. The reduction in crystallinity observed in adsorption-modeled samples is attributed to physical and potentially chemical disruptions caused by interactions with water molecules [150]. As water is adsorbed and becomes bound within CNC clusters, hydrolysis reactions between water molecules and the crystalline regions of cellulose

become more likely [151]. The water uptake and retention of CNC are primarily driven by amorphous regions that remain intact and can then diffuse into crystalline regions, allowing hydrolysis to occur. If crystalline portions of CNC were favored during the (bio)degradation process, then the humidity-isotherm treated CNC would require less energy to achieve thermal decomposition, which is what was observed in adsorption tested CNC samples. These observations were not recorded for the CNC treated at 45°C. However, the anticipated reduction in crystallinity is expected to have occurred under the treatment as well, since the atmospheric exposure is similar in both experimental setups.

Morphological Degradation

The morphological changes in CNC during 30°C and 60°C humidity treatments are primarily observed by SEM. As shown above, the surface topography of control CNC clusters appears to display superior single-crystal definition, whereas that of treated CNC clusters appears smooth, with minor to no single-crystal definition. Moreover, the smoothness of CNC clusters appears to be more pronounced as the temperature increases from 30°C to 60°C, suggesting a decrease in surface area [152]. These findings indicate that water uptake by CNC clusters triggers reorganization of individual crystals, resulting in reduced roughness and reduced cluster definition. The smoother surface features of 60°C-treated CNC are also significant for varying temperature treatments, as diffusion kinetics increase at elevated temperatures and may further affect the topography of crystal clusters [153]. SEM observations also reveal hydrostatic cracking in the treated CNCs, which is attributed to swelling and subsequent physical degradation due to water uptake [154]. CNC cluster cracking appears larger by visual observation in 30°C-treated CNC compared to 60°C, providing further evidence for the attribution [155]. Atmospheric water activity

generally increases with temperature, so the 30°C-treated CNC is anticipated to exhibit greater water adsorption than the 60°C-treated CNC [156]. This phenomenon is observed in the study data (*Fig. 3.1* and *Fig. 3.2*). However, CNC treated at 30°C is likely to exhibit greater water uptake and swelling, as lower temperatures favor the deposition of water vapor [157]. This occurrence may then lead to greater drying stress in the 30°C-treated sample [159]. These outcomes provide evidence supporting temperature as a relevant variable in the degradation rate of CNC.

TEM observed no significant change in morphology, but the zeta potential findings are supported by the higher aggregation tendency observed in the humidity-isotherm-treated samples. Single crystals appear identical in dimensionality and shape across the TEM images shown above; the only visible differences between CNCs are more populated, generally larger clusters in the treated CNC, and larger clusters as the temperature is increased during treatments. These findings, in addition to the decreasing trend in surface charge shown in *Table 3.2,* suggest a greater tendency for CNC to agglomerate when partially degraded by exposure to a humid, warm atmosphere [158]. The consequential loss of surface charge reduces the deterrence to CNC aggregation by reducing electrostatic repulsion within individual crystals [159]. The greater loss in surface charge observed for 60°C-treated CNC relative to 30°C-treated CNC is attributed to the higher surface interaction energy measured during 60°C treatment. The greater surface interaction energy can cause more sulfate groups that provide surface charge to CNC to be hydrolyzed and thus removed from the surface [160].

Mass Degradation and Microbiological Growth

In particular, the loss in surface charge suggests that the mass loss observed in the study samples may have followed an *outside-in* pathway, since the surface charge of CNC is primarily

provided by sulfate groups introduced during acid hydrolysis [161]. The loss of mass via functional groups could have occurred through hydrolysis reactions induced by water adsorption or through biodegradation driven by microbial growth. A minority fraction of the dry matter losses in these samples may be attributed to a potential biological degradation event, since water activities (a_w) at or above 0.8 support growth and activity of osmophilic yeasts and xerophilic fungi; water activities above a_w 0.9 support growth of many cellulose-degrading bacteria and most fungi [162]. Furthermore, the control CNC stored under dry conditions is reported to exhibit a measurable mass loss of 1.7% ±0.3%, attributed to structural transformations induced by drying stress and dehydration reactions [163]. At higher temperatures (e.g., 105°C), CNC drying stress may induce dehydration reactions within the biomaterial, leading to mass loss via hydroxyl groups [164]. Therefore, some of the mass loss (1.7% ±0.3%) may not be attributed to biodegradation or to hydrolysis via CNC-water interactions. The majority of mass loss in the study samples is attributed to hydrolysis reactions via water adsorption and thermal stress during drying.

Additionally, because the majority of CNC is crystalline, microbes and fungi that prefer crystalline portions of CNC as a feedstock are more likely to dominate the biodegradation process [165]. Crystalline portions of CNC would then be favored to biodegrade over any remaining amorphous portions, consequently, via enzymatic hydrolysis of microbiological species which naturally occurred within CNC samples at the start of experimental treatment [166]. However, it is recommended to more closely investigate the biological growth and biodegradation of CNC to support these claims. Future studies should conduct a longer-term storage experiment to determine whether the degradation rate remains constant, accelerates, or decelerates over time under warm, humid conditions. The mass losses should also be further evaluated to determine the dominant pathways among hydrolysis, dehydration, and potential biodegradation. Moreover, identification

of the species involved in potential microbiological feeding and/or growth would provide valuable insight into the definition of the biodegradation mechanism.

Conclusion

CNC degradation pathways via warm, humid atmospheric exposure include: reduced dispersion stability, loss of dry matter and crystallinity, reduced thermal decomposition energy, and reduced thermal stability. The reduction in crystallinity observed during adsorption tests is particularly significant because it negatively affects CNC thermal stability and is expected to compromise the mechanical properties of the material by compromising structural integrity. Physical degradation occurs via cracking in CNC clusters due to swelling during water uptake and drying stress, as well as mass loss from the hydrolysis of adsorbed water. There was no significant difference in mass loss between humidity treatments during 2-week storage tests at 45°C (i.e., 0% v. 96% v. 100% RH). Additionally, the detection of microbiological growth during the storage test was inconclusive. The hydrolysis mechanism of water adsorption is identified as the primary pathway for the reduction in crystallinity of CNC caused by exposure to various humidity isotherm treatments. Other physical changes observed in adsorption tests included increased surface smoothness in high-temperature-treated CNC (60°C), due to the reorganization of individual crystals during water diffusion. Lastly, surface charge degradation from adsorption treatments made CNC more susceptible to agglomeration due to reduced colloidal stability. TEM observations support these interpretations of zeta potential data. It is recommended to perform a longer-term storage experiment to determine whether the degradation rate remains constant, accelerates, or decelerates over time under warm, humid conditions. The mass losses should also be further evaluated to determine the dominant pathways among hydrolysis, dehydration, and

potential biodegradation. Moreover, identification of the species involved in potential microbiological feeding and/or growth would provide valuable insight into the definition of the biodegradation mechanism.

CHAPTER FOUR

PRODUCTION AND CHARACTERIZATION OF SUGAR BEET BASED CELLULOSE NANOCRYSTALS

Contribution of Authors and Co-Authors

Manuscript in Chapter 4

Author: Daniel Blake

Contributions: Investigation, Analysis, Writing – Original draft, Visualization

Co-Author: Adam Gladen

Contributions: Supervision, Writing – Review, Editing

Co-Author: Navid Anjum

Contributions: Analysis

Co-Author: Dilpreet Bajwa

Contributions: Supervision, Writing – Review, Editing

Manuscript Information

Daniel Blake, Adam Gladen, and Dilpreet Bajwa

Reviews on Advanced Materials Science

Status of Manuscript:
__X__ Prepared for submission to a peer-reviewed journal
_____ Officially submitted to a peer-reviewed journal
_____ Accepted by a peer-reviewed journal
_____ Published in a peer-reviewed journal

Abstract

Cellulose nanocrystals (CNCs) are nanoparticles commonly extracted from woody biomass such as white pine via sulfuric acid hydrolysis methodology. CNCs have generated significant interest in recent years due to its notable properties: high mechanical strength, high aspect ratio, high surface area, and a liquid crystalline nature. CNCs may also undergo chemical modification easily to adjust material properties such as thermal stability, hydrophilicity/hydrophobicity, and surface charge. In this study, several CNC types were produced using phosphoric acid (P-CNC), phosphoric/sulfuric acid blend (PS-CNC), nitric acid (N-CNC), nitric/sulfuric acid blend (NS-CNC), and sulfuric acid control (S-CNC) to investigate the impact of acid choice and/or changes in functionalization (i.e. sulfate, phosphate, nitrate) on CNC composition and properties. CNCs were produced from sugar beet pulp (SBP) and characterized to report mass yield, zeta-potential, degree of functionalization, crystallinity, and cellulose content. The CNCs made from SBP were characterized and compared alongside a commercial product (i.e. control CNC) made from white pine through the standard sulfuric acid hydrolysis. It is revealed that CNCs produced from SBP (SBPCNCs) possess lower cellulose content, zeta-potential, crystallinity, and a larger aspect ratio than the commercial CNC. The CNCs made using phosphoric acid (P-CNC and PS-CNC) exhibit potential for use in material development because of minor crystallinity and cellulose content reduction and increased reaction mass yield relative to the CNCs made from SBP using sulfuric acid (S-CNC). Phosphoric acid also diminishes the harshness of the hydrolysis as it is less caustic than sulfuric or nitric acid. The elemental composition of SBPCNCs was measured using energy dispersive spectroscopy, which reveals successful functionalization of CNC by phosphoric and/or sulfuric acid whereas nitric acid is ineffective. The degree of functionalization in S-CNC is greatest followed by PS-CNC and then P-CNC. Water uptake experiments were performed on SBPCNCs

and commercial CNC and reveal that P-CNC experiences the most water uptake at 40% and 70% RH followed by PS-CNC. The greater water uptake of P-CNC and PS-CNC is attributed to their increased amorphous fraction versus S-CNC and commercial CNC rather than functionalization.

Keyword: Cellulose nanocrystal, Phosphoric acid, Nitric acid, Sulfuric acid, Acid blend, Characterization

Introduction

Cellulose nanocrystal (CNC) is a popular material in various realms of research because of its desirable properties and sustainability [167]. CNC is often produced via sulfuric acid hydrolysis from biomass sources for commercial production, in which the chemical treatment dissolves the amorphous components [168]. These biomass sources are either woody or non-woody [169]. White pine is the standard (woody) biomass in commercial production of CNC because of the high theoretical yield given the high cellulose content and crystallinity, relatively. However, there are other biomass' that may be used for CNC production to supply the need for this material in research and development projects. Producing CNCs is often costly but may be accomplished from waste materials such as pressed sugar beet pulp (SBP) to improve economics [170] The waste material retains lignocellulosic components which may be used to yield CNC. It is preferable to find some use for these waste biomass by-products for high value applications [171]. Still, there is unmet potential for waste biomass in supplying the production of more valuable products such as CNC.

Sugar beets are used as a primary crop for sugar production, yet there is a sizable amount of biomass that remains after the desired sugars have been extracted. In other research, SBP has been proven as a valuable material in animal feeds for cattle, pigs, and horses because of the beneficial impacts to gut health [172]. Although these applications have been found to be suitable,

there has been increased demand for CNC in material development; composites in particular. SBP is known to contain ~23% cellulose content post-extraction of sugars, which is significant enough for cellulose nanocrystal production of this otherwise waste by-product. CNC production is often costly but may be accomplished from waste materials such as pressed SBP to improve economics [173]. The process is often achieved by means of acid hydrolysis in which non-crystalline components are dissolved such as hemicellulose and amorphous cellulose. The waste material retains lignocellulosic components which may be used to yield CNC. Although cellulose represents 20-25% of mass abundance in SBP, only crystalline cellulose may be used to produce CNC. Crystalline cellulose is known to represent near 50% of cellulose mass in herbaceous biomass and near 70% in woody biomass [174]. SBP is more herbaceous than woody so the maximum CNC mass yield is predicted to be ~10% from untreated starting material. The potential yield further validates the research performed on optimizing pretreatments. It is essential to define reaction parameters of the highest efficiency so that the process may remain economically viable.

SBP is often received frozen; then stored at -20°C to prevent material decomposition. The pulp is oven-dried at 70°C before use. Dried SBP is manually ground and sieved to a maximum particle size of 250μm before treatment. Pressed SBP is reported to have a cellulose content of ~23%, which has been confirmed by HPLC analysis. Cellulose is composed of glucan whereas the hemicellulose of SBP is composed of primarily arabinan and xylan [175]. Lignin content is defined by ‘Klason lignin’ which is acid insoluble. The main drawback of CNC production methods is caused by the presence of lignin [176]. The majority of lignin that is present in biomass is commonly klason lignin, which contaminates CNC if not initially removed [177]. Lignin content is seen to increase from 2% to 13% between raw SBP and the hydrolyzed product. It is apparent that acid hydrolysis of untreated SBP causes the concentration of lignin to increase in remaining

solids by reducing the dissolving of acid-soluble constituents (i.e. hemicellulose and amorphous cellulose). The persisting presence of klason lignin also seems to prevent the complete removal of hemicellulose, in addition to contaminating CNC, by binding to cellulosic components. Therefore, it is necessary to remove klason lignin before beginning acid hydrolysis by various pretreatments.

In this study, SBP is used to produce CNC with various mineral acids. The methodology of CNC production had been optimized in 2006 by Bonderson et al. in which purified cellulose was hydrolyzed using sulfuric acid [177]. The reaction conditions for sulfuric acid hydrolysis in this experiment were adopted from the procedure outlined by the optimized reaction. These conditions include a sulfuric acid concentration of 64% (w/w) and a reaction temperature of 45˚C for 45 minutes of treatment with stirring. Sulfuric acid hydrolysis of cellulose is known to result in the insertion of sulfate groups onto the CNC surface during hydrolysis, which contribute to material hydrophilicity because of its oxygen density. However, the sulfate groups are also known to initiate thermal decomposition. In this study, SBP is pretreated using traditional pretreatment methodology with varying acid hydrolyses. The goal of the experiment is to investigate the impact of varying functionalization of CNCs on material properties. Since sulfate groups are inserted onto CNC during sulfuric acid hydrolysis, it can be assumed that phosphate groups would be inserted during phosphoric acid hydrolysis and nitrate groups during nitric acid hydrolysis. Given the impact of material composition on material properties, it is worthwhile to investigate how the properties of CNC may change as functionalization is altered.

CNC produced via sulfuric acid hydrolysis methodology is known to contain numerous sulfate half-ester groups throughout resulting crystals as depicted in *Figure 4.1* [178]. Although CNC is known to be hydrophilic because of the abundance of hydroxyl groups on its surface, sulfate groups are more hydrophilic than hydroxyl groups by possessing a higher oxygen count

and density in addition to a more negative charge. Therefore, CNC possessing a higher degree of sulfonation is anticipated to exhibit higher hydrophilicity. Modification of CNC functional groups has been proven to effect material thermal stability as well [179]. Vanderfleet et al. exemplified the technique by investigating the thermal degradation of CNCs prepared using sulfuric and phosphoric acids [180]. The results proved that CNCs produced using phosphoric acid are more thermally stable than CNCs produced using sulfuric acid. However, phosphate effects on CNC hydrophilicity are yet to be determined. Phosphate groups are similar to sulfate groups in that both possess high oxygen count and negative charge, which is indicative of hydrophilicity [181]. Additionally, the presence of sulfate groups has been proven to encourage greater dispersion of CNCs by means of electrostatic forces [182]. Therefore, it is practical to observe changes in material properties of CNC by maintaining some degree of sulfonation while introducing some additional functional group.

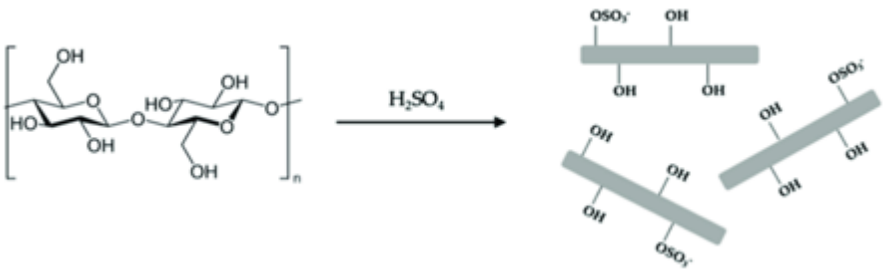

Figure 4.1 Functionalization of CNC by sulfuric acid hydrolysis.

It is known that hydrogen bonding occurs between hydrogen and oxygen, nitrogen, or fluorine [183]. Therefore, the presence of nitrate and/or phosphate groups may enhance the hydrophilicity of CNC via hydrogen bonding of water molecules. Although sulfate groups are oxygen dense, the presence of oxygen and either nitrogen or electron-dense phosphates may further encourage the hydrogen bonding which is heavily associated with CNC hydrophilicity [184]. It is hypothesized that nitric and phosphoric acid hydrolyses may result in more hydrophilic

CNC due to the positive effect that nitrate and phosphate groups may have on hydrogen bonding [185]. Furthermore, it is reported that nitric acid hydrolyses may result in CNCs with a higher thermal stability limit based on previous published research [186]. Given the nature of SBP, it is also necessary to purify the cellulose of the biomass before acid hydrolysis. The purification of cellulose from various biomass is most commonly conducted via alkali treatment with NaOH followed by bleaching treatment with $NaClO_2$ and acetic acid (CH_3COOH) [187]. The primary purpose of NaOH treatment is to weaken hemicellulose linkages so that the component may be isolated more easily during acid hydrolysis [188]. These effects also benefit the removal of lignin which is often accomplished by bleaching via $NaClO_2$ [189].

The strength of the pretreatment depends on the cellulose content of the biomass, or in other words, the amount of material which must be removed/dissolved to yield a pure cellulose product. Although CNC is a renewable and sustainable material sourced from a variety of biomass, the chemical procedures that are used to purify and hydrolyze cellulose require the handling and disposal of hazardous waste. It is acknowledged that nitric acid hydrolysis is not an improvement from the standard sulfuric acid hydrolysis in terms of environmental benefit. However, it is worthwhile to investigate the properties of CNCs produced with nitric acid in the interest of scientific research. Phosphoric acid is a weaker acid with a pK_{a1} of 2.15 ($H_3PO_4/H_2PO_4^-$), a pK_{a2} of 7.20 ($H_2PO_4^-/ HPO_4^{2-}$), and a pK_{a3} of 12.38 (HPO_4^{2-}/PO_4^{3-}) whereas the pK_{a1} and pK_{a2} of sulfuric acid is -3.0 and 1.92, respectively, and the pKa of nitric acid is -1.30 [190]. Therefore, phosphoric acid does not fully dissociate as the nitric and sulfuric acid do and is less effective as a hydrolysis reagent. The reaction conditions of alternative acid hydrolyses are more intense than the standard sulfuric acid hydrolysis. However, the properties which functionalized CNCs exhibit may validate using these more intense processes. It is proposed that the chemical modification of CNC using

phosphoric acid during acid hydrolysis may result in CNCs demonstrating improved thermal stability and water adsorption abilities.

Materials and Methods

Pressed SBP biomass was obtained from American Crystal Sugar (ACS) located in Fargo, ND as the cellulose source for CNC production. Sodium hydroxide (≥97%) and acetic acid (99.7% w/w) was purchased from Fisher Chemical (Pittsburgh, PA). Sodium chlorite (80 wt%; analytical grade) was purchased from Acros Organics (Antwerp, Belgium). Conc. H_2SO_4 (95-98%) was purchased from Fisher Chemical (Pittsburgh, PA) Phosphoric acid (85+% w/w; extra pure) was purchased from Thermo Scientific (Waltham, MA). Nitric acid (~70% w/w; technical grade) was purchased from Fisher Chemical (Pittsburgh, PA). Dialysis tubing (12-14k Dalton pore limit) was purchased from Sigma-Aldrich (Burlington, MA). Sodium chloride (99%) was purchased from Sigma-Aldrich (Burlington, MA).

SBP Pretreatment

Pretreatments conditions have been adapted based on research by Li et al. in which cellulose nanofibers (CNF) were prepared from de-pectinated sugar beet pulp [191]. Pretreatment conditions have been altered based on research presented by Hietala et al. in which CNF is also prepared from sugar beet residue [192]. **S**BP was oven-dried at 70°C for 48 hours; then ground and sieved to particle size < 250 micron before treatment. The SBP granules were first subjected to alkali treatment using 2% (w/V) NaOH at 80°C for 2 hours to weaken hemicellulose linkages and dissolve water solubles. The alkali-treated material is then vacuum filtered and washed with deionized water to remove residual NaOH before bleaching treatment. Alkali-treated pulp is then subjected to bleaching using 2% (w/V) $NaClO_2$ with 10% (V/V) acetic acid addition to the reaction

mixture to oxidize and dissolve remaining cellulose impurities. The bleached material is vacuum filtered and washed with deionized water to remove residual $NaClO_2$ and acetic acid before acid hydrolysis. Acid blends of phosphoric/sulfuric and nitric/sulfuric were mixed using an 8:1 molar ratio based on conditions used in previous published research [193]. Since sulfuric acid is the strongest among the 3 mineral acids in terms of acidity, the minority fraction of sulfuric acid in these blends functions as a catalyst during the hydrolysis of cellulose and may then allow for a more effective hydrolysis via nitric or phosphoric acid.

Acid Hydrolysis Process and CNC Extraction

The various acid hydrolysis reactions are all quenched using 10x volume of deionized water and cooled at 4°C to allow for sedimentation of the hydrolyzed material. The liquid is poured off and CNCs are washed heavily with deionized water to remove residual acid and other soluble impurities to yield a suspension. CNCs are then washed excessively with deionized water via centrifugation at 9000RPM for 10 minute cycles until pH ~5.0. These washed and concentrated CNC suspensions are isolated and mechanically homogenized (IKA, T25DS1; Staufen im Beisgau, Germany) at 1000RPM for 1 minute to break aggregates before dispersing via ultrasonication (Hielscher, UIP1000hd) at 60% amplitude power for 5 minutes. These dispersed suspensions are washed even further via dialysis in which concentrated CNC solutions are loaded and sealed in dialysis tubing. Dialysis of CNC suspensions is performed using 10x volume of deionized water, which is replaced daily over the course of 5 days. After dialysis, the CNC suspensions were subjected to 5 minutes of mechanical homogenization followed by ultrasonication at 60% for 5 minutes to disperse CNC suspensions before obtaining the final product via lyophilization (SP Scientific, Advantage Pro; Warminster, PA). CNCs were air-dried to a gel to reduce moisture content and freeze-dried for 48 hours to yield the study samples: sulfuric CNC (S-CNC; control),

phosphoric CNC (P-CNC), phosphoric/sulfuric CNC (PS-CNC), nitric CNC (N-CNC), and nitric/sulfuric CNC (NS-CNC). The mineral acids which were used to produce the CNC samples are incorporated into the CNC acronym as a means to efficiently communicate information and will be referred to as such for the remainder of the article.

Phosphoric Acid Hydrolysis

Phosphoric acid hydrolysis was performed using a reaction temperature of 100°C and reaction time of 2 hours with 10.56M acid concentration. Equivalent reaction conditions were selected for 8:1 the phosphoric and sulfuric blend hydrolysis.

Nitric Acid Hydrolysis

Nitric acid hydrolysis was performed using a reaction temperature of 80°C and reaction time of 45 minutes with 15.44M acid concentration. Equivalent reaction conditions were selected for the nitric and sulfuric blend hydrolysis.

Sulfuric Acid Hydrolysis

The control acid hydrolysis was performed using a reaction temperature of 45°C and a reaction temperature of 45 minutes with 64wt% sulfuric acid (~10.05M).

Mass Yield Measurement

CNC mass yield was measured using *Eq. 1*. SBP was dried in an oven at 70°C for 48hours and ground to a particle size of < 250 µm. The mass of the dried and ground SBP was then recorded prior to pretreatment (*SBP Mass*). SBP was subjected to alkali and bleaching treatments followed by acid hydrolysis, as outlined above. The CNCs produced by the various acid hydrolyses are

washed and concentrated before isolating the final product via lyophilization. The CNC concentrates, or gels, are freeze-dried for 48 hours and the final mass is recorded (*CNC Mass*).

Eq. 1

$$Mass\ Yield\ (\%) = \frac{CNC\ Mass}{SBP\ Mass} \times 100$$

X-ray Diffraction Analysis

CNC crystallinity was measured via powder XRD analysis (Bruker, D8 Advance Powder XRD; Billerica, MA) using the Segal method to estimate the amorphous fraction of cellulose Iβ. The estimation is then used in *Eq. 2* where *CI* is crystallinity index, I_{200} is the intensity of the 200 plane of crystalline cellulose, and I_{am} is the maximum intensity of the 'amorphous halo' occurring between crystalline peaks at approximately 18˚ 2θ [194]. The calculation yields a percentage and represents the portion of CNC which is indeed crystalline. XRD spectrums were acquired from 5-60 2θ to capture all of the relevant peaks.

Eq. 2

$$CI = \frac{I_{200} - I_{am}}{I_{200}} \times 100$$

Zeta-Potential Measurement

CNC surface charge and flocculation tendency were determined via zeta potential measurements (Zeta-Meter, System 4.0; Staunton, VA) by calculating the average of 50 individual particle charge readings. Samples were prepared following traditional methodology for CNC by dispersing CNCs in 50 mmol NaCl (aqueous) at 0.25 wt% concentration. The solution is then loaded into the Zeta-Meter cell for zeta potential measurement.

Scanning Electron Microscopy & Energy Dispersive Spectroscopy

The dry morphology of CNC was depicted via SEM (Zeiss, SUPRA 55VP; Oberkochen, Germany) at a working distance of 10 mm and an electron beam voltage of 20kV. These conditions are intense compared to usual SEM imaging settings, but these conditions are required to conduct EDS [195]. Elements detected via EDS were identified by the K-series x-ray emitted from the atom excited by the electron beam. The x-ray intensities are then measured by the instrument and given a value, which is multiplied by the element's k-ratio to yield the wt% value. The instrument is calibrated using a factory standard for each element: SiO_2 for oxygen and silicon, FeS_2 for sulfur, GaP for phosphorous, BN for nitrogen, and NaCl for chlorine.

High Pressure Liquid Chromatography

HPLC data was acquired using a BioRad Aminex HPX-87H column (Hercules, CA) and Agilent 1260 Infinity ii system (Santa Clara, CA). Sample preparation for the compositional analysis of CNCs via HPLC was adopted from the national renewable energy laboratory (NREL) established procedure (NREL/TP-510-42618) [196]. 100mg of each CNC sample was weighed using a microbalance and transferred to an autoclave tube. 1mL of 72% (w/w) sulfuric acid is added to the autoclave tube and is incubated at 30˚C for 1 hour with stirring every 5-10 minutes to dissolve the acid soluble biomass. 27mL of deionized water is then added to the mixture and the tube is sealed to be autoclaved for a 60-minute acid digestion at 121˚C/15psi. 1mL of the autoclaved solution is filtered before injection into the HPLC column; the remainder of the solution is filtered through an ashless filter paper to measure the Klason lignin content.

Fourier-Transform Infrared Spectroscopy

Fourier-Transform Infrared Spectroscopy (FTIR) spectra of powder samples were acquired using a Thermo Scientific model Nicolet iS5 system with iD7 attenuated total resonance (ATR) detection (Madison, WI). The experiment was setup using OMNIC software in which data was acquired using 64 background scans and 64 sample scans in order to produce an average from a larger sample set for data of higher quality [197].

Water Uptake Experiment

The water uptake experiment was initiated by first drying CNCs under dry nitrogen and ramping temperature from 20°C to 110°C at a rate of 7.5°C/minute; then maintaining 110°C for 20 minutes to remove any preliminary moisture. The samples were subjected to water uptake by exposure to 40% and 70% RH in a hydration chamber (ESPEC) at room temperature (~22°C) until the plateau of mass. Data points were collected every 10 minutes for the first 30 minutes, and then every 20 minutes to learn information relating to rate of water uptake as well as maximum quantity (g_{water}/g_{CNC}). Temperature and RH inside the hydration chamber were monitored by a temperature and humidity sensor (Sensirion, SHT-35; Stafa, Switzerland).

Thermogravimetric Analysis

Thermogravimetric analysis was conducted from 30°C to 600°C at a rate of 10°C/minute in a non-inert atmosphere (i.e. air) using a Discovery 5500 Thermogravimetric Analyzer (TA Instruments; New Castle, DE). Samples were held at 30°C for 5 minutes before ramping to 110°C and holding for 10 minutes to evaporate any moisture. Temperature was then ramped to 600°C and held for 10 minutes to cause thermal decomposition.

Results

It is found that the phosphoric acid hydrolysis of pretreated sugar beet pulp achieves the highest mass yield of 22.48% followed by the phosphoric/sulfuric acid blend. The mass yield of the reactions decreases as the strength of the acid or acid blend increases. Although the mass yield of S-CNC is the lowest among all reactions, it possesses the highest cellulose content. These findings indicate that sulfuric acid is the most selective in purifying and hydrolyzing cellulose. All CNCs received an identical pretreatment before acid hydrolysis. The mass yield of alkali treatment averages 63.34% whereas the mass yield of bleaching treatment averages 93.45%. S-CNC also possesses the highest crystallinity which further verifies that sulfuric acid is selective and efficient in producing CNCs, given that the reaction has the lowest temperature and shortest reaction time. These results also display a trend of increasing zeta potential magnitude as acid strength is increased. CNCs produced using phosphoric acid have the lowest zeta potential magnitude but the colloids are still considered stable. The standard deviations of zeta potentials were deduced from raw data points whereas the standard deviation of cellulose content was deduced using data points from the HPLC calibration curve. The error for crystallinity values was adapted from the original published method in which the standard error was reported to be 6.5% [198]

Table 4.1 Zeta-potential, crystallinity, cellulose content and mass yield data of CNC produced with: sulfuric acid (S-CNC), nitric/sulfuric acid blend (NS-CNC), nitric acid (N-CNC), phosphoric/sulfuric acid blend (PS-CNC), and phosphoric acid (P-CNC).

CNC	Zeta Potential (mV)	Crystallinity	Cellulose Content	Mass Yield
S-CNC	-48.15 ± 6.45	59.10% ± 6.5%	50.2% ± 0.47%	11.5%
NS-CNC	-45.55 ± 8.02	48.39% ± 6.5%	39.3% ± 0.47%	13.2%
N-CNC	-42.05 ± 7.35	51.28% ± 6.5%	33.3% ± 0.47%	17.0%
PS-CNC	-38.63 ± 5.27	57.89% ± 6.5%	41.4% ± 0.47%	20.6%
P-CNC	-35.09 ± 6.53	54.35% ± 6.5%	40.1% ± 0.47%	22.5%

Fourier-Transform Infrared Spectroscopy

FTIR spectra of all CNC samples contains a strong hydroxyl peak occurring at ~3350 cm^{-1}. This is expected for CNC as the chemical structure natural contains hydroxyl groups (*Fig. 4.1*). The strongest peak among all spectra, which occurs at ~1020 cm^{-1} is attributed to C-O stretching within the pyranose ring of the CNC backbone. The peak at ~1020 cm^{-1} may also be attributed to sulfate presence [199]. The FTIR overlaid spectra displays 3 main differences between CNC samples. The disparity appearing at 1638 cm^{-1} is attributed to carbonyl (C=O) stretching of a ketone or amide while the disparity appearing at 1280 cm^{-1} is attributed to C-O stretching of an ester. The more intense response in the fingerprint region of N-CNC and NS-CNC is attributed to the higher degree of oxidation which occurs as a result of using nitric acid.

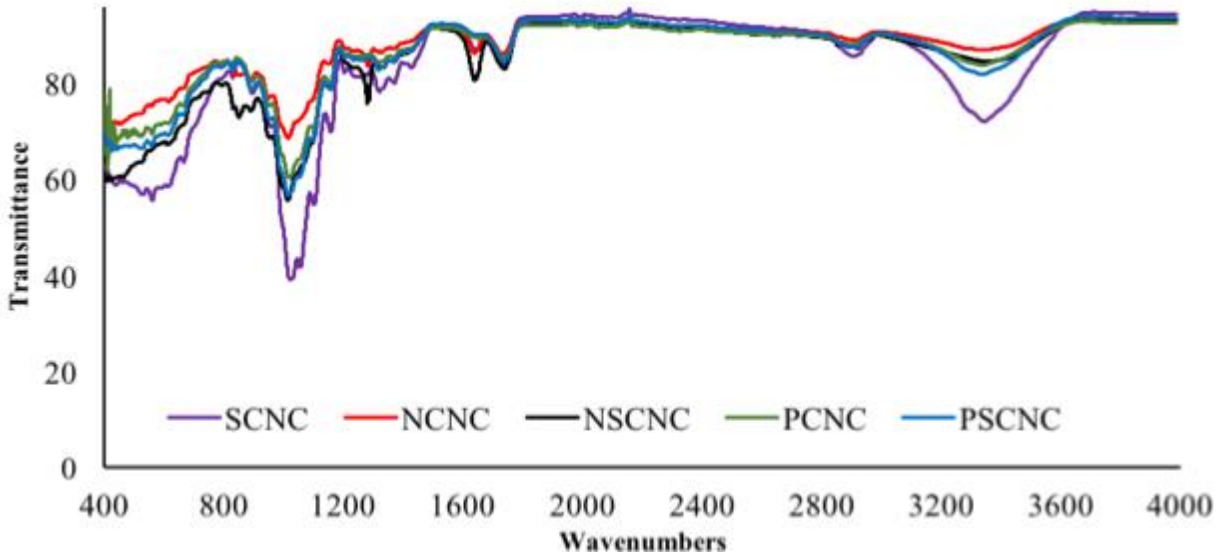

Figure 4.2 FTIR overlay of CNC produced with: sulfuric acid (S-CNC; purple), nitric/sulfuric acid blend (NS-CNC; black), nitric acid (N-CNC; red), phosphoric/sulfuric acid blend (PS-CNC; blue), and phosphoric acid (P-CNC; green).

High Pressure Liquid Chromatography

HPLC compositional analysis revealed a low cellulose content of CNCs as well as hemicellulose and lignin remaining. The persistence of hemicellulose and lignin along with low cellulose content indicate an incomplete hydrolysis and the need for more intense pretreatment to increase the purity of cellulose before hydrolysis. S-CNC has the highest cellulose content of 50.2%, PS-CNC is 41.4%, P-CNC is 40.1%, NS-CNC is 39.3%, and N-CNC is 33.3. S-CNC also has the highest lignin fraction of 4.0%, which is due to the greater dissolution of other impurities during sulfuric acid hydrolysis. Therefore, the insoluble lignin increases in mass % as its mass remains the same but other biomass such as hemicellulose and uronic acids is dissolved. N-CNC and NS-CNC possess the lowest mass fraction of hemicellulose, which is attributed to the oxidizing abilities of nitric acid in addition to its acidity.

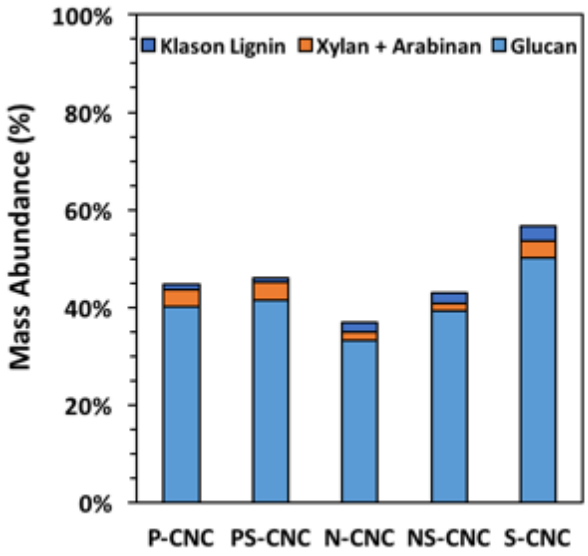

Figure 4.3 HPLC mass abundance of lignocelluloses in CNC produced with: sulfuric acid (S-CNC), nitric/sulfuric acid blend (NS-CNC), nitric acid (N-CNC), phosphoric/sulfuric acid blend (PS-CNC), and phosphoric acid (P-CNC).

X-ray Diffraction Analysis

The crystallinity of CNCs was investigated via XRD scan from 5° to 60° 2θ to capture all relevant peaks. It should be noted that the curved baseline beneath each XRD pattern is representative of the estimated amorphous fraction pattern by the XRD software (Bruker, DIFFRAC.SUITE). The crystalline peaks of CNC among all samples appear at an identical 2θ as shown in *Figure 4.4* with the exception of nitric acid CNCs which appear to be shifted slightly left. This indicates that the lattice parameters, and therefore the crystal structure, of CNC was not altered by the phosphoric and control acid hydrolyses, but appears to be altered by nitric acid hydrolyses. After calculation via the Segal method (*Eq. 2*), it is revealed that the crystalline fraction of alternative acid CNCs are reduced relative to control (i.e. S-CNC). S-CNC's crystalline fraction is 59.10% whereas PS-CNC's is 57.89%, P-CNC's is 54.35%, NS-CNC's is 48.39%, and N-CNC is 51.28%. XRD spectra of S-CNC, NS-CNC, N-CNC, and P-CNC contain additional 'stray' peaks appearing most prominently at ~27° and ~40° in S-CNC. Analysis using XRD software (JADE) revealed that these CNCs contain quartz contamination in samples. It should be noted that there is no concern of quartz contamination skewing the baseline of the amorphous 'halo' in Segal method calculations because quartz contributes an amorphous fraction which is negligible [200].

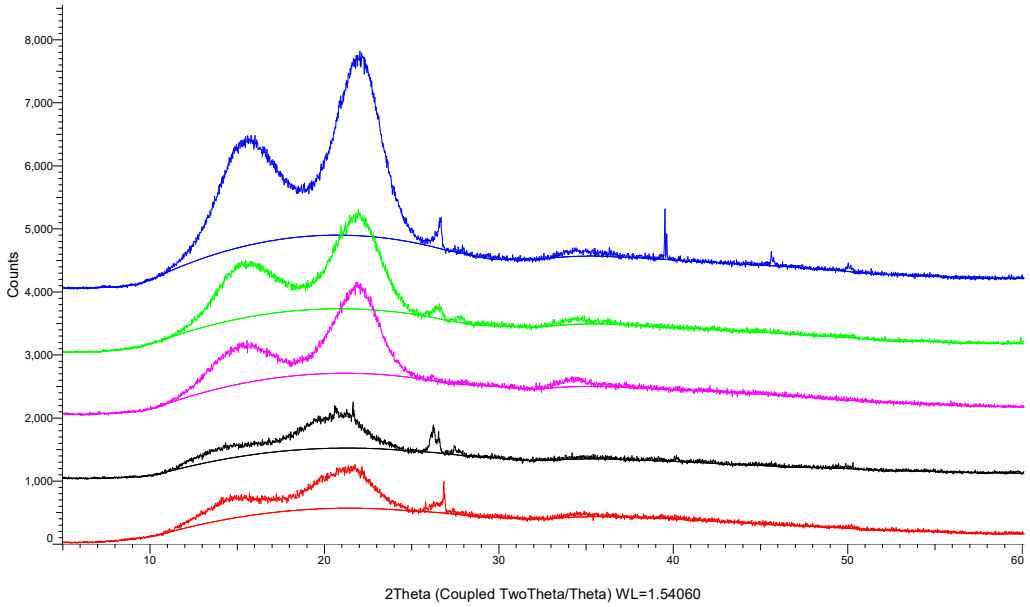

Figure 4.4 XRD stacked spectra of CNC produced with: sulfuric acid (S-CNC), nitric/sulfuric acid blend (NS-CNC), nitric acid (N-CNC), phosphoric/sulfuric acid blend (PS-CNC), and phosphoric acid (P-CNC) from 5° to 60° 2θ

Energy Dispersive Spectroscopy

EDS results confirm the presence of phosphorous in P-CNC, phosphorous and sulfur in PS-CNC, and sulfur in S-CNC and NS-CNC. However, there is no nitrogen detected in NS-CNC nor N-CNC due to lack of functionalization. Carbon has been omitted from the element detection so that only wt% of elements which occur in functional groups is measured. The oxygen content is dominant because of its existence in the makeup of cellulose repeating units and branching hydroxyls. Still, the oxygen content of P-CNC and PS-CNC is higher than that of S-CNC (Control), which is encourages hydrophilicity [184]. N-CNC also contains a high oxygen content, but is attributed to the oxidation caused by nitric acid during hydrolysis. The Si which is detected is attributed to the silicon sheet that samples were affixed to for analysis rather than some carbon tape. Silicon was chosen so that carbon tape would not interfere with elemental analysis. Impurities such as Al and Cl most likely have been inserted to the molecular build of CNCs during the

bleaching treatment using $NaClO_2$. Given that $NaClO_2$ is the least pure reagent used in the study (~80%), it is probable that impurities such as Al were introduced during the bleaching treatment. S1 refers to site 1 of the EDS analysis, and BSI stands for back scatter image, which is used to conduct SEM-EDS analysis.

Table 4.2 EDS quantified wt% for elements of significance in functional group analysis of CNCs

Element	Control Wt%	N-CNC Wt%	NS-CNC Wt%	P-CNC Wt%	PS-CNC Wt%
O	96.51	97.73	95.60	97.51	97.91
Si	0.56	1.21	2.30	0.66	0.82
S	1.16	-	0.50	-	0.11
N	-	0.00	0.00	-	-
P	-		-	0.12	0.15
Al	-	0.05	0.11	0.11	0.24
Cl	1.08	0.09	0.08	0.10	0.76

Water Uptake Measurement and Kinetic Study

Data from the water uptake experiments on CNCs is presented in *Figure 4.5* and *Figure 4.6*. It is apparent that P-CNC attains the highest amount of water uptake at both RH levels, followed by PS-CNC. Although the rate of water uptake appears to be similar, the control CNC (i.e. commercial CNC) displays a higher adsorption rate at 40% RH, relatively. The adsorption rate appears to remain the same at 70% RH for the control CNC, but increases for SBPCNCs (i.e. S-CNC, P-CNC, PS-CNC). The control CNC does attain a higher amount of water uptake at 70% v. 40% RH, but does not display as much of an increase in the plateaued mass as SBPCNCs. The higher water uptake mass of the SBPCNCs is attributed to the presence of amorphous cellulose and other amorphous components that may still be present. It is revealed by HPLC that the composition of SBPCNCs is not as pure and SBPCNCs have a lower crystallinity than control. The remaining amorphous parts of SBPCNCs have a significant impact on interactions with water,

and cause for a higher affinity for water adsorption (i.e. hydrophilicity) [200]. At a low RH, the trend among CNCs is not as apparent. However, at 70% RH, it is clear that the water uptake increases in terms of rate and plateaued mass in the following order of: control CNC (i.e. commercial CNC), S-CNC, PS-CNC, P-CNC.

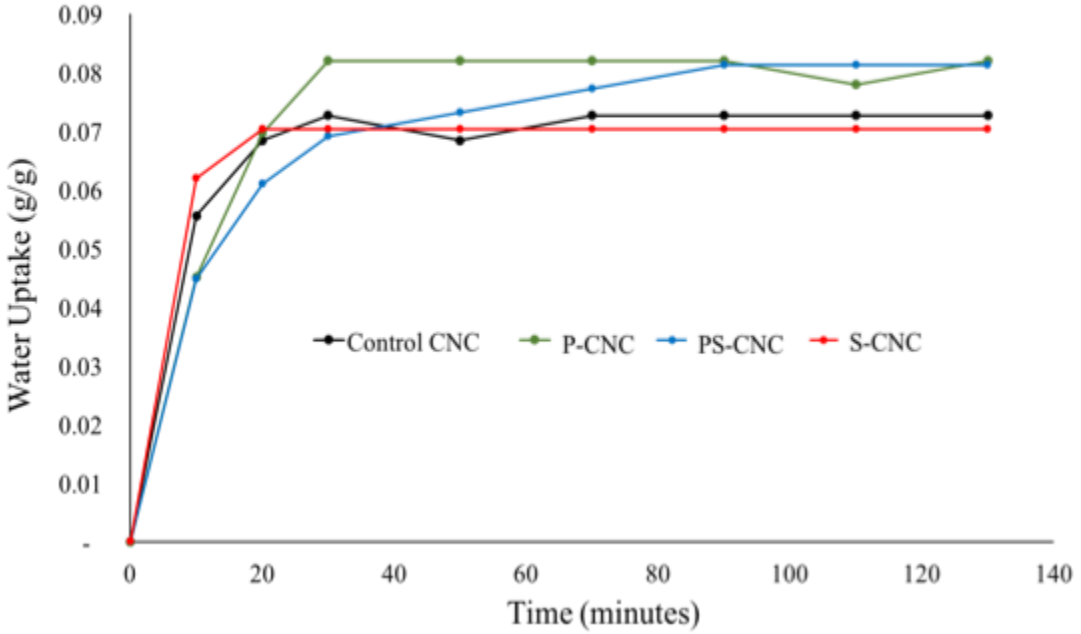

Figure 4.5 40% RH water uptake data of: control CNC (black), P-CNC (green), PS-CNC (blue), and S-CNC (red)

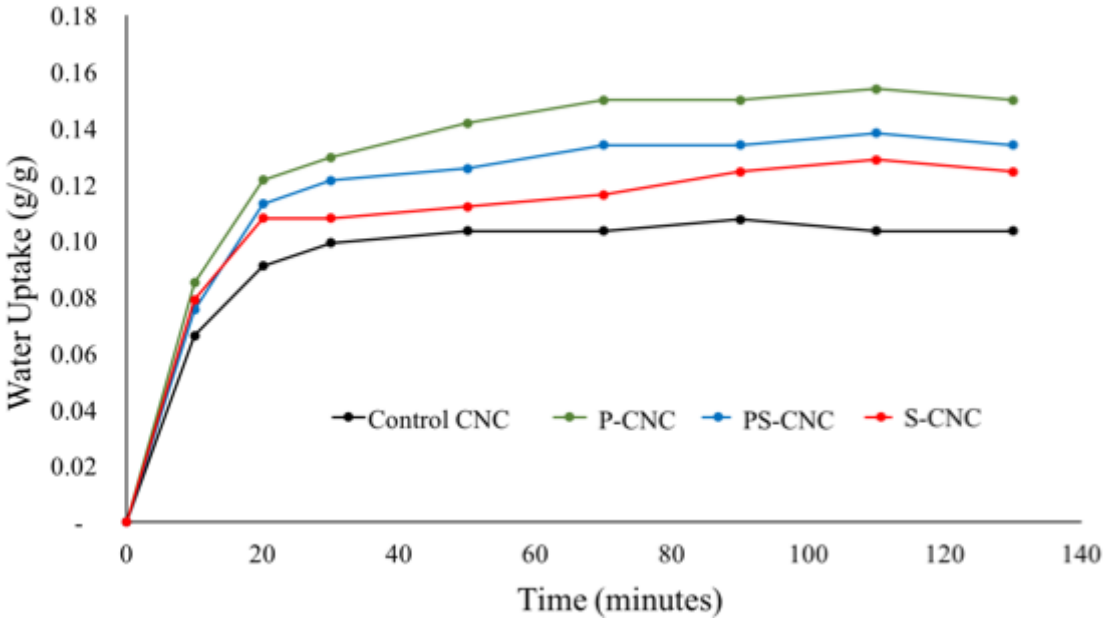

Figure 4.6 70% RH water uptake data of: control CNC (black), P-CNC (green), PS-CNC (blue), and S-CNC (red)

Thermogravimetric Analysis

TGA data for CNC samples of interest (P-CNC, PS-CNC, S-CNC, and control) is shown in *Figure 4.7*. As before, N-CNC and NS-CNC were excluded due to greater losses in crystallinity and purity relative to other CNCs. It is apparent that control CNC is characterized by the greatest thermal stability followed SBPCNCs (i.e. P-CNC, PS-CNC, and S-CNC). There is no significant difference in thermal stability between SBPCNCs. From these findings, it is likely that crystallinity is the primary factor affecting thermal stability of CNC since control CNC possesses the highest crystallinity (~79%). SBPCNCs all possess a similar crystallinity of 55-60%, so there is not much difference in thermal decomposition onset. However, the SBPCNCs retain mass after the control CNC has fully decomposed (i.e. combusted). The extended decomposition of SBPCNCs is likely due to a combination of factors including the greater presence of impurities and the larger aspect ratio.

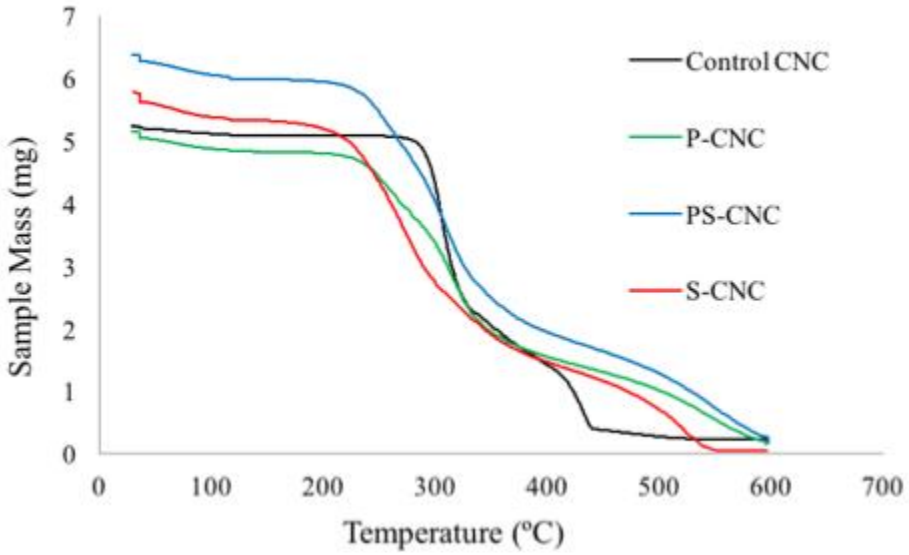

Figure 4.7 TGA data of: control CNC (black), P-CNC (green), PS-CNC (blue), and S-CNC (red) from 30°C to 600°C at 10°C/minute

Discussion

Effects of Acid Types on Compositional Analysis

CNC is produced with alternative mineral acids to potentially benefit the sustainability of CNC production in addition to valuable properties and metrics such as mass yield, crystallinity, and hydrophilicity. It is found that the mass yield of CNC production is increased as acid strength is decreased, as expected. S-CNC remains the preferred acid hydrolysis method because it has the highest crystalline fraction, surface charge magnitude, and cellulose content in addition to milder reaction conditions. However, P-CNC and PS-CNC have comparable crystallinity with a higher mass yield. The crystalline mass % in CNCs for each reaction pathway may be calculated using the following equation:

Eq. 3

$$Crystalline\ Mass\ \% = CNC\ Mass\ Yield\ \times \frac{Cellulose\ Content}{100} \times \frac{Crystallinity}{100}$$

Cellulose content and crystallinity are divided by 100 so that their quantity may be expressed as a decimal between 0 and 1 rather than a percent. In multiplying the CNC mass yield by these variables, the crystalline mass percentage may be determined. These values for S-CNC, NS-CNC, N-CNC, PS-CNC, and P-CNC are: 3.41%, 2.51%, 2.90%, 4.94%, 4.90%, respectively. Therefore, PS-CNC and P-CNC reaction pathways are actually most effective in extracting CNC given the pretreatment conditions. These findings provide further evidence for the PS-CNC and P-CNC hydrolysis pathways to be used as viable options in CNC production.

It should be noted that the Segal method that is used to calculate the crystallinity percentage is an estimation of CNC crystallinity rather than an exact value. Although the method is considered to be accurate and is widely adopted throughout research, there is an associated amount of error to be accounted for in each result (i.e. 6.5%). The primary comparison between the Segal method and other crystallinity index (CI) measurements is that the Segal method is faster, but has been known to overestimate the CI value relative to more complex methods [201]. For example, a study by Nam *et al.* on the development of cotton fibers from 20 to 60 days post-anthesis (DPA) revealed that the Segal method indicated a rapid CI increase while there was a gradual increase when using other methods (i.e. FTIR) [202]. However, the method offers an accurate enough calculation for CI values to be compared if sample preparation and the XRD experiment itself remain consistent. Therefore, it has been deemed appropriate for what was needed in the study provided here. It should also be noted that the Segal method indicated a negligible influence of crystallite size on the measurement in the study by Nam *et al.* [202].

Functional Group Effects

These results also display a trend of increasing zeta potential magnitude as acid strength is increased. CNCs produced using phosphoric acid have the lowest zeta potential magnitude but the colloids are still considered stable. It should be noted that NaCl concentration is an extremely significant factor in zeta potential readings. As more salt is added to the CNC suspension, there is more surface charge shielding that occurs [203]. The primary function of NaCl in zeta-potential measurement is to envelope individual particles so that there are numerous colloids to choose from during data acquisition. Therefore, it is essential to maintain the same NaCl concentration across samples so that the surface charges may be properly compared. The greater zeta-potential magnitude of S-CNC is attributed to the more efficient hydrolysis which occurs. Since the mass yield of sulfuric acid hydrolysis is the lowest at 11.5%, it is apparent that there is greater hydrolysis of biomass resulting in more charged moieties on the cellulose surface [204]. The specific functional groups seem to have an insignificant impact on the surface charge of CNCs compared to the degree of hydrolysis.

There is no nitrogen detected in NS-CNC and N-CNC, but the standard deviation of the measured wt% is 1.40% for NS-CNC and 1.97% for N-CNC. The nitrogen content is most likely to low to be measured via EDS. Phosphorous is detected in P-CNC and PS-CNC, and sulfur is detected in S-CNC, PS-CNC, and NS-CNC. These findings indicate that phosphoric acid and sulfuric acid hydrolyses do result in the insertion of phosphate and sulfate groups onto CNC particles given the reaction mechanism. Elemental analysis reveals that sulfate groups are more efficiently inserted onto CNC particles than phosphates because of the high relative wt% of sulfur in S-CNC compared to phosphorous in P-CNC. Interestingly, a higher amount of phosphorous is detected in PS-CNC than in P-CNC, which is in alignment with previous research [205]. These

findings verify that sulfuric acid may be used as a catalyst in acid hydrolysis using alternative acids.

The hydrophilicity of CNCs does appear to be affected by alternative acid production. The figures shown for the water uptake experiment (*Fig.4.5* and 4.*6*) reveal greater water uptake events in P-CNC and PS-CNC at 40% and 70% RH. The significance of the differences in water uptake is a result of the difference in composition of CNCs, as amorphous materials normally exhibit greater water uptake [206]. However, the difference may also be attributed to changes in functionality, which are directly involved in the mechanism of water adsorption [207]. The trend in water uptake among CNCs is more apparent at 70% RH (*Fig. 4.6*) than at 40% RH (*Fig. 4.5*) because of stronger treatment. Since the water activity is higher at 70% RH, the differences in water uptake between samples are more dramatized [208]. Interestingly, control CNC is characterized by the lowest and slowest water uptake whereas P-CNC is characterized by the greatest and fastest water uptake (at 70% RH). Hydrophilicity is expected to correlate positively with zeta potential magnitude, depending on the functional group, because of water's polar nature [209]. However, water uptake increases as surface charge is reduced in CNCs, and the zeta potential data of these CNCs has contradicted what was expected. Therefore, the trend in water uptake may either be attributed to the amorphous components of SBPCNCs, or the differences in functionality between samples.

It is likely that the higher water uptake of SBPCNCs is a direct result of higher amorphous composition relative to control CNC. Materials comprised of amorphous components rather than crystalline are known to experience greater water adsorption/absorbance and swelling because of their less ordered nature [210]. HPLC results (*Fig. 4.3*) reveal decreased purity in the following order: control CNC, S-CNC, PS-CNC, P-CNC. The only crystalline contribution of SBP is from

cellulose, so as the purity of CNCs decreases there is an increased amorphous fraction [211]. The difference in purity is not much between PS-CNC and P-CNC, but there is improved hydrophilicity exhibited by P-CNC. The difference in water uptake performance between P-CNC and PS-CNC is attributed to a greater amorphous fraction of P-CNC. Although the P-CNC hydrolysis pathway is proven to be more efficient in extracting CNC because of the overall crystalline mass yield from raw SBP, there is a lower crystallinity of P-CNC relative to PS-CNC (54.35% v. 57.89%). The amorphous fraction of P-CNC is only greater by ~3% but, apparently, provides an impact to its water uptake performance at high RH (70%). There do appear to be differences in functionality between P-CNC and PS-CNC via EDS data because of greater P and S content in PS-CNC (*Table 4.3*). However, it is insignificant in terms of hydrophilic enhancement. The greatest variation to hydrophilicity of CNCs is a result of the remaining amorphous fractions. The functionality provided by alternative acid hydrolyses does not seem to impact water uptake performance, or is not functionalized enough to directly affect interactions with water [212].

CNC Production Improvements

HPLC analysis of all sugar beet CNCs reveals a lower cellulose content compared with the commercial CNCs that can be purchased [213]. It is likely that the low cellulose content is caused by incomplete pretreatment and purification of cellulose before acid hydrolysis. There is high mass removal of near 40% during alkali treatment, which indicates an effective treatment of the biomass. However, only 3-4% of biomass is removed during bleaching treatments. Given that SBP consists of ~23% cellulose, and is most likely ~50% crystalline of the cellulose fraction, approximately ~85% mass removal is required by pretreatment to produce 100% pure CNC. A more chemically intense pretreatment is required to properly purify CNC before acid hydrolysis. Bleaching is often accomplished at particularly low reagent concentrations of near 1% (w/w) but has normally

required a repetition of the treatment to effectively remove lignin and purify cellulose [214]. The treatment effects of 2% $NaClO_2$ have been evaluated in an attempt to reduce manufacturing labor and cost by using more efficient treatment conditions with zero repetition. However, it has been revealed that repetition of the bleaching treatment is necessary to properly purify the cellulose of SBP, and a stronger alkali treatment. Acid hydrolysis conditions were defined but time constraints may be altered depending on CNC yield and aspect ratio. The reaction time may be lengthened or shortened depending on initial molecular size of cellulose components [215]. The traditional sulfuric acid hydrolysis is still the preferred method by attaining the highest crystallinity and cellulose content of all experimental reactions as well as the highest zeta potential magnitude, which is indicative of a lower flocculation tendency.

Severity factors for the pretreatment conditions that were applied have been calculated using *Eq. 4*. The severity factor is a dimensionless number that is used to measure the combined effects of chemical reactions such as temperature and time, and is particularly used in biomass pretreatment processes. The severity factor provides a method to compare the intensity of pretreatment reaction conditions. In *Eq. 4*, *T* represents temperature (in°C) and *t* represents time (in minutes) while *CSF* stands for combined severity factor.

Eq. 4

$$CSF = \log\left(t \times e^{\frac{T-100}{14.75}}\right) - pH$$

The *CSF* values for alkali and bleaching treatments are approximately -12.2 and -2.8, respectively. The pH of the alkali treatment was calculated to be 13.7 whereas the pH of the bleaching treatment was approximated to be 4.0 based on the acetic acid and sodium chlorite concentrations [216]. In the pretreatment of biomass, a negative *CSF* tends to correspond to milder conditions, while a positive *CSF* indicates more severe conditions that can solubilize more hemicellulose and lignin,

but may also degrade cellulose [217]. This information has been provided to assist in establishing suitable pretreatment conditions for the production of CNC using SBP in future endeavors.

Conclusions

Sugar beet pulp based CNC is produced with alternative mineral acids to potentially benefit sustainability of CNC production in addition to valuable properties and metrics such as mass yield, crystallinity, and hydrophilicity. It is found that the phosphoric acid hydrolysis of pretreated sugar beet pulp achieves the highest mass yield of 22.48%. S-CNC remains the preferred acid hydrolysis method because it has the highest crystalline fraction, surface charge magnitude, and cellulose content in addition to milder reaction conditions. However, PS-CNC and P-CNC reaction pathways are actually most effective in extracting CNC given the pretreatment conditions. P-CNC and PS-CNC are also of interest because of the minor reduction to crystallinity and cellulose content while increasing the mass yield of CNC. Nitric acid hydrolyzed CNCs are not recommended for common preparation and use due to the more caustic of nitric acid in comparison to phosphoric or sulfuric acid, and the reduced quality of CNC properties such as crystallinity, cellulose content (purity), and zeta potential. Nitrogen is also not detected by EDS, which is indicates the content is too low for the detectable limits of the technique. It is recommended that elemental analysis be conducted using inductive coupled plasma optical emission spectroscopy (ICPOES) to properly measure the functional group substitution with appropriate detectable limits. It is recommended that more intense pretreatment conditions be adopted to further purify cellulose before acid hydrolysis. Pretreatment conditions are intentionally assigned to be less intense for the purposes of maintaining a low environmental impact of the life cycle assessment (LCA) for CNC production from SBP. The greatest variation to hydrophilicity of CNCs is a result of the remaining

amorphous fractions. The functionality provided by alternative acid hydrolyses does not seem to impact water uptake performance, or is not functionalized enough to directly affect interactions with water.

Future Work

CNCs exhibiting enhanced hydrophilicity and thermal stability relative to purely sulfonated CNCs are used to form promising salt:CNC formulations selected from previous screenings. It should be noted that CNCs exhibiting enhanced properties may not be used if crystallinity is significantly less than the control CNC (>10%). Currently, $SrCl_2$:CNC and $SrCl_2$:$CaCl_2$:CNC composites are favored candidates based on preliminary data. 80:20 and 90:10 composition varieties are produced and subjected to performance testing. Water uptake and dehydration enthalpy values are compared to performance data of the composites containing purely sulfonated CNC. CNCs characterized by higher hydrophilicity are anticipated to promote hydration of salt:CNC materials; encouraging rapid and possibly greater energy release. Any reduction of CNC crystallinity is anticipated to impact material cycling stability because less crystallinity contributes less structural framework to salts. However, an increase in crystallinity may be observed by acid substitution experiments which is supportive of consistent and extended cycling performance. Lastly, the thermal stability of salt:CNC materials containing functionalized CNCs is measured to verify if the enhancement remains in composites. Increasing hydrophilicity of CNC is of primary importance to the study alongside maintaining or increasing crystallinity. Increasing thermal stability is desired but is of secondary importance. Therefore, acid substitution methods may be adopted if some functionalized CNC provides further enhancement to composites

under the following conditions or any combination of conditions presented in the table below. Increase is indicated by + sign; no change is indicated by 0; slight decrease is indicated by – sign.

Table 4.3 Viable conditions for acid substitution in CNC extraction

Condition	Hydrophilicity	Crystallinity	Thermal Stability
1	+	0/-	0
2	0	+	0
3	+	0/-	+

CHAPTER FIVE

SALT:CNC COMPOSITE DEVELOPMENT – THERMAL ENERGY STORAGE PERFORMANCE AND FUNDAMENTAL MATERIAL CHARACTERIZATION

Contribution of Authors and Co-Authors

Manuscript in Chapter 5

Author: Daniel Blake

Contributions: Investigation, Analysis, Writing – Original draft, Visualization

Co-Author: Adam Gladen

Contributions: Supervision, Investigation, Writing – Review, Editing

Co-Author: Navid Anjum

Contributions: Investigation, Analysis, Writing – Review, Editing

Co-Author: Sangeet Karna

Contributions: Investigation, Analysis

Co-Author: Dilpreet Bajwa

Contributions: Supervision, Writing – Review, Editing

Manuscript Information

Daniel Blake, Adam Gladen, and Dilpreet Bajwa

Reviews on Advanced Materials Science

Status of Manuscript:
__X__ Prepared for submission to a peer-reviewed journal
_____ Officially submitted to a peer-reviewed journal
_____ Accepted by a peer-reviewed journal
_____ Published in a peer-reviewed journal

Abstract

Salt hydrates have demonstrated thermal energy storage capabilities via reversible bonding of water molecules. Materials have exhibited energy densities of 400-870 kWh/m^3 at low operating temperatures (<150˚C) and are generally low-cost but prone to degradation with use. Previous efforts to improve stability have primarily focused on impregnating a porous host matrix with salt. However, the expansion of salts during hydration has led to degradation of the host matrix and salt leakage. Cellulose nanocrystals (CNCs) have shown great potential for strengthening the structural framework of composites across numerous applications. CNCs have generated significant interest due to their high mechanical strength, high aspect ratio, high surface area, liquid-crystalline nature, and hydrophilicity, which support interaction between salt and water. $CaCl_2$, $MgSO_4$, and $SrCl_2$ have been selected for the study, along with several blends ($MgSO_4$:$SrCl_2$, $SrCl_2$:$CaCl_2$, $MgSO_4$:$CaCl_2$). The goal of research is to develop and optimize promising salt:CNC composite materials for effective heat output and potential dehumidification over extended cycling periods while maintaining thermal reliability. Salts and CNCs are combined to produce composites of varying mass ratios (60:40; 80:20; 90:10). Salt:CNC systems are evaluated using transmission electron microscopy to confirm successful nucleation. Material performance is evaluated using simultaneous thermal analysis. CNC addition is found to enhance material performance in $SrCl_2$:CNC and $SrCl_2$:$CaCl_2$:CNC significantly. $SrCl_2$-containing formulations are found to possess high energy storage capabilities exceeding 600 J/g and demonstrate unique interactions with water molecules with the addition of CNC. CNC was also produced from sugar beet pulp (SBPCNC) to demonstrate a more cost-effective process to produce salt:CNC composites. Salt:SBPCNC composites were made using $SrCl_2$. Salt:SBPCNC composites exhibit lower energy storage in comparison to salt:CNC composites with control (i.e., commercial) CNC. Under study

conditions, $SrCl_2$:SBPCNC (90:10) achieves an energy storage of ~450-500 J/g, whereas $SrCl_2$:CNC (90:10; control CNC) achieves an energy storage of ~900 J/g. The discrepancies in composite performance due to CNC selection are attributed to the lower purity, crystallinity, and zeta potential magnitude of SBPCNC compared with the commercial CNC. Salt and CNC interactions are investigated using spectroscopic techniques. It is revealed that electrostatic interactions occur between CNC and the water molecules of salt hydrates, as well as unique vibrations of the composite lattice. These findings are confirmed by the detection of higher hydrated phases in composites versus pure salt hydrate (post-processing) via X-ray diffraction. CNC has also been shown to enhance material uniformity by providing a structural network for salt nucleation, as confirmed by scanning electron microscopy.

Keywords: Salt hydrates, Thermal energy storage, Thermochemical energy, Cellulose nanocrystal, Composite

Introduction

As global energy demand increases, there is a concerted effort to replace expensive and hazardous sources with sustainable energy systems. In response, the energy sector has faced particular challenges in reducing costs and extending the lifetimes of sustainable energy storage devices. The need for reliable, long-term energy has been steadily increasing globally, prompting efforts to replace the dwindling fossil fuel resources with sources that may reduce the rate of global carbonization [218]. By doing so, the efficiency of energy use in infrastructure may be enhanced either through replacement or by constructing a system that combines energy sources. Sources such as wind, solar, hydro, and biomass have received significant attention in recent years as the primary methods for decarbonization [219]. However, concerns such as reliability, accessibility,

and cost have decelerated the development of these technologies since their emergence [220]. Alternative forms of sustainable energy, such as thermochemical systems, have received recent attention as novel means of harnessing energy that can be stored and subsequently released through reversible reactions [221]. Thermal energy may be stored via three known pathways: latent, sensible, and thermochemical [222]. Latent storage occurs when energy is drawn from the surroundings to induce a phase change in a material [223]. Sensible storage occurs when the temperature of a material increases due to heat diffusion from its surroundings [224]. These pathways are commonplace but less efficient than thermochemical pathways, which involve chemical reactions that are usually reversible [225].

The benefits of thermochemical energy storage (TCES) include, but are not limited to: greater energy density, long-term storage, and minimal heat loss [226]. Hygroscopic salts generally undergo reversible thermochemical reactions with water, involving hydration (discharging) and dehydration (charging) [227]. The relationship is represented below by the following equation in which *A*/*B* is the cation/anion pair, *x*/*y* are the quantities of atoms that form the neutral salt, and *n* is the moles incorporated into the hydrate structure:

Eq.1

$$A_xB_y + nH_2O \leftrightarrow A_xB_y \cdot nH_2O + heat$$

Table 5.1 Common hydration reaction and associated energy for popular salt hydrates in TES

Salt Hydrate	Hydration Step	Theoretical Energy Density
$CaCl_2 \cdot 2H_2O$	$CaCl_2 + 2H_2O \rightarrow CaCl_2 \cdot 2H_2O$	400 kWh/m^3
$MgSO_4 \cdot 7H_2O$	$MgSO_4 + 7H_2O \rightarrow MgSO_4 \cdot 7H_2O$	777 kWh/m^3
$SrCl_2 \cdot 6H_2O$	$SrCl_2 + 6H_2O \rightarrow SrCl_2 \cdot 6H_2O$	560 kWh/m^3

The hydration process results in the incorporation of water molecules into the salt's crystal lattice, which ultimately releases heat as a byproduct of bond formation [228]. The dehydration process requires energy from the surrounding material to break these bonds. The release of heat associated with hydrate formation may be accomplished by simple immersion and solvation of the binary salt (ie., heat of solution) [229]. However, TES systems involving these thermochemical materials (TCMs) are more efficiently driven by the *adsorption* of water vapor (ie., heat of adsorption) [230]. The reverse reaction is customarily achieved by evaporation or *desorption*. The storage and subsequent release of thermal energy by these materials is desirable due to high energy density (latent heat per unit volume), small volume change between dehydrated and hydrated phases, relatively high thermal conductivity, and low toxicity [231]. These benefits, along with the mild operating conditions associated with the use of hygroscopic salts for TES, have encouraged more research into the numerous candidates known to exist ($MgSO_4$, CaCl2, SrBr2, etc.) [232]. The energy density of these materials may be defined as the energy produced by the heat released during the complete hydration process per unit volume and is often reported as kWh/m^3 [233]. Factors that are known to affect the energy density of these materials include, but are not limited to: reaction enthalpy (per mole H_2O), adsorption rate, adsorption capacity, and thermal conductivity [234]. The energy density of various common salt TCMs is shown in *Table 5.1*. The hydration mechanism of hygroscopic salts has been proposed to occur in 2 key stages: the adsorption of water vapor from the atmosphere onto the material surface, followed by the inclusion of water molecules from the surface into their final lattice positions [235]. It is the second step, which may be defined as rate limiting. Salt hydrates often exhibit intermediate or partially hydrated phases in which a stable lattice forms between the anhydrous and fully hydrated phases [236]. All phases are accessible via water adsorption, but *deliquescence may* occur beyond the fully hydrated

phase [237]. Deliquescence events in salts increase the relative viscosity on the material surface and disassemble the crystal structure [238]. The increased viscosity slows adsorption kinetics and reduces water adsorption over time.

The creation of salt TCM composites has developed as a means to enhance energy output and cycling stability by increasing the surface area of the salt crystals and offering structural support [239]. Salt TCM composite research has commonly employed an inert, porous host matrix to provide submicron pockets for crystallization [240]. Although the use of these frameworks for TES materials has improved characteristics such as adsorption/desorption rates and stability, the long-term stability desired is still not achieved, and energy density is even reduced due to lower adsorption enthalpies in the host matrices [241]. Impregnation of CNC into salt TCMs may fully expose and even enhance the number of adsorption sites by increasing the material's surface area. Therefore, the addition of CNC is hypothesized to enhance salt performance while minimizing reductions in energy density. The nano-dimensional nature of CNCs makes them suitable as nucleation agents, with an average width of 5-20 nm and a length of 100-600 nm [242]. Its water-stable crystalline form allows reliable nucleation of salt crystals while providing structural support to prevent deliquescence [243]. Moreover, CNC provides additional assistance to salt hydrates by enhancing material hydrophilicity, which may increase adsorption rates and/or induce adsorption at lower RH [244]. For these reasons, CNC is used to promote nanoscale crystal growth of TCMs and to improve their stability and water-uptake capacity. Furthermore, the use of CNC maintains the low toxicity of study materials and provides an opportunity to produce a high-value product from otherwise waste organic matter.

The proposed system for employing these composites in day-to-day use is illustrated in *Figure 5.1*, in which hydration is achieved by humidifying the salt:CNC tank, and dehydration is

achieved by solar or grid heating. The combination of salt hydrates and CNCs has not been investigated under the lens of TES by other research groups before, to our knowledge. The performance of new salt blends is also investigated during composite development. The primary goal is to extend the TES lifetime of high-performing salt hydrate by impregnating salt crystals with CNC. The ability of CNC to optimize energy storage and release of salt hydrates provides additional value to the study. Supplementing energy systems with sustainable sources has become a universal challenge as global carbon emissions continue to increase annually [245]. Salt hydrates are naturally rechargeable, rarely hazardous, and release no carbonized emissions. The addition of CNC further supports sustainability by using renewable materials. Lastly, optimizing materials for climate regulation has significant potential to conserve energy and reduce costs. Salt:CNC varieties are studied relative to their respective pure salts and salt-blend controls, as well as the CNC control. Composites were produced using both commercial CNC derived from pine wood (i.e. control CNC) and an in-house extracted CNC from sugar beet pulp (SBP). Characterization results of composites varying in CNC type (i.e. pine v. SBP) were compared to gauge material differences at nanoscale levels, which may occur as a result of CNC substitution.

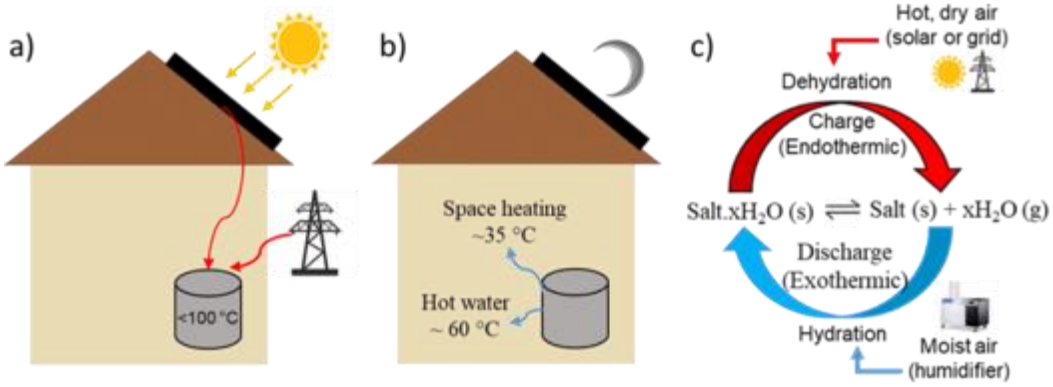

Figure 5.1 Proposed mechanism for salt hydrate TES employment in houses and other small buildings

Materials and Methods

Materials

Pressed SBP biomass was obtained from American Crystal Sugar (ACS) located in Fargo, ND, as the cellulose source for CNC production. Control CNC was obtained from the US Forest Service Labs (Madison, WI), sourced from white pine. Sodium hydroxide (≥97%) and acetic acid (99.7% w/w) were purchased from Fisher Chemical (Pittsburgh, PA). Sodium chlorite (80 wt%; analytical grade) was purchased from Acros Organics (Antwerp, Belgium). Conc. H_2SO_4 (95-98%) was purchased from Fisher Chemical (Pittsburgh, PA). Phosphoric acid (85+% w/w; extra pure) was purchased from Thermo Scientific (Waltham, MA). Dialysis tubing (12-14k Dalton pore limit) was purchased from Sigma-Aldrich (Burlington, MA). Sodium chloride (99%) was purchased from Sigma-Aldrich (Burlington, MA). Strontium chloride hexahydrate (99%) was purchased from Sigma-Aldrich (Burlington, MA). Calcium chloride dihydrate (99%) was purchased from Fisher Chemical (Pittsburgh, PA). Magnesium sulfate heptahydrate (≥99%) was purchased from Sigma-Aldrich (Burlington, MA).

SBP Pretreatment

Pretreatment conditions have been adapted based on the research by Li et al., in which cellulose nanofibers (CNF) were prepared from de-pectinated sugar beet pulp [246]. Pretreatment conditions have been altered based on research by Hietala et al., who also prepared CNF from sugar beet residue [247]. **S**BP was oven-dried at 70°C for 48 hours, then ground and sieved to a particle size < 250 microns before treatment. The SBP granules were first treated with 2% (w/V) NaOH at 80°C for 2 hours to weaken hemicellulose linkages and dissolve water-soluble components. The alkali-treated material is then vacuum-filtered and washed with deionized water

to remove residual NaOH before the bleaching treatment. Alkali-treated pulp is then subjected to bleaching using 2% (w/V) $NaClO_2$ with 10% (V/V) acetic acid addition to the reaction mixture to oxidize and dissolve remaining cellulose impurities. The bleached material is vacuum filtered and washed with deionized water to remove residual $NaClO_2$ and acetic acid before acid hydrolysis.

Acid Hydrolysis Process and CNC Extraction

Acid hydrolysis was performed at 45°C for 45 minutes using 64 wt% sulfuric acid (~10.05 M). The reaction mixture is quenched with 10x volume of deionized water and cooled to 4°C to allow sedimentation of the hydrolyzed material. The liquid is poured off, and the CNCs are washed thoroughly with deionized water to remove residual acid and other soluble impurities, yielding a suspension. CNCs are then washed excessively with deionized water via centrifugation at 9000 RPM for 10-minute cycles until the pH is ~5.0. These washed and concentrated CNC suspensions are isolated and mechanically homogenized (Make, Model) at 1000 RPM for 1 minute to break aggregates, then dispersed via ultrasonication (Hielscher, UIP1000hd) at 60% amplitude for 5 minutes. These dispersed suspensions are further washed via dialysis, in which concentrated CNC solutions are loaded into dialysis tubing and sealed. Dialysis of CNC suspensions is performed using 10x the volume of deionized water, which is replaced daily for 5 days. After dialysis, the CNC suspensions were subjected to 5 minutes of mechanical homogenization followed by ultrasonication at 60% for 5 minutes to disperse the CNC suspensions before obtaining the final product via lyophilization (Make, Model). CNCs were air-dried to a gel to reduce moisture content and freeze-dried for 48 hours to yield SBPCNC. The phosphoric acid:sulfuric acid blend was mixed at an 8:1 molar ratio, as reported in previous publications [248]. Since sulfuric acid is stronger in terms of acidity, the minority fraction of sulfuric acid in the blend may function as a

catalyst during the hydrolysis of cellulose to allow for a more effective hydrolysis via phosphoric acid [249].

Salt:CNC Composite Formulation

The quantity of SBP used to produce CNC is scaled to yield enough material for the synthesis of salt:CNC pairs using CNC derived from SBP. It is anticipated that at least 100 grams of SBP will be needed to produce 10 grams of CNC, based on the glucan composition in previous compositional analyses. The process is scaled to 100g of SBP starting material to meet the required specifications. Previously used CNC (sourced from white pine) is substituted by CNC produced from SBP in the salt:CNC formulation procedure. Current promising candidates include $SrCl_2$:$CaCl_2$:CNC (80:20 and 90:10 – salt:salt) and $SrCl_2$:CNC. CNCs obtained from SBP are dissolved in aqueous solution at a concentration of 2.5% w/V. The solution is mechanically homogenized at 1000 RPM for 1 min and ultrasonicated at 60% output for 5 min before dropwise addition to 10% w/V previously ultrasonicated salt solution at 100% output for 5 minutes. The composite solution is then ultrasonicated at 60% output for 5 min, before drying. Materials are initially air-dried under ambient ventilation and then oven-dried at 70°C to complete dryness. Dried salts and composites are manually ground and sieved through a 60-mesh screen to obtain final products for analysis. CNC was prepared from beet pulp using phosphoric acid (P-CNC) and used to produce salt:CNC formulations. ($SrCl_2$).

Thermal Energy Storage Measurement

Composites and salt controls were first dried at 110°C in a high-temperature tube furnace under a dry nitrogen flow. Then the samples were hydrated at ambient temperature (~21℃) and

70% RH using an environmental chamber (ESPEC, EPL-2H; Hudsonville, MI) until water uptake equilibrium was reached. Temperature and RH monitored by a temperature and humidity sensor (Sensirion, SHT-35; Stafa, Switzerland). The dehydration enthalpy was measured using a Simultaneous Thermal Analyzer (STA) (Perkin Elmer, 8000). For enthalpy measurement, the sample was heated from 30℃ to 100℃ at 2℃/min in a flow of dry nitrogen.

Transmission Electron Microscopy

CNC morphology of individual crystals was depicted via TEM (Zeiss, LEO 906; Oberkochen, Germany) using an electron beam voltage of 100kV and 3% uranyl acetate stain to assist contrast during imaging. The samples were prepared in aqueous media at a concentration of 0.25 wt%. During composite preparation, distinct samples are collected for TEM from the composite and from individual salt solutions of 5-10mL. Samples are ultrasonicated immediately before analysis. Salt solutions are ultrasonicated at 100% output for 5 min, and composite solutions are ultrasonicated at 60% for 5 min during material preparation. TEM then observes dispersed solutions to distinguish the morphology and dispersity of CNCs in composite solutions, as well as the dispersity of salts provided by CNCs.

Scanning Electron Microscopy

The salt:CNC composites were depicted via SEM (Zeiss, SUPRA 55VP; Oberkochen, Germany) at a working distance of 3.5 mm and an electron beam voltage of 1kV. The morphology of solid materials is analyzed using SEM. The differences in the physical form of composites v. control salts and composites of opposing CNC type are identified.

Porosity Measurement

The porosity of salt:CNC composites was measured using ImageJ (1.53t) analysis of SEM micrographs. First, the background was removed from the particles in SEM images, and the scale was set to the image width (i.e., 100 microns). Next, the threshold was adjusted to highlight the pores of the samples and applied to the image. Lastly, the 'analyze particles' function was used to calculate the porosity percentage based on the area of pores divided by the area of the particles. The Brunauer-Emmett-Teller (BET) method was not used for these measurements because it is limited to pores of a specific size deemed suitable. Additionally, the BET method would have required a significant amount of sample, which is beyond the current production abilities based on the estimated material surface area.

X-ray Diffraction Analysis

The crystallinity of salt:CNC was analyzed by powder XRD (Bruker D8, Advance; Billerica, MA). The XRD spectra were acquired from 5-100 2θ to capture all of the relevant peaks. Rietveld refinement was also performed on XRD scans of salt:CNC materials using the JADE processing software. The completed XRD scans were uploaded to the software to provide quantification of anhydrous and hydrated salt phases. XRD scans of the individual phases were provided in the software database. Once all individual phases were selected, the software uses the database scans to calculate the weight percentage of each phase within the study sample (i.e., salt:CNC composite or control).

High-Pressure Liquid Chromatography

HPLC data were acquired using a BioRad Aminex HPX-87H column (Hercules, CA) and an Agilent 1260 Infinity II system (Santa Clara, CA). Sample preparation for the compositional analysis of CNCs via HPLC was adopted from the National Renewable Energy Laboratory (NREL) published procedure [250]. 100mg of each CNC sample was weighed using a microbalance and transferred to an autoclave tube. 1 mL of 72% (w/w) sulfuric acid is added to the autoclave tube, and the mixture is incubated at 30˚C for 1 hour, with stirring every 5-10 minutes to dissolve the acid-soluble biomass. 27 mL of deionized water is then added to the mixture, and the tube is sealed for autoclaving at 121˚C/15 psi for 60 minutes for acid digestion. 1 mL of the autoclaved solution is filtered before injection into the HPLC column; the remainder is filtered through ashless filter paper to measure the Klason lignin content.

Fourier-Transform Infrared Spectroscopy

Fourier-transform infrared (FTIR) spectra of powder samples were acquired using a Thermo Scientific Nicolet iS5 system with a diamond iD7 attenuated total reflectance (ATR) detector (Madison, WI). The experiment was set up using OMNIC software, in which data were acquired using 64 background and 64 sample scans to produce an average from a larger sample set for higher-quality data [251].

Raman Spectroscopy

The Raman spectra of powder samples were recorded on glass slides using a Horiba Scientific LabRAM Evolution Confocal Raman microscope system (Kyoto, Japan), equipped with high-powered 532 nm and 785 nm lasers and 300, 600, and 1800 gr/mm grating. The spectrometer was

operated with the 300 gr/mm grating. The computer workstation was equipped with the LabSpec6 software. Samples were excited with 532 and 785 nm radiation from an Ar ion laser and analyzed with an acquisition time of 45 seconds and three accumulations for 532. Sample data was recorded over two ranges of wavenumbers (cm^{-1}): 50-1500 and 2500-3700 [252].

Thermogravimetric Analysis

Thermogravimetric analysis was conducted from 30°C to 1000°C at a rate of 10°C/minute under non-inert atmosphere (i.e., air) using a Discovery 5500 Thermogravimetric Analyzer (TA Instruments; New Castle, DE). Samples were held at 30°C for 5 minutes, then ramped to 110°C and held for 10 minutes to evaporate any moisture. The temperature was then ramped to 1000°C and held for 10 minutes to cause thermal decomposition.

Results

Thermophysical Properties

Dehydration enthalpy and water uptake values can be seen in *Figure 5.2,* in which orange bars denote pure salt enthalpy, blue bars denote 90:10 (salt:CNC) enthalpy, and green bars denote 80:20 (using control CNC). Additionally, *the 4b* and *6b* characters in the sample titles represent the batch numbers for material production, where *4b* = 4^{th} batch and *6b* = 6^{th} batch. The quantity of stored energy in 90:10 formulations is customarily greater than that of 80:20 formulations, as expected due to a greater salt mass fraction. Pure salts customarily have lower dehydration enthalpies than salt:CNC materials, but in some cases, they are higher than those of the 80:20 variety (e.g., $SrCl_2$). $MgSO_4$ shows unique results: both composites exhibit dehydration enthalpies significantly lower than those of the individual salts, due to lower water uptake and reduced salt

composition. The introduction of CNC at a minority mass fraction (i.e., 10 or 20%) into these salt hydrates improves their energy storage capabilities, except for $MgSO_4$.

All promising candidates have dehydration enthalpies within acceptable criteria, except for $CaCl_2$ pure and 90:10 (i.e., >300 J/g). High water uptake and low enthalpy suggest a deliquescence event of the salt occurring during hydration [253]. The trend is also observed in $SrCl_2$:$CaCl_2$:CNC samples, albeit to a lesser extent, indicating that $CaCl_2$ is most susceptible to deliquescence among the studied salts and therefore poses the most significant concern for stability. Notably, pure $SrCl_2$:$CaCl_2$ possesses a relatively low dehydration enthalpy while $SrCl_2$:$CaCl_2$ composites possess relatively higher values (279 v. 608 J/g). These findings validate the role of CNC in providing structure to salts and encouraging material homogeneity, thereby enhancing performance by resisting deliquescence. As in previous screenings, choice candidates continue to contain $SrCl_2$ [254].

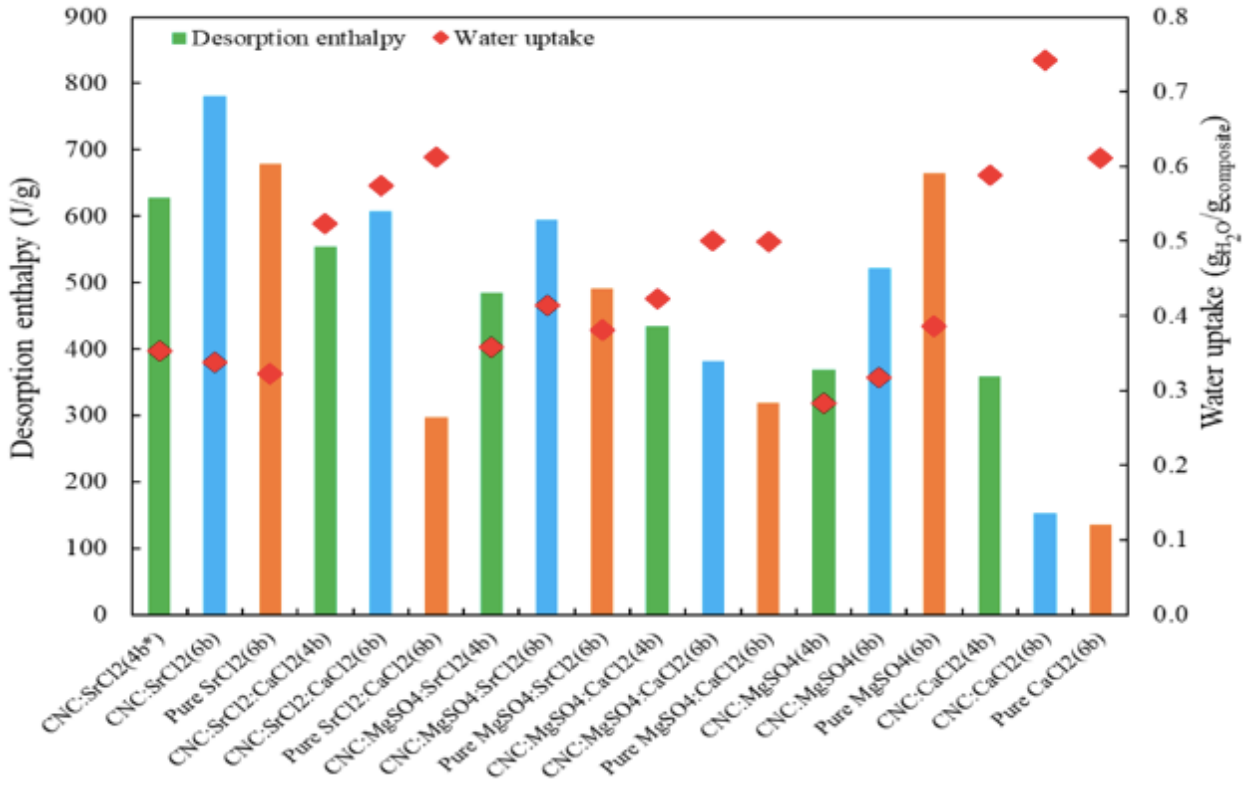

Figure 5.2 Water uptake and dehydration enthalpy values of 80:20 (green) and 90:10 (blue) composites using control CNC and salt controls (orange)

Additional formulations containing $SrCl_2$-based salt blends have been developed using a different salt combination ratio: $SrCl_2$:$CaCl_2$ – 90:10. The adjustment in $SrCl_2$ content provides another analytical perspective for generating the ideal composite for TES. Dehydration enthalpy and water uptake data for $SrCl_2$:$CaCl_2$ (90:10) samples and the control salt are presented in *Table 5.2*. As in $SrCl_2$:$CaCl_2$ (80:20) formulations, there is greater water uptake caused by the presence of $CaCl_2$. However, water uptake decreases significantly as CNC is added, thereby lowering the dehydration enthalpy because fewer reactants (i.e., water and salt) are present. Although the dehydration enthalpy is lower than that of the control salt, the energy storage is greater than that of any formulation in *Figure 5.2*. The presence of $CaCl_2$ also lowers overall material cost since

$SrCl_2$ is a more expensive salt hydrate. For these reasons, $SrCl_2$:$CaCl_2$ (90:10) formulations are pursued as final composites for upscale material development.

Table 5.2 Water uptake and dehydration enthalpy data of SrCl2:CaCl2 (90:10) formulations: salt:CNC – 90:10 (S9C19C1) and salt:CNC – 80:20 (S9C18C2)

Sample	Water Uptake	Dehydration Enthalpy (J/g)
S9C19C1	0.62	808
S9C18C2	0.59	748
Control Salt	0.78	849

Composites that possess increased energy storage relative to their respective salt control are of particular interest. However, composites that demonstrate high energy storage capabilities in general (i.e.,>600 J/g) are of primary importance to the study. The cost and abundance of $CaCl_2$ There are contributing factors as well in the continued consideration of using salt in the final product [255]. Although 60:40 (salt:CNC) formulations are not represented, it is anticipated that energy storage will be increasingly compromised as salt content is reduced [256]. Additionally, a CNC mass fraction of 40% contributes significantly to the cost of material manufacturing [257]. For these reasons, it is beneficial to place focus on 80:20 and 90:10 composite varieties. The dehydration enthalpy and water uptake values for the composites of most interest are emphasized in *Table 5.3*, along with their sample ID codes: $SrCl_2$:CNC (90:10) – S9C1; $SrCl_2$:$CaCl_2$:CNC (salt:salt – 80:20; salt:CNC – 90:10) – S8C29C1.

Table 5.3 Water uptake and dehydration enthalpy data of most promising salt:CNC formulations

Sample ID	Water Uptake (g_w/g_c)	Pure Salt (g_w/g_c)	Dehyd. Enthalpy (J/g)	Pure Salt (J/g)
S9C1	0.35	0.32	781	679
S8C29C1	0.57	0.61	608	297
S9C19C1	0.62	0.78	808	849

Thermogravimetric Analysis

TGA data for $SrCl_2$:CNC composites and controls were collected to provide a graphical representation of the mass steps associated with the $SrCl_2$ phase transition. The experiment was conducted from 30℃ to ~925℃ to also allow for an assessment of material thermal degradation under extreme conditions. The samples were held at 30℃ for 10 minutes, then again at 110℃, before increasing the temperature further to remove all moisture prior to initiating thermal decomposition. Although the TGA data of the control salt (i.e., $SrCl_2$) (*Fig. 5.3*) is similar to that of the 90:10 (salt:CNC) (*Fig. 5.4*) composite, there is a much more noticeable difference in the 80:20 data (*Fig. 5.5*). It is apparent that the 80:20 composite exhibits an additional hydrate transition not observed in the 90:10 and control data. It is known that $SrCl_2$ can exist in several hydrated phases: monohydrate, dihydrate, and hexahydrate. However, another hydrated phase of the salt has been recorded between the anhydrous and monohydrate phases: $SrCl_2 \cdot 0.5H_2O$, or hemihydrate. The hemihydrate is less common because its phase is less thermodynamically stable than those of the other hydrated phases [258]. However, the hydrophilicity of CNC enables $SrCl_2$ to transition from the monohydrate to the hemihydrate before reaching the anhydrous state. The main difference in dehydration behavior between the control salt and the 90:10 data is that the control salt experiences a smoother transition between phases. In contrast, the composite shows slightly more resistance to dehydration. This is evident by the more vertical slope in *Fig. 5.3* in comparison to *Fig. 5.4*. Additionally, there is greater mass loss in 90:10 data for the transition of hexahydrate to dihydrate than what is seen in control salt data. These findings also indicate that CNC addition provides hydrophilicity, thereby positively impacting hydration, and confers drying resistance. It should be noted that the mass loss from hexahydrate to dihydrate does not represent

the total sample mass during the transition, but represents a fraction of the sample that was in hexahydrate form.

The thermal decomposition of the control salt does not initiate until ~700°C, whereas the decomposition of the composites initiates at ~200°C. The lower temperature decomposition in composites is attributed to the pyrolysis of the CNC component. The greater mass loss during the decomposition event in 80:20 v. 90:10 composites provides further evidence for these claims, as there is 20 wt% CNC v. 10 wt% CNC. The mass loss observed in the control salt data at high temperature (i.e., ~700°C) is attributed to the release of chlorine gas from $SrCl_2$ as the salt approaches its melting point. As the salt melts, the strontium and chloride ions are allowed to move freely, which likely leads to the formation of chloride ions [259]. The phenomenon is expected to have occurred in the composite as well, but is overshadowed by the thermal decomposition and mass loss of CNC. The composites exhibit a significantly narrower thermal stability range than the control salt due to the CNC component.

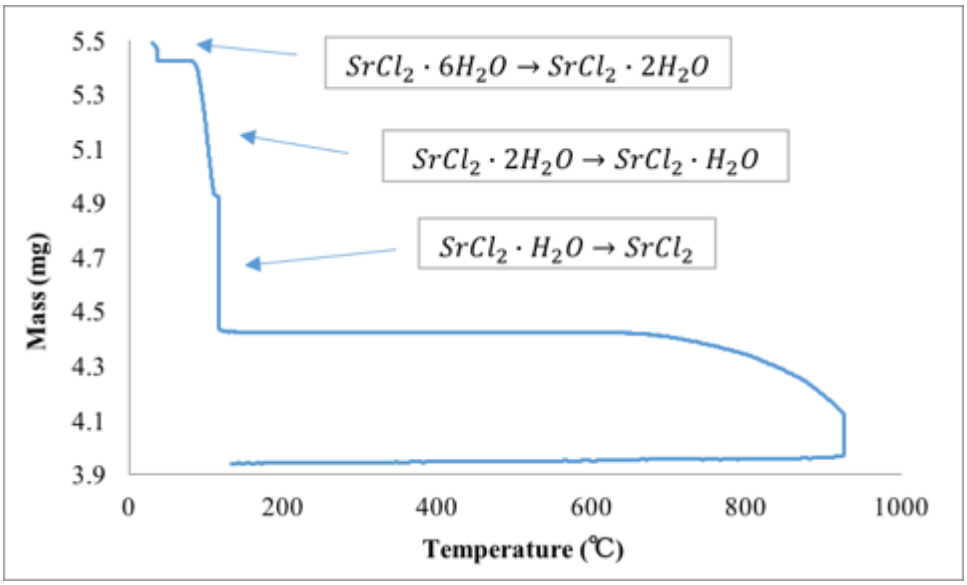

Figure 5.3 Thermogravimetric data for $SrCl_2$ control salt from 30°C to 1000°C

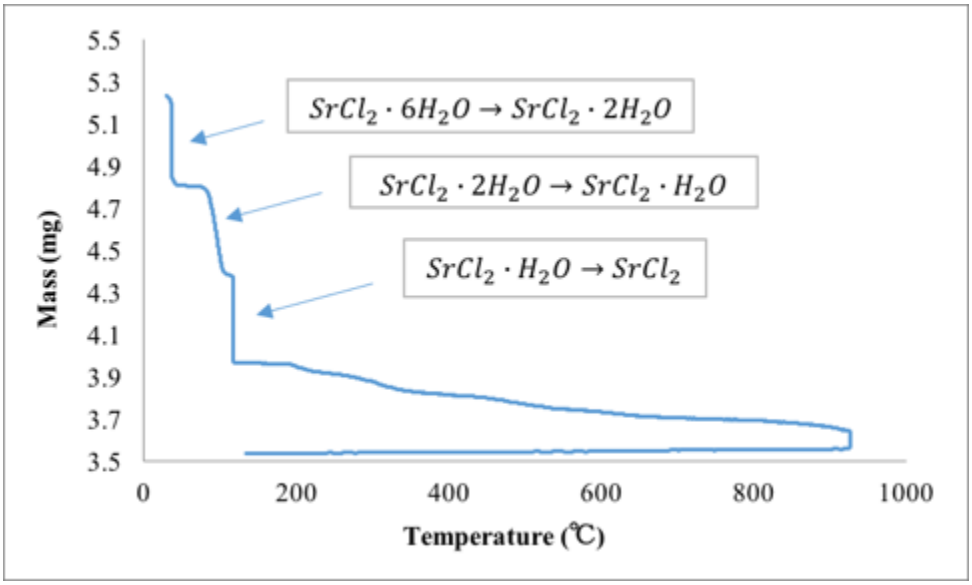

Figure 5.4 Thermogravimetric data for $SrCl_2$:CNC – 90:10 composite from 30°C to 1000°C

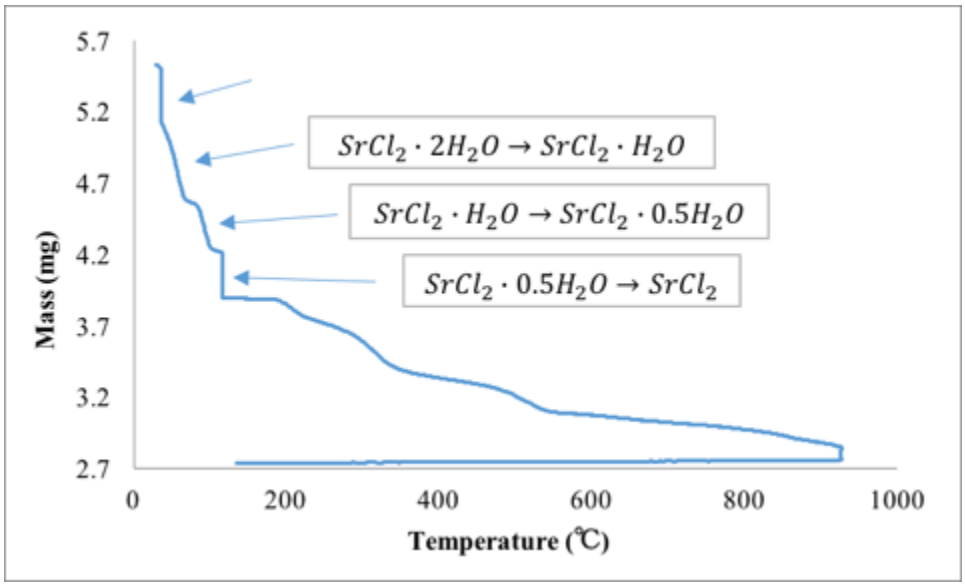

Figure 5.5 Thermogravimetric data for $SrCl_2$:CNC – 80:20 composite from 30°C to 1000°C

Salt:CNC Composites with SBPCNC

Table 5.4 shows the properties of CNC derived from pine and SBP that are relevant in salt:CNC formulation and performance: zeta-potential, crystallinity (%), cellulose content (i.e., purity), and crystal dimensions. These values define significant factors in CNC's ability to effectively nucleate salt crystals and provide a stable structural framework [260]. The commercial (i.e., control) CNC possesses improved zeta potential, crystallinity, and cellulose content, as well as a lower aspect ratio (L/W). These characteristics indicate that the commercial CNC is more suitable for assisting the performance of salt hydrate in TES. SBPCNC has a suitable zeta potential (>±30 mV) and a suitable aspect ratio, but has significantly lower % crystallinity and cellulose content. The shortcomings of SBPCNC relative to the control CNC are attributed to incomplete cellulose purification prior to acid hydrolysis. The reaction conditions of the pretreatment were accepted as a means to maintain the low environmental impact of the composite material life cycle

assessment (LCA) [261]. It should be noted that the reported cellulose content in the commercial CNC is lower than anticipated, as it should be >90% [262]. Therefore, the measured cellulose contents of SBPCNC and control CNC are likely higher than those reported here due to inefficiencies in the NREL-established method or the HPLC column.

Table 5.4 Significant properties affecting salt:CNC performance of control CNC v. SBPCNC

CNC	Zeta Potential	Crystallinity	Cellulose Content	Crystal Length and Width
Control	-64.63 mV	78.9% ± 6.5%	82.9%	242.13; 12.53 nm
SBPCNC	-48.15 mV	59.1% ± 6.5%	50.2%	314.67; 9.73 nm

Table 5.5 describes TES performance results of materials fabricated with commercial CNC v. those fabricated with SBPCNC. There is a significant decrease in the dehydration enthalpy when the commercial CNC is replaced with SBPCNC. These findings are attributed to the lower crystallinity and cellulose content of SBPCNC, as shown in *Table 5.4,* relative to those of the control CNC.

Table 5.5 Dehydration enthalpy and water uptake of $SrCl_2$ composites with SBPCNC realtive to composites with control CNC

Sample	Water Uptake (g/g)	Dehydration Enthalpy (J/g)	$SrCl_2$:CNC Control
SrCl2:SBPCNC 90:10	0.53	505.42	935.16
SrCl2:SBPCNC 80:20	0.52	472.86	763.16
SrCl2:SBPCNC 60:40	0.44	447.91	693.00

The $SrCl_2$ composites composed with phosphoric acid produced CNCs (P-CNC) were also tested, and their dehydration enthalpy at equilibrium conditions was measured (*Fig. 5.6*). All the $SrCl_2$ samples with SBPCNC have significantly lower desorption enthalpies than those without

SBPCNC. However, the desorption enthalpy values for P-CNC samples are comparable to those for $SrCl_2$:SBPCNC samples, which are produced with CNCs made via sulfuric acid hydrolysis of SBP rather than phosphoric acid. At equilibrium, all samples showed similar water uptake, whereas $SrCl_2$:SBPCNC samples absorbed more water, likely due to residual amorphous cellulose [263]. The primary difference between the samples is that the commercially obtained CNC results from a more refined, optimized process and has a higher degree of crystallinity and purity than CNC from SBP. However, the slight increase in dehydration enthalpy with lower water uptake exhibited by P-CNC samples v. SBPCNC samples indicates that different acid hydrolysis conditions can be used to tune the composite's material properties, and phosphoric acid-functionalized CNCs may be more suitable for TES applications in salt:CNC composites.

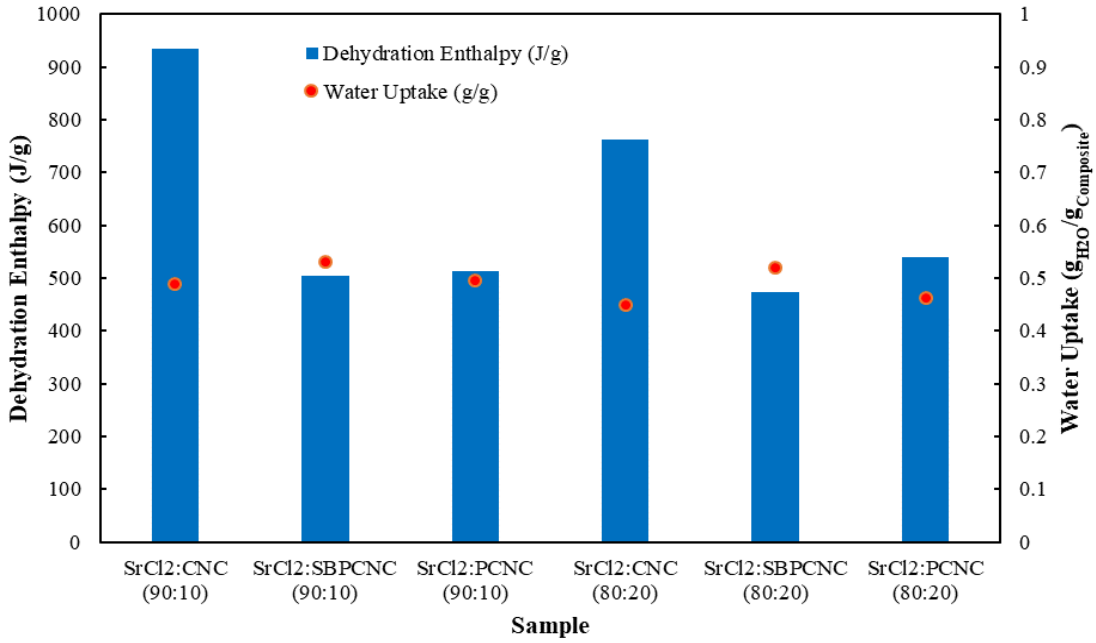

Figure 5.6 Equilibrium dehydration enthalpy and water uptake comparison between SrCl2: CNC, SrCl2: SBPCNC and SrCl2: P-CNC samples at 90:10 and 80:20 ratio

Composite Molecular Interactions

Raman Spectroscopy

Salt-CNC interactions were assessed using a variety of techniques, including Raman spectroscopy, FTIR spectroscopy, and XRD. Raman peak data have been compiled in a table (*Table 5.6*) for readability; the raw Raman data are provided in Appendix B. $SrCl_2$:CNC samples using commercial CNC were assessed relative to salt and CNC controls. Sample IDs are denoted based on sample code (S8C2 – $SrCl_2$:CNC, 80:20) and Raman excitation wavelength (532 versus 785 nm). The most notable peak locations have been emboldened to indicate peak responses that were recorded only in composite spectra. These peaks are highly significant because they suggest a unique interaction between salt and CNC [264]. The S9C1 peaks are slightly shifted to the left relative to the S8C2 peaks, suggesting weaker chemical bonds in the 90:10 composite [265]. The 785 nm excitation wavelength apparently failed to elicit a response in the $SrCl_2$ and CNC control samples in the higher-wavenumber spectrum. However, the $SrCl_2$:CNC samples did respond under these instrument conditions. Interestingly, composites display a similar strong peak response near ~3400 cm^{-1}, as seen in the $SrCl_2$ control, but a new peak arises near ~3350 cm^{-1}. This peak is present in the CNC control spectrum; however, the peak appears stronger and narrower in $SrCl_2$:CNC spectra. Although CNC displays a strong peak near ~2900 cm^{-1} with 532 nm excitation, no such peak is observed when scanning $SrCl_2$:CNC samples at the same wavelength. Only at 785 nm does a similar peak response occur in composite samples. Interestingly, the 785 nm wavelength does not provoke a detectable response from pure CNC in the 2500-3700 wavenumber range.

Raman findings reveal a unique lattice vibration in both $SrCl_2$:CNC composites and higher hydrated states of $SrCl_2$. The peaks at ~550 are characteristic peaks of librational modes involving the restricted motion of water molecules in the salt crystal lattice [266]. The ~3250 peaks in particular are attributed to symmetric O-H stretching vibrations of salt hydrate water molecules

[267]. Therefore, these peaks are observed in composite spectra due to CNC hydrophilicity and its impact on drying resistance. Moreover, the slight leftward shift of this peak in S9C1 indicates weaker hydrogen bonding within the composite network [265]. The peaks appearing at ~170 cm^{-1} are attributed to unique lattice vibrations of salt:CNC materials since 10-200 cm^{-1} is known as the Raman lattice mode region [268]. The modes represent vibrations of an entire crystal lattice rather than individual molecules. The peaks at ~700 cm^{-1} are attributed to the formation of $SrCO_3$ within the composite, which is produced from hydrated SrO via an oxidation reaction with air [269].

Table 5.6 Raman peak location data of SrCl2:CNC and control samples

Sample ID	Notable Peak Locations (cm^{-1})													
$SrCl_2$ 532	*65*	*-*	*140*	*-*	*265*	*-*	*471*	*-*	*-*	*-*	*-*	*-*	*3442*	*3520*
CNC 532	*-*	*88*	*-*	*-*	*-*	*380*	*436*	*-*	*-*	*1096*	*2900*	*-*	*3347*	*-*
$SrCl_2$ 785	*64*	*-*	*148*	*-*	*-*	*392*	*-*	*-*	*-*	*-*	*-*	*-*	*-*	*-*
CNC 785	*-*	*89*	*-*	*-*	*-*	*377*	*434*	*-*	*-*	*1094*	*-*	*-*	*-*	*-*
S8C2 532	*-*	*99*	*-*	***177***	*276*	*-*	*478*	***557***	***705***	*-*	*-*	***3252***	*3430*	*-*
S8C2 785	*62*	*93*	*147*	***168***	*271*	*379*	*477*	**-**	**-**	*1094*	*2900*	**-**	*3345*	*-*
S9C1 532	*-*	*87*	*147*	***173***	*272*	*-*	*468*	***554***	***708***	*-*	*-*	***3249***	*3427*	*-*
S9C1 785	*-*	*93*	*-*	***178***	*-*	*377*	*475*	***559***	**-**	*1094*	*2901*	**-**	*3442*	*-*

FTIR Spectroscopy

FTIR spectroscopy scans were performed using the same samples that were subjected to Raman spectroscopy to fully assess the excitation spectrum that induces a measurable vibrational response. It is known that FTIR results may complement Raman, as modes that are Raman-inactive are often FTIR-active [270]. An overlay of the FTIR spectra is shown in *Figure 5.7*. The prominent peaks appearing in the FTIR spectra include O-H stretching, which is seen between 3200-3600 cm^{-1}, and C-O stretching, which is seen between 1000-1100 cm^{-1} [271]. All samples are responsive to O-H stretching due to the hydroxyl groups of CNC and the water molecules that are within $SrCl_2$ hydrate(s). Other prominent peaks include a strong, sharp response near 1600 cm^{-1}, observed only

in samples containing $SrCl_2$. Moreover, the response decreases in intensity when CNC is introduced to $SrCl_2$, indicating that this peak is specifically due to the presence of $SrCl_2$, perhaps through unique FTIR interactions such as Sr-O or Sr-Cl bonding vibrations [272]. A similar waning response of composites is observed at 1050 cm^{-1}, relative to the CNC rather than the $SrCl_2$ control. The 1050 peak response decreases in composite samples and is absent in the $SrCl_2$ control spectra, indicating that the peak is due to CNC alone rather than to an interaction between a composite component and CNC. These peaks are attributed to the C-O stretching of CNC. Interestingly, $SrCl_2$:CNC composites display a unique peak at ~3000 cm^{-1} because of some specialized interaction, which is attributed to the O-H stretching of water molecules within the salt hydrate [273]. The combination of $SrCl_2$ and CNC in composites is also seen to cause a shift in the O-H peak of CNC, which is attributed to hydrogen bonding interactions between the water molecules of the salt hydrate and CNC. The O-H stretching of CNC control occurs at ~3350 cm^{-1}, whereas the O-H stretching of $SrCl_2$:CNC composites occurs at ~3200. These findings provide additional evidence supporting the assumption that there is a chemical, as well as a physical, interaction between salt hydrates and CNC. FTIR results indicate that salt-CNC chemical interactions are based on hydrogen bonding and other electrostatic forces between CNC and salt hydrate water molecules.

It has been proven that an increase in hydrogen bonding strength causes a shift in the O-H peak response from higher to lower wavenumber [274]. The peaks appearing at ~3200 and ~3350 cm^{-1} are attributed to the O-H stretching of hydroxyl groups in CNC, so the shift from ~3350 to ~3200 is likely caused by an increase in hydrogen bonding strength from water molecules within the salt hydrate lattice. However, the unique composite peak appearing at ~3000 cm^{-1} is attributed to a different interaction. The pattern of this peak is slightly visible in the control salt spectrum,

suggesting that it originates from bonding within the salt hydrate rather than CNC. It is known that alternative forms of water molecules have unique FTIR responses, such as adsorbed water molecules that form a hydration layer and water molecules that are directly part of a material lattice [275]. Since salt hydrates incorporate water molecules directly into their material structure, the peaks that appear at ~3000 cm^{-1} are attributed to the O-H vibrations of water molecules in the salt lattice. Moreover, CNC is proven to promote adsorption of water for salt hydrates (as evident by TGA data), so a greater O-H response of salt-bound water molecules is expected, given that there is more water in higher hydrated states (i.e., hexahydrate) in composites.

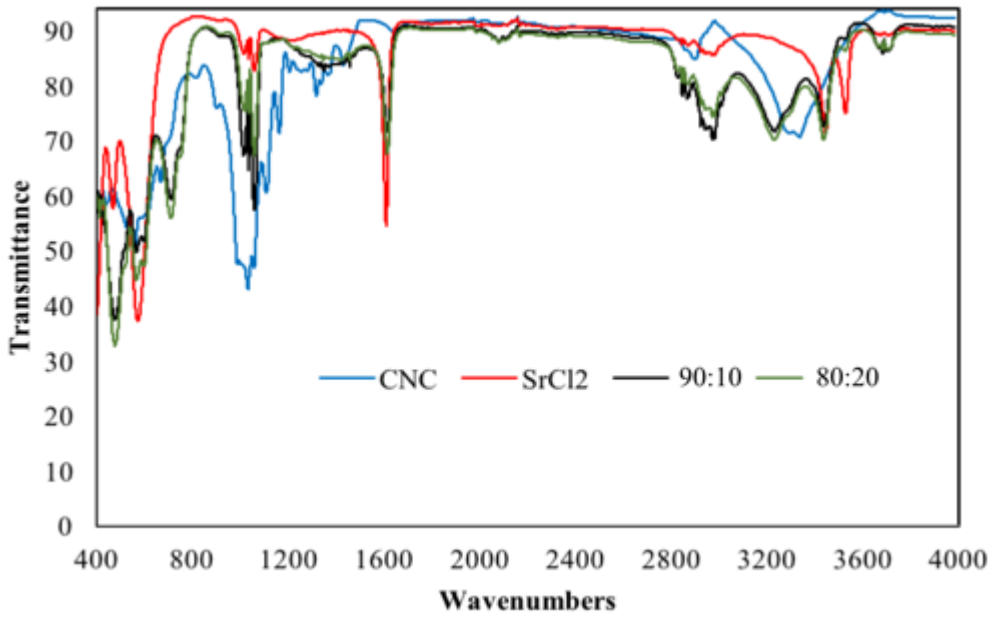

Figure 5.7 FTIR spectra overlay of: CNC (blue), $SrCl_2$ (red), $SrCl_2$:CNC – 90:10 (black), and $SrCl_2$:CNC – 80:20 (green) from 400 to 4000 cm^{-1}

X-ray Diffraction Analysis

$SrCl_2$ is known to form 4 different crystal structures: one in anhydrous form and three others in hydrated form: monohydrate, dihydrate, and hexahydrate. Therefore, four different crystal structures may be observed in a single XRD spectrum of $SrCl_2$ or $SrCl_2$:CNC. The crystal

structure of CNC is not visible due to the dominance of the salt crystal structure in the XRD response. In *Figure 5.8*, it is apparent that there are prominent peaks of $SrCl_2$ (control), which appear in $SrCl_2$:CNC composites using SBPCNC only. In contrast, there are other prominent peaks of the $SrCl_2$:CNC composites that do not appear in the control spectrum. The peaks that do not appear in the control spectrum, in particular, are indicative of a greater variety of $SrCl_2$-hydrated phases in the composite but not in the control salt. These peaks are more dominant in composites processed with control CNC than with SBPCNC because control CNC provides greater uniformity. Therefore, the current crystalline phase of the salt may be less variable. The peaks in the control salt appear only in composites using SBPCNC and are significant because they are absent in the spectra of composites using control CNC. These discrepancies are attributed to a greater drying resistance of composites comprised with control CNC v. SBPCNC (at 70˚C). The presence of these additional peaks in composites using SBPCNC v. control CNC provides further evidence of poorer salt nucleation and dispersion, which results in a lack of uniformity. SBPCNC appears to cause the formation of 'pockets' of various crystalline phases throughout the material, more so than control CNC. These interpretations are supported by reduced purity, lower zeta potential magnitude, and lower crystallinity of SBPCNC relative to control CNC, as well as a larger aspect ratio.

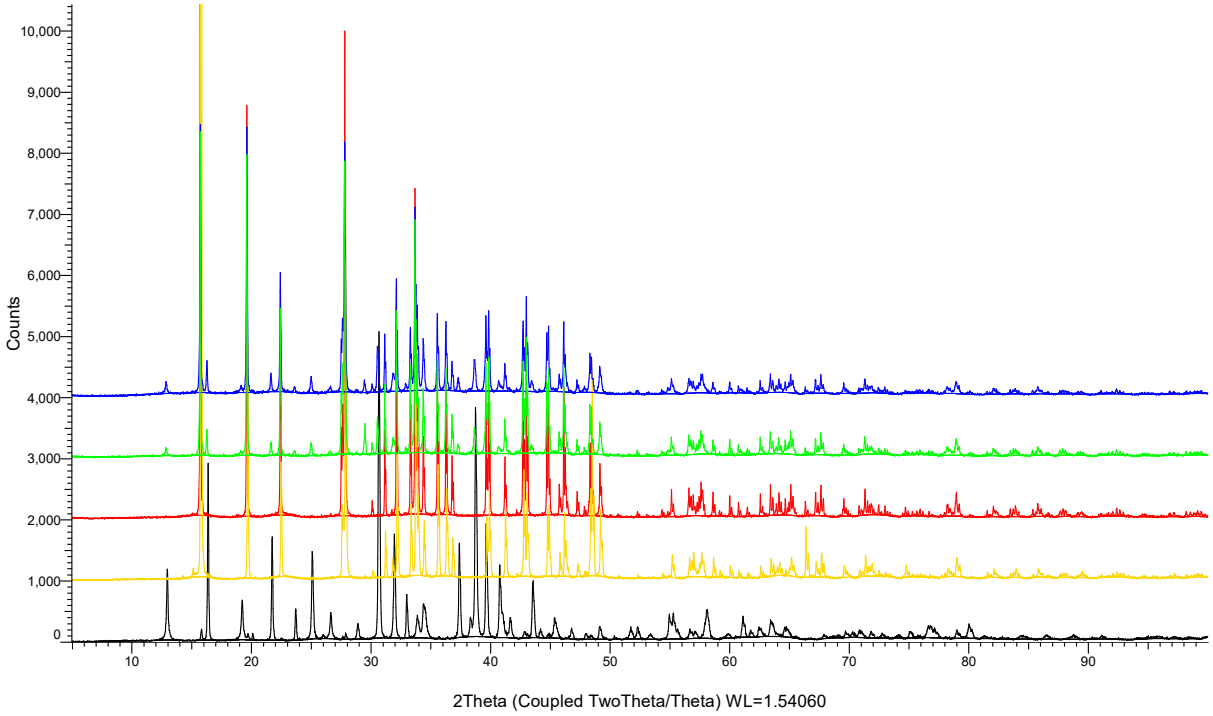

Figure 5.8 XRD scans of 80:20 (red) and 90:10 (yellow) composites using control CNC (red; yellow) and SBPCNC (blue; green) with salt controls (black) for $SrCl_2$ and from 5˚ to 100˚ 2θ

XRD scans of $SrCl_2$ composite and control samples were subjected to Rietveld refinement analysis as a means to quantify the hydrated (and anhydrous) phases. The results are presented in *Tables 5.7* and *5.8*, and the spectra-fitting (via JADE) used in the Rietveld refinement process is presented in Appendix B. The dried samples were dehydrated at 110˚C for 1 hour to accurately represent the dehydration step that occurs during energy density measurements and material cycling. The hydrated samples were prepared by enclosing the materials in a desiccation chamber containing a saturated NaCl solution; an image of the setup is provided in Appendix B for visualization. A humidity sensor was also placed inside the chamber alongside the samples to ensure the interior atmosphere was suitable for the hydration event (Extech, 445703). The humidity

inside the chamber was recorded at 60% RH, and the samples were hydrated for 24 hours prior to Rietveld refinement analysis.

Table 5.7 Rietveld refinement phase quantification for dehydrated $SrCl_2$ composites and control

Sample	Salt:CNC	Anhydrous (%)	Monohydrate (%)	Dihydrate (%)	Hexahydrate (%)
$SrCl_2$	-	0.0 ± 0.0	98.3 ± 0.8	1.1 ± 0.4	0.6 ± 0.1
S9C1	90:10	8.7 ± 0.2	89.7 ± 0.9	1.6 ± 0.5	0.0 ± 0.0
S8C2	80:20	0.4 ± 0.1	98.8 ± 0.8	0.0 ± 0.0	0.8 ± 0.2

Table 5.8 Rietveld refinement phase quantification for hydrated $SrCl_2$ composites and control

Sample	Salt:CNC	Anhydrous (%)	Monohydrate (%)	Dihydrate (%)	Hexahydrate (%)
$SrCl_2$	-	0.0 ± 0.0	0.3 ± 0.8	0.6 ± 0.7	99.2 ± 8.8
S9C1	90:10	0.0 ± 0.0	0.0 ± 0.0	0.0 ± 0.0	100 ± 3.6
S8C2	80:20	0.4 ± 0.2	0.3 ± 0.6	0.1 ± 0.0	99.3 ±4.3

The 90:10 composite achieves the highest efficiency in converting the salt ($SrCl_2$) between the hydrated and dehydrated phases. The 90:10 composite achieves an anhydrous composition of 8.7% whereas the control salt and 80:20 composite are nearly 100% monohydrate. The control salt and the 80:20 composite also retain some of the hexahydrate phase after the dehydration event, indicating resistance to material charging. Furthermore, the hydration event results in complete conversion of $SrCl_2$ to its maximum hydrated phase in the 90:10 composite (100 ± 3.6%), whereas the control salt and the 80:20 composite show slightly incomplete conversion (i.e., <100% hexahydrate). These findings provide additional evidence of the superior performance of 90:10 composites in TES.

Composite Morphology

Scanning Electron Microscopy

Figures 5.9a-b display incredibly geometric crystals of a composite material (containing control CNC), whereas *Figures 5.9c-d* display larger masses of a less-organized crystal structure. *Figure 5.9e* shows the control salt ($SrCl_2$), which is more similar in morphology to composites with control CNC than composites with SBPCNC, based on initial observations. These findings help justify the significant loss in dehydration enthalpy exhibited by composites with SBPCNC. The less-ordered crystal structure of SBPCNC composites indicates that less energy can be gained from the change in material entropy during water uptake [276]. Furthermore, it is apparent through *Figure 5.9* that $SrCl_2$:CNC composites produced using control CNC are more porous and uniform than composites produced using SBPCNC. These observations support XRD interpretations. The differences in morphology are attributed to the higher purity and dimensional consistency of the control CNC relative to the SBPCNC. The $SrCl_2$ control appears to be more porous and less agglomerated, as observed by SEM, which helps explain the significant decrease in TES performance between SBPCNC composites and other samples with $SrCl_2$. Although water uptake is similar, lower porosity would result in less water diffusion into the materials. Therefore, there is less conversion of salt to its fully hydrated form, and the material's energy storage performance suffers. Additionally, the larger agglomerations of SBPCNC-containing composites indicate a smaller particle surface area, meaning a greater mass of composite material is unexposed to humidity and relies on water diffusion to convert to the hydrated form.

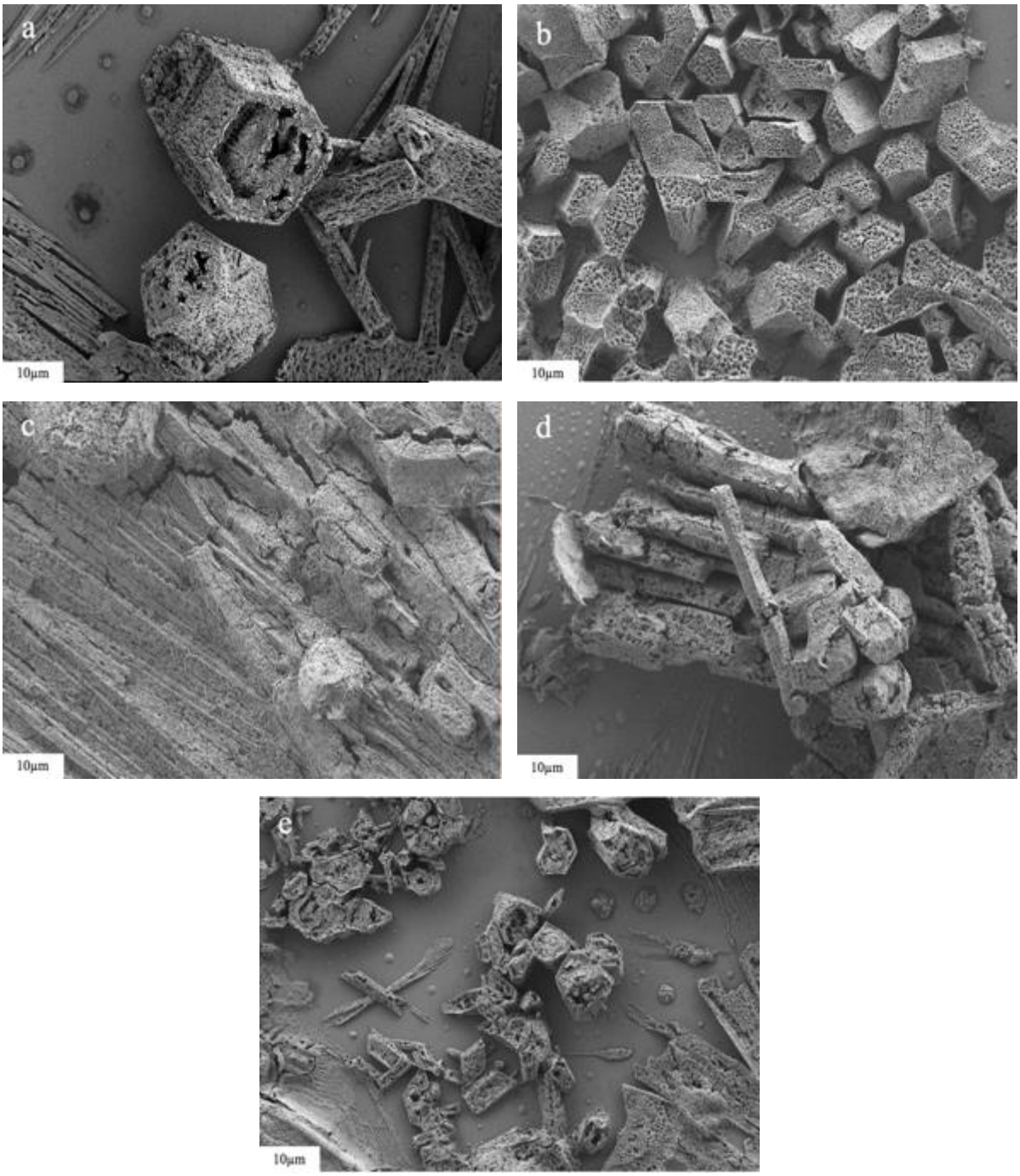

Figure 5.9 SEM images acquired at 2160x magnifcation of: (a) SrCl2:CNC – 90:10; (b) 80:20; (c) 90:10-SBP; (d) 80:20-SBP; (e) $SrCl_2$

Porosity Measurement

The above SEM micrographs were analyzed for porosity using ImageJ to determine the percent area of material topography corresponding to pores. These measurements were made to support morphology interpretations based on the SEM micrographs of the composite and control samples. The results are summarized in *Table 5.9*. It is apparent that control CNC increases porosity in $SrCl_2$:CNC composites, whereas SBPCNC decreases porosity relative to the control salt ($SrCl_2$). These differences are attributed to the increased aspect ratio and higher amorphous content in SBPCNC relative to control CNC.

Table 5.9 Porosity measurements of $SrCl_2$:CNC composites and control (acquired via ImageJ)

Sample	$SrCl_2$:SBPCNC	$SrCl_2$:SBPCNC	$SrCl_2$:CNC	$SrCl_2$:CNC	$SrCl_2$
Salt:CNC	90:10	80:20	90:10	80:20	-
Porosity (%)	10.889	11.815	13.317	24.852	12.537

Transmission Electron Microscopy

TEM images of salt:CNC composites (80:20) are displayed in *Figure 5.10a-c*, in which $SrCl_2$, $CaCl_2$, and $SrCl_2$:$CaCl_2$ (80:20) are represented. Evidence of CNC nucleation of salt is apparent among all samples. The shading of images depends on electron density: lighter regions have lower electron density, which lessens the repulsion of the microscope beam. As such, the black and darker grey shading is characteristic of salt, while the lighter grey shading is characteristic of CNC, and is apparent by its needle-like particle shape. Lighter grey shading may also be characteristic of marginal sample coverage and is apparent by the voided space in the imaged medium. There are several salt body centers depicted by the black shading in the images, but CNC appears well dispersed throughout and seems to inhibit salt aggregation in some regions.

Additionally, salt body centers have submicron diameters, which are beneficial for material performance [277]. The observations of $CaCl_2$:CNC and $SrCl_2$:CNC are similar in that both possess a greater number of salt body centers than $SrCl_2$:$CaCl_2$:CNC, but no significant salt aggregation. $SrCl_2$:CNC differs by possessing larger salt body centers, which suggests that the material is more prone to salt aggregation. $CaCl_2$:CNC differs by possessing seemingly more salt body centers but of lesser size, and a slight grouping of CNC particles. These observations suggest $CaCl_2$:CNC is less prone to salt aggregation, which is in alignment with the solubility of salts. However, $CaCl_2$:CNC appears to be more prone to CNC aggregation. These single-salt composites exhibit flocculation tendencies for either salt or CNC, but the complications diminish when used as a salt blend in $SrCl_2$:$CaCl_2$:CNC. $SrCl_2$ and $CaCl_2$ aid each other in blending properly with CNC to produce a more homogeneous composite. However, it is apparent that CNC successfully disperses the solvated salt, as evidenced by the slightly darker shading near the center of each CNC body. From these results, it is supported that $SrCl_2$:$CaCl_2$:CNC is most supportive of material stability by exhibiting the most uniformity of salt:CNC mixing. $SrCl_2$:CNC and $CaCl_2$:CNC possess a high uniformity as well. However, there are some agglomerations in salt-dense regions of $SrCl_2$:CNC and CNC-dense regions of $CaCl_2$:CNC, which may cause complications in long-term material cycling stability (i.e. 500+ cycles).

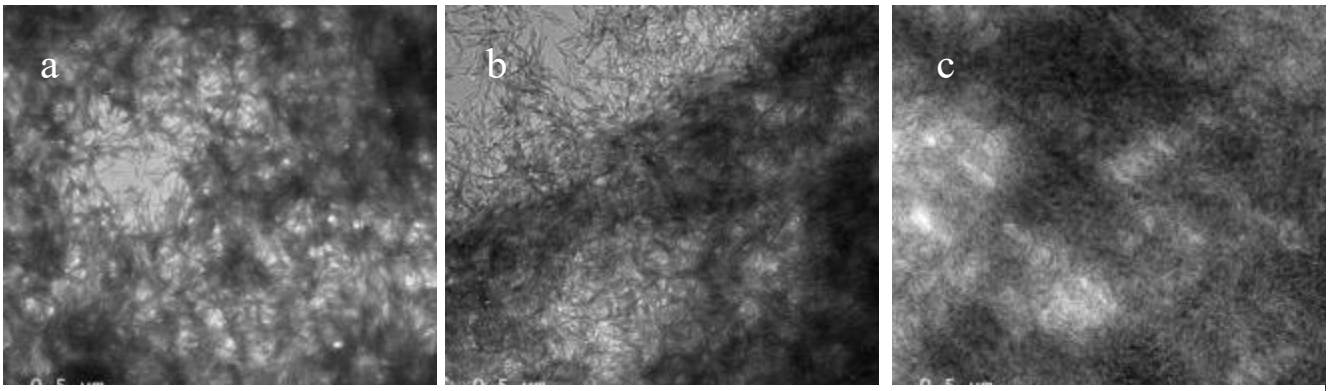

Figure 5.10 TEM images of salt:CNC (80:20) formulations aquired at 16000x magnification for: (a) $SrCl_2$, (b) $CaCl_2$, and (c) $SrCl_2$:$CaCl_2$ – 80:20

Discussion

Salt:CNC TES Performance

The addition of CNC to most salt hydrates has been shown to enhance TES while aiding hydration (i.e., energy release) in $SrCl_2$, CaCl2, $SrCl_2$:$CaCl_2$, $MgSO_4$:$SrCl_2$, and $MgSO_4$:$CaCl_2$. $MgSO_4$ is unique in that the energy density decreases significantly as CNC is added, attributed to an over-hydration event leading to deliquescence issues or other forms of structural disassembly [278]. In other salt varieties, CNC impregnation enhances the TES abilities of 90:10 formulations but not of 80:20 formulations, except for $MgSO_4$:$SrCl_2$ and $SrCl_2$. However, these exclusions are mainly due to the high energy density of the control salts. It should be noted that ion swapping occurs in salt blends, which can result in the formation of poorly soluble, or in some cases, insoluble salts. The phenomenon was observed during the development of $MgSO_4$:$SrCl_2$ composites, which form a nearly insoluble salt, $SrSO_4$, as sulfate and chloride ions are exchanged between the metal ions. The phenomenon was also observed in the development of $MgSO_4$:$CaCl_2$ composites, although $CaSO_4$ is slightly more soluble than $SrSO_4$. Overall, the formation of these insoluble chemical species reduces TES capacity by trapping and isolating valuable, energy-dense salts in a different form. Therefore, it is learned that the combination of chloride salts with sulfate (or hydroxide) salts should be avoided to prevent any loss in the theoretical TES capacity.

The benefits to the TES performance of salt hydrates in composites are a result of the assistance that CNC provides in the conversion of salts to their hydrated forms. SEM images reveal improved uniformity in morphology, as evidenced by salt:CNC materials using control CNC, as well as a more porous structure. These observations were confirmed by the measurements of material porosity presented in *Table 5.9*. The composites developed using control CNC are significantly more porous than the salt control (i.e., $SrCl_2$). These findings validate the enhanced

TES abilities of salt:CNC composites, as their morphological features aid water adsorption and diffusion [279]. The greater porosity, in particular, would allow for adsorbed water to diffuse throughout the material with less resistance so that non-hydrated (or sub-hydrated) salts may be reached [280]. The theoretical energy density of salts has not been achieved in these studies, which may be due to deficient hydration conditions and salt concealment [281]. However, it is important to avoid salt deliquescence, so achieving complete hydration of the materials may be precarious, as water must continue to be adsorbed from the surface for the concealed salt to be hydrated [282]. The lack of porosity observed in the SEM images of SBPCNC composites further demonstrates how these morphological features affect TES performance. Formulations containing SBPCNC achieved dehydration enthalpies nearly half those of formulations with control CNC (*Table 5.5*), which could be a direct consequence of salt concealment. Since there were similar water-uptake values between SBPCNC and control CNC composites (*Fig. 5.6*), SBPCNC composites are likely more prone to deliquescence due to poorer water diffusion [283]. However, the composites need to be cycled alongside control CNC composites (with $SrCl_2$) before reaching such conclusions.

Since the 90:10 formulations were shown to enhance TES performance there has been less focus on 60:40 formulations due to their lower energy density and higher material cost [284]. The same can be said for 80:20 formulations. However, these composites may be helpful if 90:10 formulations exhibit a loss in energy storage capacity that is insufficiently significant relative to research goals (ie., 5000 cycles). In terms of observable changes in morphology during cycling, the control salt starts as a smooth, lightly packed powder bed from cycles 1–15. However, by 30–40 cycles, the repetitive swelling of each hydration step causes the material surface to rupture and bulge into a loose, fibrous crust [285]. As cycling continues, these agglomerates grow and become more fragile, gradually consolidating into larger, irregular chunks. These observations of a

progression from an expanded, highly ordered state to a lumpy, unorganized state suggest that there is a cycle-induced mechanism for structural breakdown and reformation [286]. $SrCl_2$:CNC formulations exhibit a slightly smoother topography and a greater surface area, owing to a higher volume of small surface features across the composite [287]. In 80:20 $SrCl_2$:CNC, the surface area of crystals appears to be increased further by the nucleation assistance of CNC. Small clumps of material form composites, which then transition to more jagged surface features and later to a more ordered structure. The hydration events may facilitate salt migration and reordering, enabling the consolidation of smaller, jagged salt crystal growth [288]. Needle-shaped crystal growth is also observed across large crystal surfaces, a characteristic of $SrCl_2$ when crystallized slowly [289].

The dispersion of CNC in composite solutions as a function of the source material is dependent on the CNC crystallinity and surface charge [290]. Having a higher surface charge reduces particle agglomeration by increasing repulsive forces, while higher crystallinity reduces agglomeration by preventing entanglements caused by residual amorphous components. HPLC data reveal that the control CNC has a much higher cellulose content than SBPCNC and therefore has higher purity. The lack of purity and crystallinity in SBPCNC is another factor contributing to the poor performance. However, SBPCNC still provides a structural framework and may allow extended cycling of salts if deliquescence does not occur due to poor water diffusion. The framework of both SBPCNC and control CNC composites is observed firsthand through increased grinding resistance relative to pure salts. All formulations, including controls, were processed identically, so the difference in physical force required to powder the materials via mortar and pestle was noticed and is significant. The observation was particularly pronounced in SBPCNC composites, most likely due to the amorphous components exerting a binding effect within the material through entanglements or other intermolecular interactions [291].

Salt:CNC Composite Interactions

Chemical interactions in the composites were determined using Raman and FTIR spectroscopy. The techniques are known to detect various material bonding and can therefore detect potential electrostatic interactions in composites [292]. Raman spectroscopy reveals unique bonding and/or lattice vibrations arising from the salt:CNC combination (*Table 5.6*). Since CNCs are proven to nucleate salt crystals via TEM imaging (*Fig. 5.10*), CNCs may likely cause new lattice vibrations to arise in composites, either from the defects at component interfaces or the presence of hydrated crystal structure(s) that are not present in the salt control (i.e., $SrCl_2$). As mentioned above, SrCl2 exhibits four distinct crystal structures between the anhydrous and hydrated forms, and additional crystalline peaks appear in the XRD data (*Fig. 5.8*) due to other hydrated phases of the salt that are absent in the control spectrum. Therefore, the additional composite peaks observed in the Raman data (*Table 5.6*) may result from lattice vibrations of these hydrated forms [293]. It is further supported that these additional peaks are a result of extra hydrated states by the peak appearing in S8C2 and S9C1 (532) samples' spectra at ~3250 cm^{-1} because the O-H vibrations of water are typically observed from 3250-3410 cm^{-1} [294]. Since the ~3250 Raman response is unique to composite samples and materials are shown by XRD to exhibit greater water retention (*Fig. 5.9*), other peaks unique to composites are also likely a result of greater water retention. However, the position of the water peak may shift from that of the composites if the control salt is hydrated to the same extent as the composites [295]. The O-H stretching of CNC was found to be shifted in composites due to hydrogen bonding interactions with salt hydrate water molecules via FTIR tests (*Fig. 5.7*), so these shifts can occur in Raman data as well [296].

The broad peaks shown in FTIR data between 3200 and 3600 cm^{-1} were assigned as the O-H stretching of CNC. There is a significant range for these peaks due to their broad nature and electrostatic interactions with other polarizing groups, which can shift the peak [297]. The phenomenon is apparent in *Fig. 5.7, as shown* by the comparison between the composites and the controls ($SrCl_2$ and CNC). Salt:CNC materials display a shift in the O-H stretching of CNC because of hydrogen bonding interactions between salt hydrate water molecules and CNC hydroxyl groups (~3350 v. ~3200 cm^{-1}, respectively). Additionally, the composites display a unique peak at ~3000 cm^{-1} due to the O-H vibrations of water molecules in the salt hydrate [298]. The peak is most likely a direct result of the greater abundance of higher-hydrated states in the composite relative to the control salt, especially given that the peak is faintly visible in the control salt spectrum [299]. Since CNC naturally possesses a surface charge and a hydrophilic nature from acid hydrolysis procedures, salt hydrates are attracted to the CNC surface, and CNC assists in salt hydrate water adsorption/retention [300].

Zeta potential experiments validate these interpretations. Materials characterized by a zeta potential of greater magnitude exhibit less agglomeration and improved dispersion via electrostatic repulsion [301]. However, surface charge may be shielded by the addition of an aqueous salt, which forms an electrical double layer around charged particles [302]. The double layer is comprised of one layer of the cation and one layer of the anion that make up the salt. NaCl is used at very low concentration (i.e. 5-50 mmol) in zeta potential experiments to form the electrical double-layer so that particles may be enveloped by salt and better separated for measurement [303]. However, a higher salt concentration will shield the surface charge, thereby counteracting the purpose of salt in zeta potential samples [304]. These interactions are also highly relevant to salt:CNC composites, since the materials are formed from aqueous mixtures of CNC and salt.

Therefore, additional salt-CNC electrostatic interactions include the formation of an electrical double layer that encloses CNC particles. These interactions are strongly favorable for impregnating CNC to nucleate salt crystals, thereby forming the composite structural framework (*Fig. 5.10*). Although CNC has been added at a specific mass fraction, it has been shown to nucleate salt crystal growth, suggesting that CNC density decreases toward the composite surface [305]. The density gradient is significant because it indicates that salt density increases toward the composite surface, which is favorable for the material's response to humidity. Therefore, individual composite components are highly compatible and have significant potential to develop a reliable product for low- to mid-temperature TES.

SBPCNC v. Control CNC

The primary concern of CNC substitution between control CNC and SBPCNC is the adverse effects on dehydration enthalpy and material cycling stability. SBPCNC has a larger aspect ratio than the control CNC, thereby reducing its nucleation and dispersant abilities, as observed with salts [306]. SBPCNC also possesses a lower crystallinity than control CNC, so there is less resistance to degradation and an increased susceptibility to form imperfections by entanglement of remaining amorphous components [307]. These entanglements of CNC may then provoke salt aggregation and deliquescence events by providing a weaker structural framework and fewer dispersive effects. Additionally, the poorly ordered state of SBPCNC composites in SEM images indicates that less energy can be gained from the change in entropy of the material (salt) upon hydration [308]. Therefore, the CNC substitution from the control to SBPCNC lowers material performance prospects. These findings are also apparent in XRD peaks composites using SBPCNC that are absent in spectra of composites using control CNC (*Fig. 5.8*). The presence of these

additional peaks in composites using SBPCNC v. control CNC provides further evidence of poorer salt nucleation and dispersion, which results in a lack of uniformity. SBPCNC causes 'pockets' of various crystalline phases to form throughout the material, more so than control CNC. The reduced purity, zeta potential magnitude, and crystallinity of SBPCNC relative to control CNC are primary factors, along with the larger aspect ratio.

If CNC is to be used from SBP, it is recommended that stronger pretreatment conditions be used to generate CNC from SBP. The primary reason for SBPCNC's inferior performance compared to the control CNC is its lower crystallinity and purity (i.e., cellulose content). If stronger pretreatment conditions are used, the cellulose fraction of SBP may be purified enough to produce a CNC product comparable to that obtained via standardized sulfuric acid hydrolysis [309]. The pretreatment conditions for SBPCNC in this study were selected based on the LCA of the final product. Since CNC is the most expensive component of the composite (per unit mass), maintaining pretreatment conditions of minimal economic impact (i.e., less intense conditions) was desirable [310]. However, it may be worthwhile to develop an improved procedure for producing SBPCNC, as it is a waste material with significant potential for reuse [311]. Based on current insights, the quality of SBPCNC may be improved by increasing the chemical concentration during pretreatment, in addition to repeating the bleaching treatments (e.g., 3x) [312]. It is the bleaching treatments that must be repeated to purify the cellulose in biomass that require an alternative chemical means other than hydrolysis (i.e., oxidation) [313]. If SBP is purified to the extent that the white pine wood pulp is before hydrolysis to produce control CNC, then it is likely that SBPCNC may be produced of a more competitive quality. These findings also strongly suggest that CNF may not be appropriate for thermochemical TES applications involving salt hydrates [314].

Conclusion

$SrCl_2$:CNC and $SrCl_2$:$CaCl_2$:CNC ($SrCl_2$:$CaCl_2$ – 90:10) are proven to be the most promising of the TES materials that were developed based on energy density and uniformity. In particular, the 90:10 – salt:CNC varieties. The interpretations here suggest that $SrCl_2$:CNC is an excellent candidate for demonstrating cycling stability of 500 cycles. The combination of a lack of porosity and larger particle agglomerations is attributed as the primary cause of poorer SBPCNC composite performance. FTIR results indicate that salt:CNC interaction, in a chemical sense, is based on the hydrogen bonding between CNC and water molecules of the salt hydrate. The interpretations are supported by Raman data, which indicates unique salt:CNC lattice vibrations and/or salt hydrate effects on CNC vibrations as in FTIR. The discrepancies in the XRD pattern observed for CNC are directly responsible for greater water retention in the composites. The hydrophilicity of CNC increases drying resistance by binding to free water and the water molecules in salt hydrates. The composite materials form due to mechanical and electrostatic interactions, with strong chemical affinity between them, as observed by TEM. $SrCl_2$:CNC composites produced using control CNC are more porous and uniform than composites produced using SBPCNC. SEM observations are in support of XRD interpretations. Additionally, SBPCNC-containing composites form larger agglomerations, indicating that the materials rely on water diffusion for concealed salt to be converted to the hydrated form. The poor performance of SBPCNC composites is due to reduced purity, zeta potential magnitude, and crystallinity relative to the control CNC, as well as a larger aspect ratio. SBPCNC composites may be competitive if the chemical treatments used to produce SBPCNC are intensified to yield a more comparable product.

REFERENCES CITED

[1] U.S. Environmental Protection Agency (2023) "Global Greenhouse Gas Emissions Data" Available: https://www.epa.gov/ghgemissions/global-greenhouse-gas-emissions-data

[2] U.S. Energy Information Administration (2023) "Renewable and Alternative Fuels" Available: https://www.eia.gov/renewable/

[3] Zhao, Q.; Lin, J.; Huang, H.; Wu, Q.; Shen, Y.; Xiao, Y. (2021) "Optimization of thermochemical energy storage systems based on hydrated salts: A review" *Energy and Buildings* 244 111035

[4] Chavam, S.; Rudrapati, R.; Manickam, S. (2021) "A comprehensive review on current advances of thermal energy storage and its applications" *Alexandria Eng. J.* 61 pp. 5455-5463

[5] Ho, C.K.; Ambrosini, A. (2020) "Thermal Energy Storage Technologies" *Sandia National Laboratories* Ch. 12

[6] Seyitini, L.; Belgasim, B.; Enweremadu, C.C. (2023) "Solid state sensible heat storage technology for industrial applications – A review" *J. of Energy Storage* 62 106919

[7] Salgado-Pizarro, R.; Calderon, A.; Svobodova-Sedlackova A.; Fernandez, A.I.; Barreneche, C. (2022) "The relevance of thermochemical energy storage in the last two decades: The analysis of research evolution" *J. of Energy Storage* 51 104377

[8] Lefebvre, D.; Handan Tezel, F. (2017) "A review of energy storage technologies with a focus on adsorption thermal energy storage processes for heating applications" *Renew. Sustain. Energy Rev.* 67 pp. 116-125

[9] Hua, W.; Yan, H.; Zhang, X.; Xu, X.; Zhang, L.; Shi, Y. (2022) "Review of salt hydrates-based thermochemical adsorption thermal storage technologies" *J. of Energy Storage* 56 106158

[10] Kiyabu, S.; Girard, P.; Siegel, D.J. (2022) "Discovery of Salt Hydrates for Thermal Energy Storage" *J. Am. Chem. Soc.* 144 pp. 21617-21627

[11] Yang, H.; Wang, C.; Tong, L.; Yin, S.; Wang, L.; Ding, Y. (2023) "Salt Hydrate Adsorption Material-Based Thermochemical Energy Storage for Space Heating Application: A Review" *Energies* 16 2875

[12] Ferchaud, C. (2016) "Experimental study of salt hydrates for thermochemical seasonal heat storage" [PhD Thesis] *Technische Universiteit Eindhoven*

[13] Hayatina, I.; Auckaili, A.; Farid, M. (2023) "Review on Salt Hydrate Thermochemical Heat Transformer" *Energies* 16 4668

[14] N'Tsoukpoe, K.E.; Schmidt, T.; Rammelberg, H.U.; Watts. B.A.; Ruck, W.K.L. (2014) "A systematic multi-step screening of numerous salt hydrates for low temperature thermochemical energy storage" *Applied Energy* 124 pp. 1-16

[15] Zbair, M.; Bennici, S. (2021) "Survey Summary on Salts Hydrates and Composites Used in Thermochemical Sorption Heat Storage: A Review" *Energies* 14 3105

[16] Li, W.; Klemes, J.J.; Wang, Q.; Zeng, M. (2022) "Salt hydrate-based gas-solid thermochemical energy storage: Current progress, challenges, and perspectives" *Renew. and Sustain. Energy Reviews* 154 111846

[17] Sögütoglu, L.; Birkelbach, F.; Werner, A.; Fischer, H.; Huinink, H.; Adan, O. (2021) "Hydration of salts as a two-step process: Water adsorption and hydrate formation" *Thermochimica Acta* 695 178819

[18] Clark, R.; Gholamibozanjani, G.; Woods, J.; Kaur, S.; Odukomaiya, A.; Al-Hallaj, S.; Farid, M. (2022) "Experimental screening of salt hydrates for thermochemical energy storage for building heating application" *J. of Energy Storage* 51 104415

[19] Sögütoglu, L.; Steiger, M.; Houben, J.; Biemans, D.; Fischer, H.R.; Donkers, P.; Huinink, H.; Adan, O.C.G. (2019) "Understanding the Hydration Process of Salts: The Impact of a Nucleation Barrier" *Cryst. Growth Des.* 19 pp. 2279-2288

[20] Rammelberg, H.U.; Schmidt, T.; Ruck, W. (2012) "Hydration and dehydration of salt hydrates and hydroxides for thermal energy storage – kinetics and energy release" *Energy Procedia* 30 pp. 362-369

[21] Merdaw, A.A.; Sharif, A.O.; Derwish, G.A.W. "Mass transfer in pressure-driven membrane separation processes, Part II" *Chem. Eng. J.* 168 pp. 229-240

[22] Purohit, B.K.; Sistla, V.S. (2021) "Inorganic salt hydrate for thermal energy storage application: A review" *Energy Storage* 3 2

[23] Zhang, Y.; Wang, R. (2020) "Sorption thermal energy storage: Concept, process, applications and perspectives" *Energy Storage Mater.* 27 pp. 352-369

[24] Yan, T.; Zhang, H. (2022) "A critical review of salt hydrates as thermochemical sorption heat storage materials: Thermophysical properties and reaction kinetics" *Solar Energy* 242 pp. 157-183

[25] Gennick, I.; Harmon, K. M. (1975). Hydrogen bonding. VI. Structural and infrared spectral analysis of lithium hydroxide monohydrate and cesium and rubidium hydroxide hydrates. *Inorganic Chemistry*, *14*(9), 2214-2219

[26] Paroutoglou, E.; Afshari, A.; Fojan, P.; Hultmark, G. (2021). Investigation of Thermal Behavior of Paraffins, Fatty Acids, Salt Hydrates and Renewable Based Oils as PCM. In *14th International Renewable Energy Storage Conference 2020 (IRES 2020)* (pp. 34-40). Atlantis Press.

[27] Purohit, B. K.; Sistla, V. S. (2021). Inorganic salt hydrate for thermal energy storage application: A review. *Energy Storage*, *3*(2), e212.

[28] Kumar, N.; Banerjee, D. (2018). A Comprehensive Review of Salt Hydrates as Phase Change Materials (PCMs). *International Journal of Transport Phenomena*, *15*(1).

[29] Zhou, W.; Jiang, J.; Wu, H.; Hu, D.; Li, P.; Yang, X.; Jia, X. (2021). Facile preparation of binary salt hydrates/carbon nanotube composite for thermal storage materials with enhanced structural stability. *ACS Applied Energy Materials*, *4*(5), 4561-4569.

[30] Li, W.; Klemes, J.J.; Wang, Q.; Zeng, M. (2022) "Salt hydrate-based gas-solid thermochemical energy storage: Current progress, challenges, and perspectives" *Renew. and Sustain. Energy Reviews* 154 111846

[31] Kumar, N.; Hirschey, J.; LaClair, T.; Gluesenkamp, K.R.; Graham, S. (2019) "Review of stability and thermal conductivity enhancements for salt hydrates" *J. of Energy Storage* 24 100794

[32] Li, C.; Li, Q.; Lu, X.; Ge, R.; Du, Y.; Xiong, Y. (2022) "Inorganic salt based shape-stabilized composite phase change materials for medium and high temperature thermal energy storage: Ingredients selection, fabrication, microstructural characteristics and development, and applications" *J. of Energy Storage* 55 105252

[33] Mehrabadi, A.; Farid, M. (2018) "New salt hydrate composite for low-grade thermal energy storage" *Energy* 164 pp. 194-203

[34] Druske, M.; Fopah-Lele, A.; Korhammer, K.; Rammelberg, H.U.; Wegscheider, N.; Ruck, W.; Schmidt, T. (2014) "Developed materials for thermal energy storage: synthesis and characterization" *Energy Procedia* 61 pp. 96-99

[35] Sinko, R.; Mishra, S.; Ruiz, L.; Brandis, N.; Keten, S. (2014) "Dimension of Biological Cellulose Nanocrystals Maximize Fracture Strength" *ACS Macro Lett.* 3 pp. 64-69

[36] Yang, J.; Zhao, J.; Xu, F.; Sun, R. (2013) "Revealing Strong Nanocomposite Hydrogels Reinforced by Cellulose Nanocrystals: Insight into Morphologies and Interactions" *ACS Appl. Mater. Interfaces* 5 pp. 12960-12967

[37] Bai, L.; Bossa, N.; Qu, F.; Winglee, J.; Li, G.; Sun, K.; Liang, H.; Wiesner, M.R. (2017) "Comparison of Hydrophilicity and Mechanical Properties of Nanocomposite Membranes with Cellulose Nanocrystals and Carbon Nanotubes" *Environ. Sci. Technol.* 51 pp. 253-262

[38] Seabra, A.B.; Bernardes, J.S.; Favara, W.J.; Paula, A.J.; Duran, N. (2018) "Cellulose nanocrystals as carriers in medicine and their toxicities: A review" *Carbohydrate Polymers* 181 pp. 514-527

[39] dos Santos, R.M.; Flauzino Neto, W.P.; Silverio, H.A.; Martins, D.F.; Dantas, N.O.; Pasquini, D. (2013) "Cellulose nanocrystals from pineapple leaf, a new approach for the reuse of this agro-waste" *Industrial Crops and Products* 50 pp. 707-714

[40] Xie, N.; Huang, Z.; Luo, Z.; Gao, X.; Fang, Y.; Zhang, Z. (2017) "Inorganic Salt Hydrate for Thermal Energy Storage" *Appl. Sci.* 7 1317

[41] Mazur, N.; Blijlevens, M.A.R.; Ruliaman, R.; Fischer, H.; Donkers, P.; Meekes, H.; Vlieg, E.; Adan, O.; Huinink, H. (2023) "Revisiting salt hydrate selection for domestic heat storage applications" *Renew. Energy* 218 119331

[42] Li, W.; Zeng, M.; Wang, Q. (2020) "Development and performance investigation of $MgSO_4/SrCl_2$ composite salt for mid-low temperature thermochemical heat storage" *Solar Energy Mater. & Solar Cells* 210 110509

[43] Ye, Z.; Liu, H.; Wang, W.; Liu, H.; Lv, J.; Yang, F. (2022). Reaction/sorption kinetics of salt hydrates for thermal energy storage. *Journal of Energy Storage* 56 106122.

[44] Solé, A.; Miró, L.; Barreneche, C.; Martorell, I.; Cabeza, L. F. (2015). Corrosion of metals and salt hydrates used for thermochemical energy storage. *Renewable Energy* 75 pp. 519-523.

[45] U.S. Energy Information Administration. U.S. energy facts explained. https://www.eia.gov/energyexplained/us-energy-facts/ 2023

[46] Chavam S, Rudrapati R, Manickam S. A comprehensive review on current advances of thermal energy storage and its applications. Alexandria Eng. J. 2021;61**:**5455-5463

[47] Lefebvre D, Handan Tezel F. A review of energy storage technologies with a focus on adsorption thermal energy storage processes for heating applications. Renew. Sustain. Energy Rev. 2017;67:116-125

[48] Hua W, Yan H, Zhang X, Xu X, Zhang L, Shi Y. Review of salt hydrates-based thermochemical adsorption thermal storage technologies. J. of Energy Storage 2022;56:106158

[49] Yang H, Wang C, Tong L, Yin S, Wang L, Ding Y. Salt Hydrate Adsorption Material-Based Thermochemical Energy Storage for Space Heating Application: A Review. Energies 2023;16:2875

[50] Lass-Seyoum A, Borozdenko D, Friedrich T, Schonfeld K, Adler J, Mack S. Experimental Investigations on Adsorption and Surface Characteristics of Salt Hydrates and Hydrophobic Porous Matrix Based Composites. Mod. Environ. Sci. and Eng. 2017;3:67-81

[51] Zbair M, Bennici S. Survey Summary on Salts Hydrates and Composites Used in Thermochemical Sorption Heat Storage: A Review. Energies 2021;14:3105

[52] Sharma SD, Sagara K. Latent Heat Storage Materials and Systems: A Review. Int. J. of Green Energy 2005;2:1-56

[53] Suresh C, Saini RP. Thermal performance of sensible and latent heat thermal energy storage systems. Int. J. of Energy Research 2020;6:4743-4758

[54] Ferchaud C. Experimental study of salt hydrates for thermochemical seasonal heat storage. [PhD Thesis] Technische Universiteit Eindhoven 2016

[55] Hayatina I, Auckaili A, Farid M. Review on Salt Hydrate Thermochemical Heat Transformer. Energies 2023;16:4668

[56] Kiyabu S, Girard P, Siegel DJ. Discovery of Salt Hydrates for Thermal Energy Storage. J. Am. Chem. Soc. 2022;144:21617-21627

[57] Chen L. Chemical potential and Gibbs free energy. Material Matters 2020;44:520-523

[58] Donald H, Jenkins B. Thermodynamics of the Relationship between Lattice Energy and Lattice Enthalpy. J. of Chem. Education 2005;82:950-952

[59] Sögütoglu L, Steiger M, Houben J, Biemans D, Fischer HR, Donkers P, Huinink H, Adan OCG. Understanding the Hydration Process of Salts: The Impact of a Nucleation Barrier. Cryst. Growth & Des. 2019;19:2279-2288

[60] Sato M, Hattanji T. A laboratory experiment on salt weathering by humidity change: salt damage induced by deliquescence and hydration. Progress in Earth and Planetary Science 2018;5:84

[61] Sögütoglu L, Birkelbach F, Werner A, Fischer H, Huinink H, Adan O. Hydration of salts as a two-step process: Water adsorption and hydrate formation. Thermochimica Acta 2021;695:178819

[62] Zhang Y, Wang R. Sorption thermal energy storage: Concept, process, applications and perspectives. Energy Storage Materials 2020;27:352-369

[63] Clark R, Gholamibozanjani G, Woods J, Kaur S, Odukomaiya A, Al-Hallaj S, Farid M. Experimental screening of salt hydrates for thermochemical energy storage for building heating application. J. of Energy Storage 2022;51:104415

[64] Quinn R, Appleby JB, Pez GP. Salt Hydrates: New Reversible Absorbents for Carbon Dioxide. J. Am. Chem. Soc. 1995;117:329-335

[65] Hinmers S, Atkinson GH, Critoph RE, Van der Pal M. Modelling and analysis of Ammonia Sorption Reactions in Halide Salts. Int. J. of Refrigeration 2022;137:188-211

[66] Merdaw AA, Sharif AO, Derwish GAW. Mass transfer in pressure-driven membrane separation processes, Part II. Chem. Eng. J. 2011;168:229-240

[67] Rammelberg HU, Schmidt T, Ruck W. Hydration and dehydration of salt hydrates and hydroxides for thermal energy storage – kinetics and energy release. Energy Procedia 2012;30:362-369

[68] Sarbu I, Dorca A. Review on heat transfer analysis in thermal energy storage using latent heat storage systems and phase change materials. Int. J. of Energy Research 2018;43:29-64

[69] N'Tsoukpoe KE, Schmidt T, Rammelberg HU, Watts BA, Ruck WKL. A systematic multi-step screening of numerous salt hydrates for low temperature thermochemical energy storage Applied Energy 2014;124:1-16

[70] Purohit BK, Sistla VS. Inorganic salt hydrate for thermal energy storage application: A review Energy Storage 2021;3:2

[71] Li W, Klemes JJ, Wang Q, Zeng M. Salt hydrate-based gas-solid thermochemical energy storage: Current progress, challenges, and perspectives Renew. and Sustain. Energy Reviews 2022;154:111846

[72] Li W, Zeng M, Wang Q. Development and performance investigation of $MgSO_4/SrCl_2$ composite salt for mid-low temperature thermochemical heat storage. Solar Energy Materials & Solar Cells 2020;210:110509

[73] Issayan G, Zettl B, Somitsch W. Developing and Stabilizing Salt-Hydrate Composites as Thermal Storage Materials. Int. Renew. Energy Storage Conf. 2020

[74] Yan T, Zhang H. A critical review of salt hydrates as thermochemical sorption heat storage materials: Thermophysical properties and reaction kinetics. Solar Energy 2022;242:157-183

[75] Li C, Li Q, Lu X, Ge R, Du Y, Xiong Y. Inorganic salt based shape-stabilized composite phase change materials for medium and high temperature thermal energy storage: Ingredients selection, fabrication, microstructural characteristics and development, and applications. J. of Energy Storage 2022;55:105252

[76] Sharif F, Muhammad N, Zafar T. Cellulose Based Biomaterials: Benefits and Challenges. Biofibers and Biopolymers for Biocomposites 2020:229-246

[77] Kumar N, Hirschey J, LaClair T, Gluesenkamp KR, Graham S. Review of stability and thermal conductivity enhancements for salt hydrates" J. of Energy Storage 2019;24:100794

[78] Mehrabadi A, Farid M. New salt hydrate composite for low-grade thermal energy storage. Energy 2018;164:194-203

[79] Salviati S, Carosio F, Cantamessa F, Medina L, Berglund LA, Saracco G, Fina A. Ice-templated nanocellulose porous structure enhances thermochemical storage kinetics in hydrated salt/graphite composites. Renew. Energy 2020;160:698-706

[80] Druske M, Fopah-Lele A, Korhammer K, Rammelberg HU, Wegscheider N, Ruck W, Schmidt T. Developed materials for thermal energy storage: synthesis and characterization. Energy Procedia 2014;61:96-99

[81] Yang X, Li S, Huang H, Li J, Kobayashi N, Kubota M. Effect of Carbon Nanoadditives on Lithium Hydroxide Monohydrate-Based Composite Materials for Low Temperature Chemical Heat Storage. Energies 2017;10:644

[82] Oh K, Kwon S, Xu W, Wang X, Toivakka M. Effect of micro- and nanofibrillated cellulose on the phase stability of sodium sulfate decahydrate based phase change material. Cellulose 2020;27:5003-5016

[83] Shen Z, Oh K, Kwon S, Toivakka M, Lee HL. Use of cellulose nanofibril (CNF)/silver nanoparticles (AgNPs) composite in salt hydrate phase change material for efficient thermal energy storage. Int. J. of Biological Macromolecules 2021;174:402-412

[84] Li X, Zhou Y, Nian H, Zhu F, Ren X, Dong O, Hai C, Shen Y, Zeng J. Preparation and thermal energy storage studies of $CH_3COONa{\cdot}3H_2O$ – KCl composites salt system with enhanced phase change performance" Applied Thermal Eng. 2016;102:708-715

[85] Zhou W, Jiang J, Wu H, Hu D, Li P, Yang X, Jia X. Facile Preparation of Binary Salt Hydrates/Carbon Nanotube Composite for Thermal Storage Materials with Enhanced Structural Stability ACS Applied Energy Materials 2021;4:4561-4569

[86] Tao YB, Lin CH, He YL. Preparation and thermal properties characterization of carbonate salt/carbon nanomaterial composite phase change material" Energy Conversion and Management 2015;97:103-110

[87] Zhang B, Zhang Z, Kapar S, Ataeian P, da Silva Bernardes J, Berry R, Zhao W, Zhou G, Tam KC. Microencapsulation of Phase Change Materials with Polystyrene/Cellulose Nanocrystal Hybrid Shell via Pickering Emulsion Polymerization" ACS Sustainable Chem. Eng. 2019;7:17756-17767

[88] Fan X, Guan Y, Li Y, Yu H, Marek J, Wang D, Militky J, Zou Z, Yao J. Shape-Stabilized Cellulose Nanocrystal-Based Phase-Change Materials for Energy Storage. ACS Appl. Nano Mater. 2020;3:1741-1748

[89] Abdalkarim SYH, Ouyang Z, Yu H, Li Y, Wang C, Asad RAM, Lu Y, Yao J. Magnetic cellulose nanocrystals hybrids reinforced phase change fiber composite with highly thermal energy storage efficiencies. Carbohydrate Polymers 2021;254:117481

[90] Dardari O, Amadine O, Sair S, Ousaleh HA, Essamlali Y, Idrissi AE, Aboulhrouz S, Danoun K, Maati H, Zahouily M. Cellulose nanocrystal stabilized copper nanoparticles for grafting phase change materials with high thermal conductivity. J. of Energy Storage 2024;79:110182

[91] Gladen A, Bajwa D. A Novel Composite Material of Hygroscopic Salt Stabilized by Nanocellulose for Thermochemical Energy Storage. ASME Int. Conf. on Energy Sustainability 2021

[92] Karna S. Screening of Thermochemical Nanocellulose Based Salt Hydrates for Thermal Energy Storage. [Master's Thesis] North Dakota State University 2024

[93] Blake D, Bajwa D, Gladen A, Turnaoglu T, Karna S (2024) Development of salt-based nanocellulose composites for thermal energy storage. ACS Annual Conf Div of Energy and Fuels

[94] de Gennaro B, Cappi A, de Gennaro M, Bianco N, Langella A, Cappelletti P, Marocco A, Aprea P, Pansini M. Use of Zeolites in the Capture and Storage of Thermal Energy by Water Desorption—Adsorption Cycles. Materials 2022;15:5574

[95] Zhao Q, Lin J, Huang H, Wu Q, Shen Y, Xiao Y. Optimization of thermochemical energy storage systems based on hydrated salts: A review. Energy and Buildings 2021;244:111035

[96] Aarts J, Fischer H, Adan O, Huinink H. Towards stable performance of salt hydrates in thermochemical energy storage: A review. J. of Energy Storage 2025;114:115726

[97] Hassanabadi S, Girnik IS, Bahrami M. Sorption kinetics of salt-in-porous-matrix composites: The effect of expanded natural graphite on cooling power. Int. J. of Refrigeration 2024;166:129-138

[98] Taurbekov A, Fierro V, Kuspanov Z, Abdisattar A, Atamanova T, Kaidar B, Mansurov Z Atamonov M. Nanocellulose and carbon nanotube composites: A universal solution for environmental and energy challenges. J of Environ. Chem. Eng. 2024;12(5):113262

[99] Kuziel AW, Dzido G, Turczyn R, Jedrysiak RG, Kolanowska A, Tracz A, Zieba W, Cyganiuk A, Terzyk AP, Boncel S. Ultra-long carbon nanotube-paraffin composites of

record thermal conductivity and high phase change enthalpy among paraffin-based heat storage materials. J. of Energy Storage 2021;36:102396

[100] Wijnhorst R, Demmenie M, Jambon-Puillet E, Ariese F, Bonn D, Shahidzadeh N. Softness of hydrates salt crystals under deliquescence. Nature Comm. 2023;14:1090

[101] Blake D, Bajwa D, Gladen A, Turnaoglu T, Karna S. Development of salt-based nanocellulose composites for thermal energy storage. ACS Annual Conf. Div. of Energy and Fuels 2024

[102] Wang S, Stahlbuhk A, Steiger M. Hydration and deliquescence behavior of calcium chloride hydrates. Fluid Phase Equilibria 2024;585:114171

[103] Anjum N, Niemi A, Blake D, Bajwa D, Gladen A. Impact of Cycling on the Structure of Crystal Nanocellulose-Salt Composite Materials for Thermal Energy Storage. ASME Int. Conf. on Energy Sustainability 2025

[104] Prathapan R, Thapa R, Garnier G, Tabor RF. Modulating the zeta potential of cellulose nanocrystals using salts and surfactants. Colloids and Surfaces A: Physiochem. And Eng. Aspects 2016;509:11-18

[105] Musah M, Azeh Y, Mathew JT, Umar MT, Abdulhamid Z, Muhammad AI. Adsorption Kinetics and Isotherm Models: A Review. Caliphate J. of Science & Tech. 2021;1:20-26

[106] Das SK. Kinetics of Salt Hydrates and Crystalline Nanocellulose-Salt Composites for Thermochemical Energy Storage. [Master's Thesis] North Dakota State University 2025

[107] Habibi Y, Lucia LA, Rojas OJ (2010) Cellulose Nanocrystals: Chemistry, Self-Assembly, and Applications. Chem Rev 110:3479-3500

[108] Rashid AB, Hoque ME, Kabir N, Rifat FF, Ishrak H, Alqahtani A, Chowdhury MEH (2023) Synthesis, Properties, Applications, and Future Prospective of Cellulose Nanocrystals. Polym 15(20):4070

[109] Pakzad A, Simonsen J, Heiden PA, Yassar RS (2012) Size effects on the nanomechanical properties of cellulose I nanocrystals. J of Mat Research 27(3):528-536. https://doi.org/10.1557/jmr.2011.288

[110] Forsgren L, Sahlin-Sjovold K, Venkatesh A, Thunberg J, Kadar R, Boldizar A, Westman G, Rigdahl M (2018) Composites with surface-grafted cellulose nanocrystals (CNC). J of Mat. Sci. 54:3009-3022

[111] Kumar S, Graninger G, Hawkin SC, Falzon BG (2021) A nanostructured cellulose-based interphase layer to enhance the mechanical performance of glass fibre-reinforced polymer composites. Compos. Part A: Appl. Sci. and Manuf.

[112] Raza M, Abu-Jdayil B, Banat F, Al-Marzouqi AH (2022) Isolation and Characterization of Cellulose Nanocrystals from Date Palm Waste. ACS Omega 7(29):25366-25379

[113] Babaei-Ghazvini A, Vafakish B, Patel R, Falua KJ, Dunlop MJ, Acharya B (2024) Cellulose nanocrystals in the development of biodegradable materials: A review on CNC resources, modification and their hybridization. Int J of Biological Macromolecules 258:128834

[114] Almashhadani AQ, Leh CP, Chan S, Lee CY, Goh CF (2022) Nanocrystalline cellulose isolation via acid hydrolysis from non-woody biomass: Importance of hydrolysis parameters. Carb Polym 286:119285,

[115] Trache D, Hussin MH, Haafiz MKM, Thakur VK (2017) Recent progress in cellulose nanocrystals: sources and production. Nanoscale 9:1763-1786

[116] Garcia A, Labidi J, Belgacem MN, Bras J (2017) The nanocellulose biorefinery: woody versus herbaceous agricultural wastes for NCC production. Cellulose 24:693-704

[117] Bondeson D, Mathew A, Oksman K (2006) Optimization of the isolation of nanocrystals from microcrystalline cellulose by acid hydrolysis. Cellulose 13:171-180

[118] Thompson L, Azadmanjiri J, Nikzad M, Sbarski I, Wang J, Yu A (2019) Cellulose Nanocrystals: Production Functionalization and Advanced Applications. Rev on Adv Mat Sci 58:1-16

[119] George J, Sabapathi SN (2015) Cellulose nanocrystals: synthesis, functional properties, and applications. Nanotechnol. Sci. Appl. 8:45-54

[120] Missale E, Maniglio D, Speranza G, Frasconi M, Pantano MF (2024) Cellulose Nanocrystal Composites with Enhanced Mechanical Properties for Robust Transparent Thin Films. *ACS App Nano Mat 7*:18167-18176

[121] Fan X, Guan Y, Li Y, Yu H, Marek J, Wang D, Militky J, Zou Z, Yao J (2020) Shape-Stabilized Cellulose Nanocrystal-Based Phase-Change Materials for Energy Storage. ACS Appl Nano Mat 3:1741-1748

[122] Abdalkarim SYH, Ouyang Z, Yu H, Li Y, Wang C, Asad RAM, Lu Y, Yao J (2021) Magnetic cellulose nanocrystals hybrids reinforced phase change fiber composite with highly thermal energy storage efficiencies. Carb Polym 254:117481

[123] Gladen A, Bajwa D (2021) A Novel Composite Material of Hygroscopic Salt Stabilized by Nanocellulose for Thermochemical Energy Storage. ASME Int Conf on Energy Sustain

[124] Clark R, Gholamibozanjani G, Woods J, Kaur S, Odukomaiya A, Al-Hallaj S, Farid M (2022) Experimental screening of salt hydrates for thermochemical energy storage for building heating application. J of Energy Storage 51:104415

[125] Blake D, Gladen A, Bajwa D (2025) Salt hydrate bio-composites for thermal energy storage: A concise review. J. of Energy Storage 133:117874

[126] Blake D, Bajwa D, Gladen A, Turnaoglu T, Karna S (2024) Development of salt-based nanocellulose composites for thermal energy storage. ACS Annual Conf Div of Energy and Fuels

[127] Wei X, Lin T, Lu L, Yu M, Yin X (2024) Enhanced homogeneity and flexibility in a humidity sensor using cellulose nanocrystal-based composite film with circular shear flow. Int J of Bio Macromolecules 263:130293

[128] Wang B, Zhou J, Wang Z, Mu S, S R, Wang Z (2020) Cellulose nanocrystal/plant oil polymer composites with hydrophobicity, humidity-sensitivity, and high wet strength. Carb Polym 231:115739

[129] Babaei-Ghazvini A, Acharya B (2021) Humidity-Responsive Photonic Films and Coatings and Based on Tuned Cellulose Nanocrystals/Glycerol/Polyethylene Glycol. Polym 13:3695

[130] Manzano LMG, Cruz MAR, Tun NMM, Gonzalez AV, Hernandez JHM (2021) Effect of Cellulose and Cellulose Nanocrystal Contents on the Biodegradation under Composting Conditions, of Hierarchical PLA Biocomposites. Polymers 13(11):1855

[131] Perez J, Munoz-Dorado J, de la Rubia T, Martinez J (2002) Biodegradation and biological treatments of cellulose, hemicellulose and lignin: an overview

[132] Klyosov AA (1990) Trends in biochemistry and enzymology of cellulose degradation. Biochem. 29(47):10577-10585

[133] Coughlan, MP (1985) The properties of fungal and bacterial cellulases with comment on their production and application. Biotech. and Gen. Eng. Rev. 3(1):39-110.

[134] Solhi L, Guccini V, Heise K, Solala I, Niinivaara E, Xu W, Mihhels K, Kroger M, Meng Z, Wohlert J, Tao H, Cranston ED, Kontturi E (2023) Understanding Nanocellulose–Water Interactions: Turning a Detriment into an Asset. Chem Rev 123:1925-2015

[135] Gonzalez JM, Aranda B (2023) Microbial Growth under Limiting Conditions-Future Perspectives. Microorganisms 11(7):1641

[136] Timmermann EO (2003) Multilayer sorption parameters: BET and GAB values? Coll. and Surf. A: Physiochem. and Eng. Asp. 220(1-3):235-260

[137] Thygesen A, Oddershede J, Lilholt H, Thomsen AB, Stahl K (2005) On the determination of crystallinity and cellulose content in plant fibres. Cellulose 12:563-576

[138] Bashir A, Lambert PA, Stedman Y, Hilton AC (2022) Combined Effect of Temperature and Relative Humidity on the Survival of Salmonella Isolates on Stainless Steel Coupons. Int. J of Envron. Res. and Pub. Health 19(2):909

[139] D'Acierno F, Hamad WY, Michal CA, MacLachlan MJ (2020) Thermal Degradation of Cellulose Filaments and Nanocrystals. Biomacromolecules 21:3374-3386

[140] Gotze J, Pan Y, Muller A (2021) Mineralogy and mineral chemistry of quartz: A review. Mineralogical Magazine 85(5):639-664

[141] Segal, L. G. J. M. A., Creely, J. J., Martin Jr, A. E., & Conrad, C. M. (1959). An empirical method for estimating the degree of crystallinity of native cellulose using the X-ray diffractometer. *Textile research journal*, *29*(10), 786-794.

[142] Pan X, Li S, Li Y, Guo P, Zhao X, Cai Y (2022) Resource, characteristic, purification and application of quartz: a review. Minerals Eng 183:107600

[143] Guo X, Wu Y, Xie X (2017) Water vapor sorption properties of cellulose nanocrystals and nanofibers using dynamic vapor sorption apparatus. Sci Reports 7:14207

[144] Serrano-Lotina A, Portela R, Baeza P, Alcolea-Rodriguez V, Villarroel M, Avila P (2023) Zeta potential as a tool for functional materials development. Catalysis Today 423:113862

[145] Bangar SP, Harussani MM, Ilyas RA, Ashogbon AO, Singh A, Trif M, Jafari SM (2022) Surface modification of cellulose nanocrystals: Processes, properties, and applications. Food Hydrocolloids 130:107689

[146] Mamleev V, Bourbigot S, Yvon J (2007) Kinetic analysis of the thermal decomposition of cellulose: The main step of mass loss. J of Anal. And Appl. Pyrolysis 80(1):151-165

[147] Hrcka R, Kucerova V, Honig V (2022) Dry-matter Loss and Changes in the Chemical Composition of Spruce Wood after Long-Term Storing in the Form of Roundwood. Polymers (Basel) 14(16):3400

[148] Silverio HA, Neto WPF, Dantas NO, Pasquini D (2013) Extraction and characterization of cellulose nanocrystals from corncob for application as reinforcing agent in nanocomposites. Ind Crops and Products 44:427-436

[149] Erdal NB, Hakkarainen M (2022) Degradation of Cellulose Derivatives in Laboratory, Man-Made, and Natural Environments. Biomacromolecules 23:2713-2729

[150] O'Neill H, Pingali SV, Petridis L, He J, Mamontov E, Hong L, Urban V, Evans B, Langan P, Smith JC, Davison BH. Dynamics of water bound to crystalline cellulose. Sci. Rep. 7:11840

[151] Singh K, Nitin P, Kasamias K (2024) Surface roughness characterization using representative elementary area (REA) analysis. Sci Reports 14:1785

[152] Wang W, Ma W, Wu M, Sun L (2022) Effect of water molecules at different temperatures on properties of cellulose based on molecular dynamics. BioResources 17:269-280

[153] Etale A, Onyianta AJ, Turner SR, Eichhorn SJ (2023) Cellulose: A Review of Water Interactions, Applications in Composites, and Water Treatment. Chem Rev 123(5):2016-2048

[154] Torstensen J, Ottesen V, Rodriguez-Fabia S, Syverud K, Johansson L, Lervik A (2022) The influence of temperature on cellulose swelling at constant water density. Sci Reports 12:20736

[155] Meriçer, Ç., Minelli, M., Baschetti, M. G., & Lindström, T. (2017). Water sorption in microfibrillated cellulose (MFC): The effect of temperature and pretreatment. *Carbohydrate polymers*, *174*, 1201-1212.

[156] Ogawa Y, Nishiyama Y, Mazeau K (2022) Drying-induced bending deformation of cellulose nanocrystals studied by molecular dynamics simulations. Cellulose 27(17):9779-9786

[157] Lunardi CN, Gomes AJ, Rocha FS, Tommaso JD, Patience GS (2020) Experimental methods in chemical engineering: Zeta potential. The Can J of Chem Eng 99:627-639

[158] Abitbol T, Kam D, Levi-Kalisman Y, Gray DG, Shoseyov O (2018) Surface Charge Influence on the Phase Separation and Viscosity of Cellulose Nanocrystals. Langmuir 34(13):3925-3933

[159] Neely WB (1985) Environmental Exposure from Chemicals. CRC Press

[160] Roman M, Winter WT (2004) Effect of Sulfate Groups from Sulfuric Acid Hydrolysis on the Thermal Degradation Behavior of Bacterial Cellulose. Biomacromolecules 5(5):1671-1677

[161] Peleg M (2022) Models of the water activity effect on microbial growth rate and initiation. App Microbio and Biotechn 106:1375-1382

[162] Yin Q, Liu H (2021) Drying Stress and Strain of Wood: A Review. Appl. Sci. 11(11):5023

[163] Martinelli FRB, Pariz MG, de Andrade R, Ferreria SR, Marques FA, Monteiro SN, de Azevedo ARG (2024) Influence of drying temperature on coconut-fibers. Sci. Rep. 14:6421

[164] Singh G, Chandoha-Lee C, Zhang W, Rennecker S, Vikesland PJ, Pruden A (2016) Biodegradation of nanocrystalline cellulose by two environmentally-relevant consortia. Water Research 104:137-146

[165] Ioelovich M (2024) Thermodynamics of enzymatic hydrolysis of cellulose. World J of Adv Research and Rev 21(02):577-586

[166] Xie, S., Zhang, X., Walcott, M. P., & Lin, H. (2018). Applications of cellulose nanocrystals: a review. *Engineered Science*, *2*(16), 4-16.

[167] Trache, D., Hussin, M. H., Haafiz, M. M., & Thakur, V. K. (2017). Recent progress in cellulose nanocrystals: sources and production. *Nanoscale*, *9*(5), 1763-1786.

[168] Tang, Y., Yang, H., & Vignolini, S. (2022). Recent progress in production methods for cellulose nanocrystals: leading to more sustainable processes. *Advanced Sustainable Systems*, *6*(3), 2100100.

[169] Habeeb, A. (2024). The benefits of sugar beet pulp by-products used in animal feeding on rumen fermentation, nutrient utilization, blood components, growth, and milk yield with some principal considerations prior to introducing to the animals. *Indiana Journal of Agriculture and Life Sciences*, *4*(4), 1-13.

[170] Ptak, M., Skowrońska, A., Pińkowska, H., & Krzywonos, M. (2021). Sugar beet pulp in the context of developing the concept of circular bioeconomy. *Energies*, *15*(1), 175.

[171] Joanna, B., Michal, B., Piotr, D., Agnieszka, W., Dorota, K., & Izabela, W. (2018). Sugar beet pulp as a source of valuable biotechnological products. In *Advances in biotechnology for food industry* (pp. 359-392). Academic Press.

[172] Vanderfleet, O. M., & Cranston, E. D. (2021). Production routes to tailor the performance of cellulose nanocrystals. *Nature Reviews Materials*, *6*(2), 124-144.

[173] Raza, M., & Abu-Jdayil, B. (2022). Cellulose nanocrystals from lignocellulosic feedstock: a review of production technology and surface chemistry modification. *Cellulose*, *29*(2), 685-722.

[174] Fatemi, S. M., Robatjazi, S. M., Zarei, A. R., & Hosseini, S. G. (2023). Extraction of Cellulose Nanocrystal from Sugar Beet Pulp and its Characterization. *Journal of Advanced Defense Science & Technology*, *13*(4), 263-270.

[175] Whitfield, M. B., Chinn, M. S., & Veal, M. W. (2016). Improvement of acid hydrolysis procedures for the composition analysis of herbaceous biomass. *Energy & Fuels*, *30*(10), 8260-8269.

[176] Bondeson, D., Mathew, A., & Oksman, K. (2006). Optimization of the isolation of nanocrystals from microcrystalline cellulose by acid hydrolysis. *Cellulose*, *13*(2), 171-180.

[177] Lin, N., & Dufresne, A. (2014). Surface chemistry, morphological analysis and properties of cellulose nanocrystals with gradiented sulfonation degrees. *Nanoscale*, *6*(10), 5384-5393.

[178] D'Acierno, F., Michal, C. A., & MacLachlan, M. J. (2023). Thermal stability of cellulose nanomaterials. *Chemical reviews*, *123*(11), 7295-7325.

[179] Vanderfleet, O. M., Reid, M. S., Bras, J., Heux, L., Godoy-Vargas, J., Panga, M. K., & Cranston, E. D. (2019). Insight into thermal stability of cellulose nanocrystals from new hydrolysis methods with acid blends. *Cellulose*, *26*(1), 507-528.

[180] Zhang, Y., Jing, X., Jing, K., Chang, L., & Bao, W. (2015). Study on the pore structure and oxygen-containing functional groups devoting to the hydrophilic force of dewatered lignite. *Applied Surface Science*, *324*, 90-98.

[181] Mohomane, S. M., Motloung, S. V., Koao, L. F., & Motaung, T. E. (2022). Effects of acid hydrolysis on the extraction of cellulose nanocrystals (CNCs): A review. *Cellul. Chem. Technol*, *56*(7-8), 691-703.

[182] Gilli, G., & Gilli, P. (2009). *The nature of the hydrogen bond: outline of a comprehensive hydrogen bond theory* (Vol. 23). Oxford university press.

[183] Parthasarathi, R., Subramanian, V., & Sathyamurthy, N. J. T. J. P. C. A. (2006). Hydrogen bonding without borders: an atoms-in-molecules perspective. *The Journal of Physical Chemistry A*, *110*(10), 3349-3351.

[184] Fan, M., Li, C., Shao, Y., Zhang, S., Gholizadeh, M., & Hu, X. (2022). Pyrolysis of cellulose: Correlation of hydrophilicity with evolution of functionality of biochar. *Science of The Total Environment*, *825*, 153959.

[185] Aljafree, N. F. A., Norrrahim, M. N. F., Samsuri, A., & Yunus, W. M. Z. W. (2025). Advancements in nitrated nanocellulose: from structural insights to energetic applications. *Cellulose*, 1-53.

[186] Rana, A. K., Frollini, E., & Thakur, V. K. (2021). Cellulose nanocrystals: Pretreatments, preparation strategies, and surface functionalization. *International Journal of Biological Macromolecules*, *182*, 1554-1581.

[187] Rana, A. K., Frollini, E., & Thakur, V. K. (2021). Cellulose nanocrystals: Pretreatments, preparation strategies, and surface functionalization. *International Journal of Biological Macromolecules*, *182*, 1554-1581.

[188] Bolat, F., Ghitman, J., Necolau, M. I., Vasile, E., & Iovu, H. (2023). A comparative study of the impact of the bleaching method on the production and characterization of cotton-origin nanocrystalline cellulose by acid and enzymatic hydrolysis. *Polymers*, *15*(16), 3446

[189] Van der Hagen, M., & Järnberg, J. (2009). *140. Sulphuric, hydrochloric, nitric and phosphoric acids*.

[190] Li, M., Wang, L. J., Li, D., Cheng, Y. L., & Adhikari, B. (2014). Preparation and characterization of cellulose nanofibers from de-pectinated sugar beet pulp. *Carbohydrate Polymers*, *102*, 136-143.

[191] Hietala, M., Sain, S., & Oksman, K. (2017). Highly redispersible sugar beet nanofibers as reinforcement in bionanocomposites. *Cellulose*, *24*(5), 2177-2189.

[192] Vanderfleet, O. M., Osorio, D. A., & Cranston, E. D. (2018). Optimization of cellulose nanocrystal length and surface charge density through phosphoric acid hydrolysis. *Philosophical Transactions of the Royal Society A: Mathematical, Physical and Engineering Sciences*, *376*(2112), 20170041.

[193] Nam, S., Liu, Y., He, Z., Hinchliffe, D. J., & Fang, D. (2024). Assessment of Segal method for identifying crystallinity evolution in developing cotton fibers. *Agricultural & Environmental Letters*, *9*(1), e20138.

[194] Shindo, D., & Oikawa, T. (2002). Energy dispersive x-ray spectroscopy. In *Analytical electron microscopy for materials science* (pp. 81-102). Tokyo: Springer Japan.

[195] Sluiter, J. B., Ruiz, R. O., Scarlata, C. J., Sluiter, A. D., & Templeton, D. W. (2010). Compositional analysis of lignocellulosic feedstocks. 1. Review and description of methods. *Journal of agricultural and food chemistry*, *58*(16), 9043-9053.

[196] Berthomieu, C., & Hienerwadel, R. (2009). Fourier transform infrared (FTIR) spectroscopy. *Photosynthesis research*, *101*(2), 157-170.

[197] Segal, L., Creely, J.J., Martin, A.E., Conrad, C.M. (1959). An Empirical Method for Estimating the Degree of Crystallinity of Native Cellulose Using the X-Ray Diffractometerl. *Textile Research Journal*, *29*(10), 786-794.

[198] Dassanayake, R. S., Dissanayake, N., Fierro, J. S., Abidi, N., Quitevis, E. L., Boggavarappu, K., & Thalangamaarachchige, V. D. (2023). Characterization of cellulose nanocrystals by current spectroscopic techniques. *Applied Spectroscopy Reviews*, *58*(3), 180-205.

[199] Chen, C. H., Soo, J. C., Young, L. H., Wu, T. N., Yoon, C., Lai, C. Y., & Tsai, P. J. (2014). Effect of the quartz particle size on XRD quantifications and its implications for field collected samples. *Aerosol and Air Quality Research*, *14*(6), 1573-1583.

[200] Ioelovich, M. (2022). Features of water vapor sorption by cellulose materials. *World Journal of Advanced Research and Reviews*, *13*(3), 254-263.

[201] French, A. D.; & Santiago Cintrón, M. (2013). Cellulose polymorphy, crystallite size, and the Segal Crystallinity Index. *Cellulose*, *20*(1), 583-588.

[202] Nam, S.; Liu, Y., He, Z.; Hinchliffe, D. J.; & Fang, D. (2024). Assessment of Segal method for identifying crystallinity evolution in developing cotton fibers. *Agricultural & Environmental Letters*, *9*(1), e20138.

[203] Gustafsson, J.; Mikkola, P.; Jokinen, M.; & Rosenholm, J. B. (2000). The influence of pH and NaCl on the zeta potential and rheology of anatase dispersions. *Colloids and Surfaces A: Physicochemical and Engineering Aspects*, *175*(3), 349-359.

[204] Zhu, J. Y., Agarwal, U. P., Ciesielski, P. N., Himmel, M. E., Gao, R., Deng, Y., ... & Österberg, M. (2021). Towards sustainable production and utilization of plant-biomass-based nanomaterials: a review and analysis of recent developments. *Biotechnology for Biofuels*, *14*(1), 114.

[205] Hou, M., Wang, L., Xu, Q., Zhang, X., Yang, X., Zhang, L., ... & Liu, L. (2024). Utilization of waste cotton fibers by extracting nanocellulose crystals: a study on phosphoric acid method compared with sulfuric acid method and TEMPO oxidation method. *Fibers and Polymers*, *25*(11), 4271-4281.

[206] Sahu, P., & Gupta, M. K. (2022). Water absorption behavior of cellulosic fibres polymer composites: A review on its effects and remedies. *Journal of Industrial Textiles*, *51*(5_suppl), 7480S-7512S.

[207] Etale, A., Onyianta, A. J., Turner, S. R., & Eichhorn, S. J. (2023). Cellulose: a review of water interactions, applications in composites, and water treatment. *Chemical reviews*, *123*(5), 2016-2048.

[208] Thijs, H. M., Becer, C. R., Guerrero-Sanchez, C., Fournier, D., Hoogenboom, R., & Schubert, U. S. (2007). Water uptake of hydrophilic polymers determined by a thermal gravimetric analyzer with a controlled humidity chamber. *Journal of Materials Chemistry*, *17*(46), 4864-4871.

[209] Mänttäri, M., Pihlajamäki, A., & Nyström, M. (2006). Effect of pH on hydrophilicity and charge and their effect on the filtration efficiency of NF membranes at different pH. *Journal of Membrane Science*, *280*(1-2), 311-320.

[210] Stachurski, Z. H. (2011). On structure and properties of amorphous materials. *Materials*, *4*(9), 1564-1598.

[211] Harris, D., & DeBolt, S. (2008). Relative crystallinity of plant biomass: studies on assembly, adaptation and acclimation. *PLoS One*, *3*(8), e2897.

[212] Yoshida, A., Tanahashi, I., & Nishino, A. (1990). Effect of concentration of surface acidic functional groups on electric double-layer properties of activated carbon fibers. *Carbon*, *28*(5), 611-615.

[213] Reid, M. S., Villalobos, M., & Cranston, E. D. (2017). Benchmarking cellulose nanocrystals: from the laboratory to industrial production. *Langmuir*, *33*(7), 1583-1598.

[214] Henniges, U., & Potthast, A. (2009). Bleaching revisited: Impact of oxidative and reductive bleaching treatments on cellulose and paper.

[215] Almashhadani, A. Q., Leh, C. P., Chan, S. Y., Lee, C. Y., & Goh, C. F. (2022). Nanocrystalline cellulose isolation via acid hydrolysis from non-woody biomass: Importance of hydrolysis parameters. *Carbohydrate Polymers*, *286*, 119285

[216] Gomaa, M.; Al-Badaani, A. A.; Hifney, A. F.; & Adam, M. S. (2021). Industrial optimization of alkaline and bleaching conditions for cellulose extraction from the marine seaweed Ulva lactuca. *Journal of Applied Phycology*, *33*(6), 4093-4103.

[217] Lee, J. W.; & Jeffries, T. W. (2011). Efficiencies of acid catalysts in the hydrolysis of lignocellulosic biomass over a range of combined severity factors. *Bioresource technology*, *102*(10), 5884-5890.

[218] Arent DJ, Green P, Abdullah Z, Barnes T, Bauer S, Bernstein A, Berry D, Berry J, Burrell T, Carpenter B, Cochran J. Challenges and opportunities in decarbonizing the US energy system. Renewable and Sustainable Energy Reviews. 2022 Nov 1;169:112939.

[219] Lund, H. (2024). *Renewable energy systems: a smart energy systems approach to the choice and modeling of fully decarbonized societies*. Elsevier.

[220] Papadis, E., & Tsatsaronis, G. (2020). Challenges in the decarbonization of the energy sector. *Energy*, *205*, 118025.

[221] Abedin, A. H., & Rosen, M. A. (2011). A critical review of thermochemical energy storage systems. *The open renewable energy journal*, *4*(1), 42-46.

[222] Sarbu, I., & Sebarchievici, C. (2018). A comprehensive review of thermal energy storage. *Sustainability*, *10*(1), 191.

[223] Jouhara, H., Żabnieńska-Góra, A., Khordehgah, N., Ahmad, D., & Lipinski, T. (2020). Latent thermal energy storage technologies and applications: A review. *International Journal of Thermofluids*, *5*, 100039.

[224] Fernández, A., Martínez, M., Segarra, M., Martorell, I., & Cabeza, L. F. (2010). Selection of materials with potential in sensible thermal energy storage. *Solar energy materials and solar cells*, *94*(10), 1723-1729.

[225] Chen, X., Zhang, Z., Qi, C., Ling, X., & Peng, H. (2018). State of the art on the high-temperature thermochemical energy storage systems. *Energy Conversion and Management*, *177*, 792-815.

[226] Airò Farulla, G., Cellura, M., Guarino, F., & Ferraro, M. (2020). A review of thermochemical energy storage systems for power grid support. *Applied Sciences*, *10*(9), 3142.

[227] Lin, J., Zhao, Q., Huang, H., Mao, H., Liu, Y., & Xiao, Y. (2021). Applications of low-temperature thermochemical energy storage systems for salt hydrates based on material classification: A review. *Solar Energy*, *214*, 149-178.

[228] Wells, A. F. (1954). The crystal structures of salt hydrates and complex halides. *Quarterly Reviews, Chemical Society*, *8*(4), 380-403.

[229] Purohit, B. K., & Sistla, V. S. (2021). Inorganic salt hydrate for thermal energy storage application: A review. *Energy Storage*, *3*(2), e212.

[230] Balasubramanian, G., Ghommem, M., Hajj, M. R., Wong, W. P., Tomlin, J. A., & Puri, I. K. (2010). Modeling of thermochemical energy storage by salt hydrates. *International Journal of Heat and Mass Transfer*, *53*(25-26), 5700-5706.

[231] Blake, D., Gladen, A., & Bajwa, D. (2025). Salt hydrate bio-composites for thermal energy storage: A concise review. *Journal of Energy Storage*, *133*, 117874.

[232] Trausel, F., De Jong, A. J., & Cuypers, R. (2014). A review on the properties of salt hydrates for thermochemical storage. *Energy Procedia*, *48*, 447-452.

[233] Kiyabu, S., Girard, P., & Siegel, D. J. (2022). Discovery of salt hydrates for thermal energy storage. *Journal of the American Chemical Society*, *144*(47), 21617-21627.

[234] Spietz, T., Fryza, R., Lasek, J., & Zuwała, J. (2025). Thermochemical Energy Storage Based on Salt Hydrates: A Comprehensive Review. *Energies*, *18*(10), 2643.

[235] Sögütoglu, L. C., Birkelbach, F., Werner, A., Fischer, H., Huinink, H., & Adan, O. (2021). Hydration of salts as a two-step process: Water adsorption and hydrate formation. *Thermochimica Acta*, *695*, 178819.

[236] Linnow, K., Niermann, M., Bonatz, D., Posern, K., & Steiger, M. (2014). Experimental studies of the mechanism and kinetics of hydration reactions. *Energy procedia*, *48*, 394-404.

[237] Espinosa, R. M., Franke, L., & Deckelmann, G. (2008). Phase changes of salts in porous materials: Crystallization, hydration and deliquescence. *Construction and Building Materials*, *22*(8), 1758-1773.

[238] Yan, T. S., Li, T. X., Xu, J. X., & Chao, J. W. (2020). Understanding the transition process of phase change and dehydration reaction of salt hydrate for thermal energy storage. *Applied Thermal Engineering*, *166*, 114655.

[239] Aarts, J., van Ravensteijn, B., Fischer, H., Adan, O., & Huinink, H. (2023). Polymeric stabilization of salt hydrates for thermochemical energy storage. *Applied Energy*, *341*, 121068.

[240] Mehrabadi, A., & Farid, M. (2018). New salt hydrate composite for low-grade thermal energy storage. *Energy*, *164*, 194-203.

[241] Gordeeva, L. G., & Aristov, Y. I. (2012). Composites 'salt inside porous matrix'for adsorption heat transformation: a current state-of-the-art and new trends. *International Journal of Low-Carbon Technologies*, *7*(4), 288-302.

[242] Shojaeiarani, J.; Bajwa, D.S.; Chanda, S. (2021) "Cellulose nanocrystal based composites: A review" *Composites Part C: Open Access* **5** 100164

[243] Chu, Y.; Sun, Y.; Wu, W.; Xiao, H. (2020) "Dispersion Properties of Nanocellulose: A Review" *Carbohydrate Polymers* 250 116892

[244] Bai, L., Bossa, N., Qu, F., Winglee, J., Li, G., Sun, K., ... & Wiesner, M. R. (2017). Comparison of hydrophilicity and mechanical properties of nanocomposite membranes with cellulose nanocrystals and carbon nanotubes. *Environmental science & technology*, *51*(1), 253-262.

[245] Chu, S., & Majumdar, A. (2012). Opportunities and challenges for a sustainable energy future. *nature*, *488*(7411), 294-303.

[246] Li, M.; Wang, L.; Li, D.; Cheng, Y.; Adhikari, B. (2014) "Preparation and characterization of cellulose nanofibers from de-pectinated sugar beet pulp" *Carbohydrate Polymers* 102 pp. 136-143

[247] Hietala, M.; Sain, S.; Oksman, K. (2017) "Highly redispersible sugar beet nanofibers as reinforcement in bionanocomposites" *Cellulose* **24** pp. 2177-2189

[248] Vanderfleet, O. M., Reid, M. S., Bras, J., Heux, L., Godoy-Vargas, J., Panga, M. K., & Cranston, E. D. (2019). Insight into thermal stability of cellulose nanocrystals from new hydrolysis methods with acid blends. *Cellulose*, *26*(1), 507-528.

[249] Amin, K. N. M., Hosseinmardi, A., Martin, D. J., & Annamalai, P. K. (2022). A mixed acid methodology to produce thermally stable cellulose nanocrystal at high yield using phosphoric acid. *Journal of Bioresources and Bioproducts*, *7*(2), 99-108.

[250] Sluiter, A., Sluiter, J., & Wolfrum, E. J. (2013). Methods for biomass compositional analysis.

[251] Barra, I., Khiari, L., Haefele, S. M., Sakrabani, R., & Kebede, F. (2021). Optimizing setup of scan number in FTIR spectroscopy using the moment distance index and PLS regression: application to soil spectroscopy. *Scientific Reports*, *11*(1), 13358.

[252] Fischer, S., Thümmler, K., Pfeiffer, K., Liebert, T., & Heinze, T. (2002). Evaluation of molten inorganic salt hydrates as reaction medium for the derivatization of cellulose. *Cellulose*, *9*(3), 293-300.

[253] Zbair, M., & Bennici, S. (2021). Survey summary on salts hydrates and composites used in thermochemical sorption heat storage: a review. *Energies*, *14*(11), 3105

[254] Shin, J., Morrell, M. R., Barbosa, E., Menon, A. K., & McDowell, M. T. (2025). Investigating structural and morphological transformations of strontium chloride for thermochemical energy storage. *Journal of Materials Chemistry A*.

[255] Trailokya, A., Srivastava, A., Bhole, M., & Zalte, N. (2017). Calcium and calcium salts. *Journal of the Association of Physicians of India*, *65*(1), 1-2

[256] Yang, H., Wang, C., Tong, L., Yin, S., Wang, L., & Ding, Y. (2023). Salt hydrate adsorption material-based thermochemical energy storage for space heating application: A review. *Energies*, *16*(6), 2875

[257] Trache, D., Hussin, M. H., Haafiz, M. M., & Thakur, V. K. (2017). Recent progress in cellulose nanocrystals: sources and production. *Nanoscale*, *9*(5), 1763-1786

[258] Kumar, N.; & Banerjee, D. (2019). Thermal cycling of calcium chloride hexahydrate with strontium chloride as a phase change material for latent heat thermal energy storage applications in a nondifferential scanning calorimeter set-up. *Journal of Thermal Science and Engineering Applications*, *11*(5), 051014.

[259] Kenney, C. N. (1975). Molten salt catalysis of gas reactions. *Catalysis Reviews Science and Engineering*, *11*(1), 197-224.

[260] Phan-Xuan, T., Thuresson, A., Skepö, M., Labrador, A., Bordes, R., & Matic, A. (2016). Aggregation behavior of aqueous cellulose nanocrystals: the effect of inorganic salts. *Cellulose*, *23*(6), 3653-3663

[261] Pandey, R., Pourhashem, G., & Gladen, A. C. (2024). Screening of salt hydrates and cellulose nanocrystal composites for thermochemical energy storage using life cycle assessment. *Sustainable Materials and Technologies*, *40*, e00889.

[262] Rudie, A. (2017). Commercialization of cellulose nanofibril (CNF) and cellulose nanocrystal (CNC): pathway and challenges. *Handbook of nanocellulose and cellulose nanocomposites*, *2*, 761-797.

[263] Ciolacu, D., Ciolacu, F., & Popa, V. I. (2011). Amorphous cellulose—structure and characterization. *Cellulose chemistry and technology*, *45*(1), 13.

[264] Li, Z.; Deng, L.; Kinloch, I.A.; Young, R.J. (2023) Raman spectroscopy of carbon materials and their composites: Graphene, nanotubes and fibres *Progress in Mater. Sci.* 135. 101089

[265] Diana, E., Chierotti, M. R., Marchese, E. M., Croce, G., Milanesio, M., & Stanghellini, P. L. (2012). Blue and red shift hydrogen bonds in crystalline cobaltocinium complexes. *New Journal of Chemistry*, *36*(4), 1099-1107.

[266] Adams, D.M.; Trumble, W.R. (1974) Single-crystal Raman spectrum of strontium dichloride hexahydrate and some related materials *J. Chem. Soc., Faraday Trans. 2*, 70, 1967-1977

[267] Hetmanczyk, J.; Hetmanczyk, L.; Migdal-Mikuli, A.; Mikuli, E.; Florek-Wojciechowska, M.; Haranczyk, H. (2014) Vibrations and reorientations of H_2O molecules in $[Sr(H_2O)_6]Cl_2$ studied by Raman light scattering, incoherent inelastic neutron scattering and proton magnetic resonance. *Spectrochimica Acta Part A: Mol. And Biomol. Spec.*, 124, 429-440

[268] Forst, M., Mankowsky, R., & Cavalleri, A. (2015). Mode-selective control of the crystal lattice. *Accounts of chemical research*, *48*(2), 380-387.

[269] Hong, J.; Heo, S.J.; Singh, P. (2021) Water mediated growth of oriented single crystalline $SrCO_3$ nanorod arrays on strontium compounds. *Sci. Rep.*, 11, 3368

[270] Guerrero-Perez, M.O.; Patience, G.S. (2019) Experimental methods in chemical engineering: Fourier transform infrared spectroscopy–FTIR. *The Canadian J. of Chem. Eng.* 98 (1) pp. 25-33

[271] Berthomieu, C., & Hienerwadel, R. (2009). Fourier transform infrared (FTIR) spectroscopy. *Photosynthesis research*, *101*(2), 157-170

[272] Lutz, H. D., Pobitschka, W., Christian, H., & Becker, R. A. (1979). Lattice vibration spectra. XXII—infrared and Raman spectra of strontium chloride dihydrate, SrCl2· 2H2O and SrCl2· 2 (H, D) 2O. *Journal of Raman Spectroscopy*, *8*(4), 189-194

[273] Buczek, A.; Rzepiela, K.; Kupka, T.; & Broda, M. A. (2025). Impact of OH$\cdots\pi$ Hydrogen Bond on IR and NMR Parameters of Cannabidiol: Theoretical and Experimental Study. *Molecules*, *30*(12), 2591.

[274] Mizuno, K.; Miyashita, Y.; Shindo, Y.; & Ogawa, H. (1995). NMR and FT-IR studies of hydrogen bonds in ethanol-water mixtures. *The Journal of Physical Chemistry*, *99*(10), 3225-3228.

[275] Bridelli, M. G. (2017). Fourier transform infrared spectroscopy in the study of hydrated biological macromolecules. *Fourier Transforms-High-Tech Application and Current Trends*, 191-213.

[276] Badger, R. M., & Bauer, S. H. (1937). Spectroscopic studies of the hydrogen bond. II. The shift of the O–H vibrational frequency in the formation of the hydrogen bond. *The Journal of Chemical Physics*, *5*(11), 839-851

[277] Cihan, E., Berent, H. K., Demir, H., & Öztop, H. F. (2023). Entropy analysis and thermal energy storage performance of PCM in honeycomb structure: Effects of materials and dimensions. *Thermal Science and Engineering Progress*, *38*, 101668

[278] Range, S.; Bernardes, C.E.S.; Simoes, R.G.; Epple, M.; Minas da Piedade, M.E. (2015) "Size Matters: An Experimental and Computational Study of the Influence of Particle Size on the Lattice Energy of NaCl" *J. Phys. Chem. C* **119** (8) pp.4387-4396

[279] Druske, M. M., Fopah-Lele, A., Korhammer, K., Rammelberg, H. U., Wegscheider, N., Ruck, W., & Schmidt, T. (2014). Developed materials for thermal energy storage: synthesis and characterization. *Energy procedia*, *61*, 96-99

[280] Krishna, R. (2012). Diffusion in porous crystalline materials. *Chemical Society Reviews*, *41*(8), 3099-3118

[281] Østergaard, K. K., Anderson, R., Llamedo, M., & Tohidi, B. (2002). Hydrate phase equilibria in porous media: effect of pore size and salinity. *Terra Nova*, *14*(5), 307-312

[282] Freyer, D., & Voigt, W. (2003). Crystallization and phase stability of CaSO4 and CaSO4–based salts. *Monatshefte für Chemie/Chemical Monthly*, *134*(5), 693-719

[283] Sogutoglu, L. C., Steiger, M., Houben, J., Biemans, D., Fischer, H. R., Donkers, P., ... & Adan, O. C. (2019). Understanding the hydration process of salts: the impact of a nucleation barrier. *Crystal Growth & Design*, *19*(4), 2279-2288

[284] Mauer, L. J., & Taylor, L. S. (2010). Water-solids interactions: deliquescence. *Annual review of food science and technology*, *1*(1), 41-63

[285] DeForest, N., Mendes, G., Stadler, M., Feng, W., Lai, J., & Marnay, C. (2014). Optimal deployment of thermal energy storage under diverse economic and climate conditions. *Applied energy*, *119*, 488-496

[286] Aarts, J., Fischer, H., Adan, O., & Huinink, H. (2024). Impact of cycling on the performance of mm-sized salt hydrate particles. *Journal of Energy Storage*, *76*, 109806

[287] Aarts, J., de Jong, S., Cotti, M., Donkers, P., Fischer, H., Adan, O., & Huinink, H. (2022). Diffusion limited hydration kinetics of millimeter sized salt hydrate particles for thermochemical heat storage. *Journal of energy storage*, *47*, 103554

[288] Hobson, R. D. (2019). Surface roughness in topography: quantitative approach. In *Spatial analysis in geomorphology* (pp. 221-246). Routledge.

[289] Zeng, Z., Ma, H., Yang, C., Zhao, K., Liang, X., Li, H., & Zheng, Z. (2024). Self-healing behaviors of damaged rock salt under humidity cycling. *International Journal of Rock Mechanics and Mining Sciences*, *174*, 105636

[290] Shin, J., Morrell, M. R., Barbosa, E., Menon, A. K., & McDowell, M. T. (2025). Investigating structural and morphological transformations of strontium chloride for thermochemical energy storage. *Journal of Materials Chemistry A*.

[291] Aramfard, M., Kaynan, O., Hosseini, E., Zakertabrizi, M., Pérez, L. M., & Asadi, A. (2022). Aqueous dispersion of carbon nanomaterials with cellulose nanocrystals: an investigation of molecular interactions. *Small*, *18*(37), 2202216.

[292] Ren, Z., Guo, R., Zhou, X., Bi, H., Jia, X., Xu, M., ... & Huang, Z. (2021). Effect of amorphous cellulose on the deformation behavior of cellulose composites: molecular dynamics simulation. *Rsc Advances*, *11*(33), 19967-19977

[293] Lefrant, S., Baibarac, M., & Baltog, I. (2009). Raman and FTIR spectroscopy as valuable tools for the characterization of polymer and carbon nanotube based composites. *Journal of Materials Chemistry*, *19*(32), 5690-5704

[294] Hamilton, A., & Menzies, R. I. (2010). Raman spectra of mirabilite, Na2SO4· 10H2O and the rediscovered metastable heptahydrate, Na2SO4· 7H2O. *Journal of Raman Spectroscopy*, *41*(9), 1014-1020

[295] Baumgartner, M., & Bakker, R. J. (2010). Raman spectra of ice and salt hydrates in synthetic fluid inclusions. *Chemical Geology*, *275*(1-2), 58-66

[296] Chaban, G. M., Huo, W. M., & Lee, T. J. (2002). Theoretical study of infrared and Raman spectra of hydrated magnesium sulfate salts. *The Journal of chemical physics*, *117*(6), 2532-2537

[297] Berets, S., & Christenson, J. (2015). Polarization in FTIR ATR.

[298] Eneh, C.I.; Bolen, M.J.; Suarez-Martinez, P.C.; Bachmann, A.L.; Zimudzi, T.J., Hickner, M.A.; Batys, P.; Sammalkorpi, M.; & Lutkenhaus, J.L. (2020). Fourier transform infrared spectroscopy investigation of water microenvironments in polyelectrolyte multilayers at varying temperatures. *Soft Matter*, *16*(9), 2291-2300.

[299] Max, J. J.; & Chapados, C. (2001). IR spectroscopy of aqueous alkali halide solutions: pure salt-solvated water spectra and hydration numbers. *The Journal of Chemical Physics*, *115*(6), 2664-2675.

[300] Bai, L., Bossa, N., Qu, F., Winglee, J., Li, G., Sun, K., Liang, H. & Wiesner, M.R. (2017). Comparison of hydrophilicity and mechanical properties of nanocomposite membranes with cellulose nanocrystals and carbon nanotubes. *Environmental science & technology*, *51*(1), 253-262.

[301] Prathapan, R., Thapa, R., Garnier, G., & Tabor, R. F. (2016). Modulating the zeta potential of cellulose nanocrystals using salts and surfactants. *Colloids and Surfaces A: Physicochemical and Engineering Aspects*, *509*, 11-18

[302] Phan-Xuan, T., Thuresson, A., Skepö, M., Labrador, A., Bordes, R., & Matic, A. (2016). Aggregation behavior of aqueous cellulose nanocrystals: the effect of inorganic salts. *Cellulose*, *23*(6), 3653-3663

[303] Sim, K., Lee, J., Lee, H., & Youn, H. J. (2015). Flocculation behavior of cellulose nanofibrils under different salt conditions and its impact on network strength and dewatering ability. *Cellulose*, *22*(6), 3689-3700

[304] Zhong, L., Fu, S., Peng, X., Zhan, H., & Sun, R. (2012). Colloidal stability of negatively charged cellulose nanocrystalline in aqueous systems. *Carbohydrate polymers*, *90*(1), 644-649

[305] Tatsumi, D., Ishioka, S., & Matsumoto, T. (1999). Effect of particle and salt concentrations on the rheological properties of cellulose fibrous suspensions. *Nihon Reoroji Gakkaishi*, *27*(4), 243-248

[306] Hu, F., Lin, N., Chang, P. R., & Huang, J. (2015). Reinforcement and nucleation of acetylated cellulose nanocrystals in foamed polyester composites. *Carbohydrate polymers*, *129*, 208-215

[307] Yu, H. Y., Zhang, H., Song, M. L., Zhou, Y., Yao, J., & Ni, Q. Q. (2017). From cellulose nanospheres, nanorods to nanofibers: various aspect ratio induced nucleation/reinforcing effects on polylactic acid for robust-barrier food packaging. *ACS applied materials & interfaces*, *9*(50), 43920-43938

[308] Leff, H. S. (1996). Thermodynamic entropy: The spreading and sharing of energy. *American Journal of Physics*, *64*(10), 1261-1271

[309] Yang, D., Peng, X. W., Zhong, L. X., Cao, X. F., Chen, W., & Sun, R. C. (2013). Effects of pretreatments on crystalline properties and morphology of cellulose nanocrystals. *Cellulose*, *20*(5), 2427-2437

[310] Arvidsson, R., Nguyen, D., & Svanström, M. (2015). Life cycle assessment of cellulose nanofibrils production by mechanical treatment and two different pretreatment processes. *Environmental science & technology*, *49*(11), 6881-6890

[311] Abbasi, A., Makhtoumi, Y., Wu, Y., & Chen, G. (2024). Characterization of cellulose nanocrystal extracted from household waste and its application for seed germination. *Carbohydrate Polymer Technologies and Applications*, *7*, 100409

[312] Xie, H., Du, H., Yang, X., & Si, C. (2018). Recent strategies in preparation of cellulose nanocrystals and cellulose nanofibrils derived from raw cellulose materials. *International Journal of Polymer Science*, *2018*(1), 7923068

[313] Benchikh, L., Ait Ferhat, Y., Guessoum, M., Merzouki, A., & Grohens, Y. (2025). Cellulose nanocrystals (CNC) from Diss plant: bleaching treatment effect. *International Journal of Materials Research*

[314] Chanda, S., & Bajwa, D. S. (2021). A review of current physical techniques for dispersion of cellulose nanomaterials in polymer matrices. *Reviews on Advanced Materials Science*, *60*(1), 325-341

APPENDICES

APPENDIX A

CHAPTER TWO

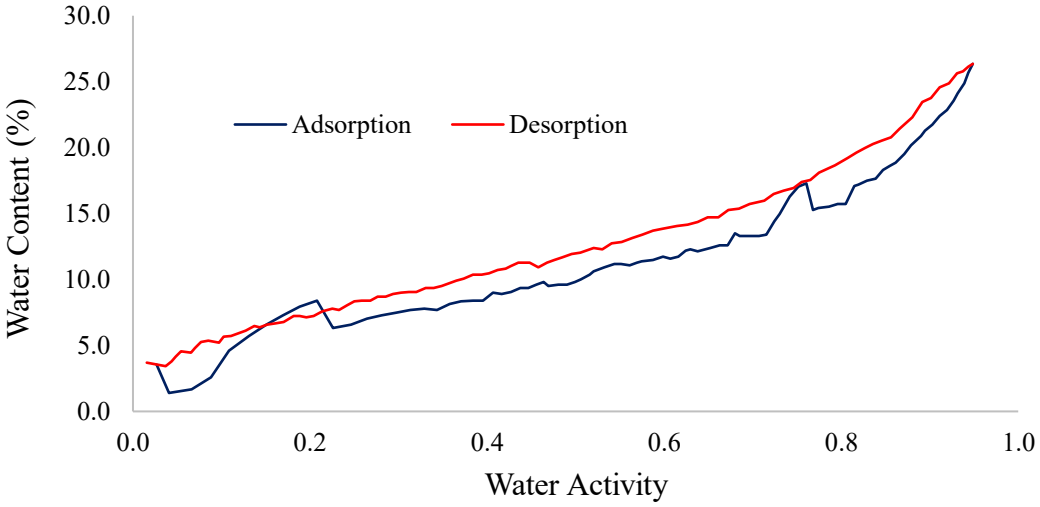

Figure A1. Raw data of 30°C treated CNC – water adsorption testing

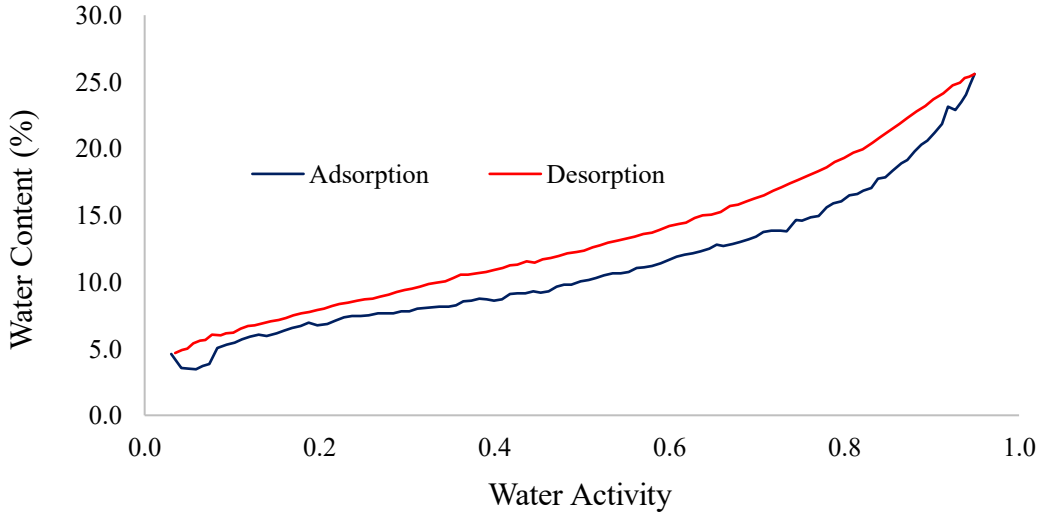

Figure A2. Raw data of 60°C treated CNC – water adsorption testing

APPENDIX B

CHAPTER FIVE

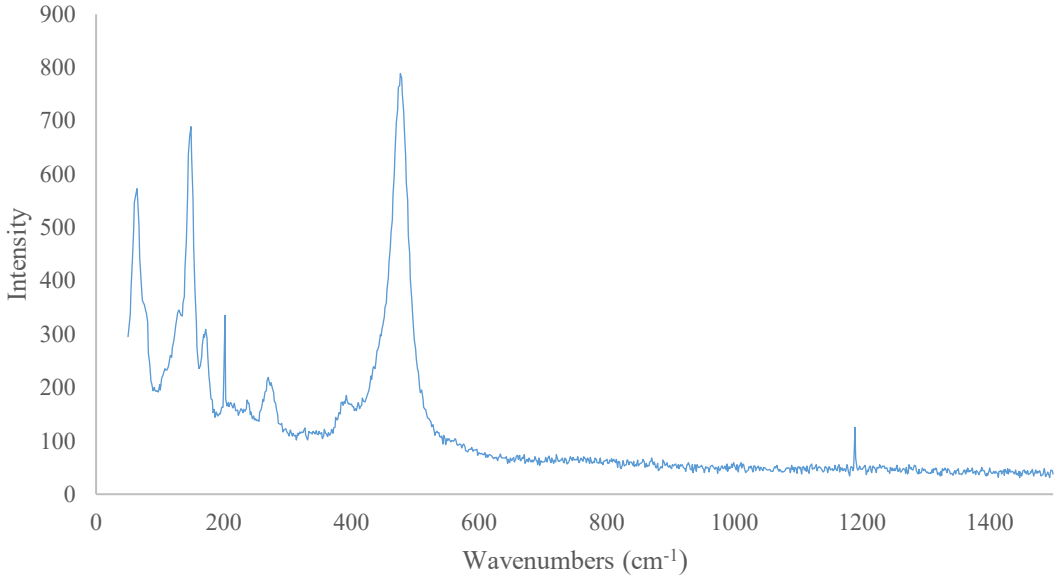

Figure B1. Raman spectrum of CNC control from 50 to 1500 cm^{-1} using 785nm excitation wavelength

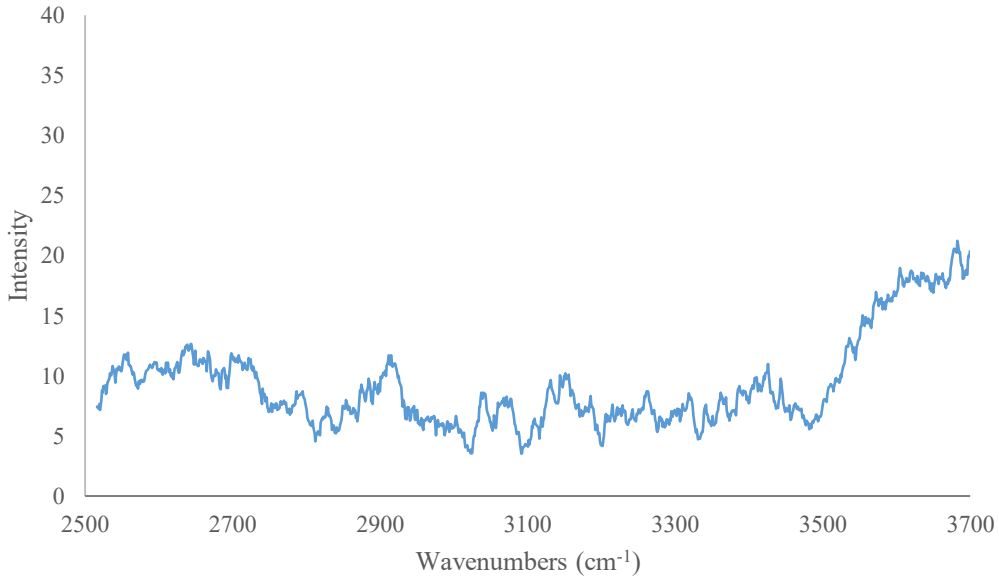

Figure B2. Raman spectrum of CNC control from 2500 to 3700 cm^{-1} using 785nm excitation wavelength

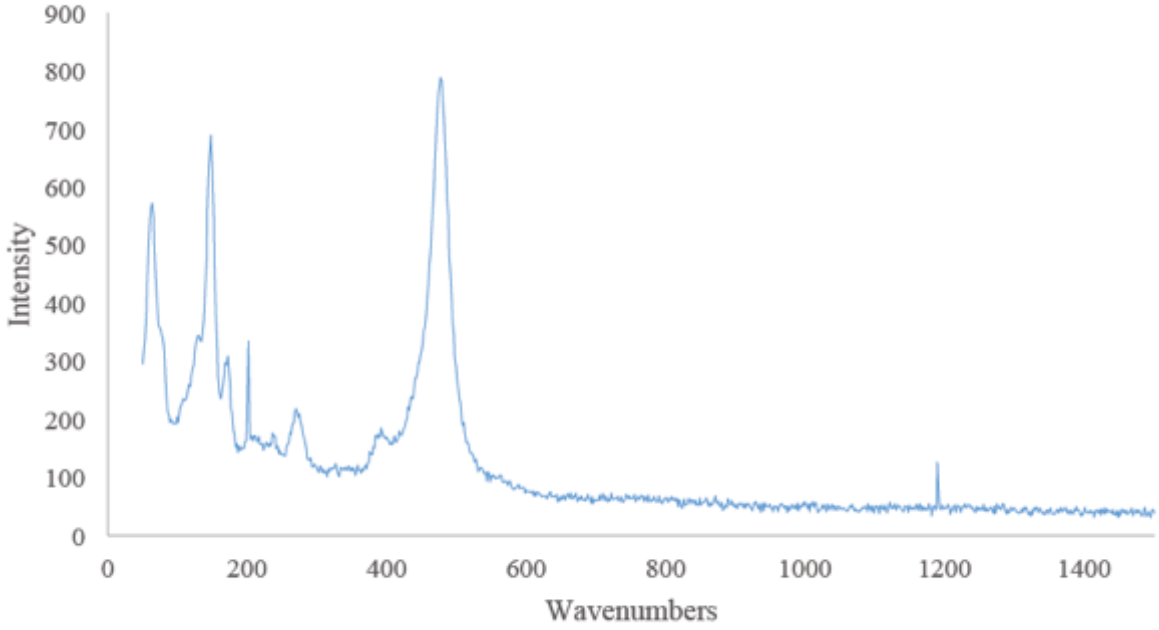

Figure B4. Raman spectrum of $SrCl_2$ control from 50 to 1500 cm^{-1} using 785nm excitation wavelength

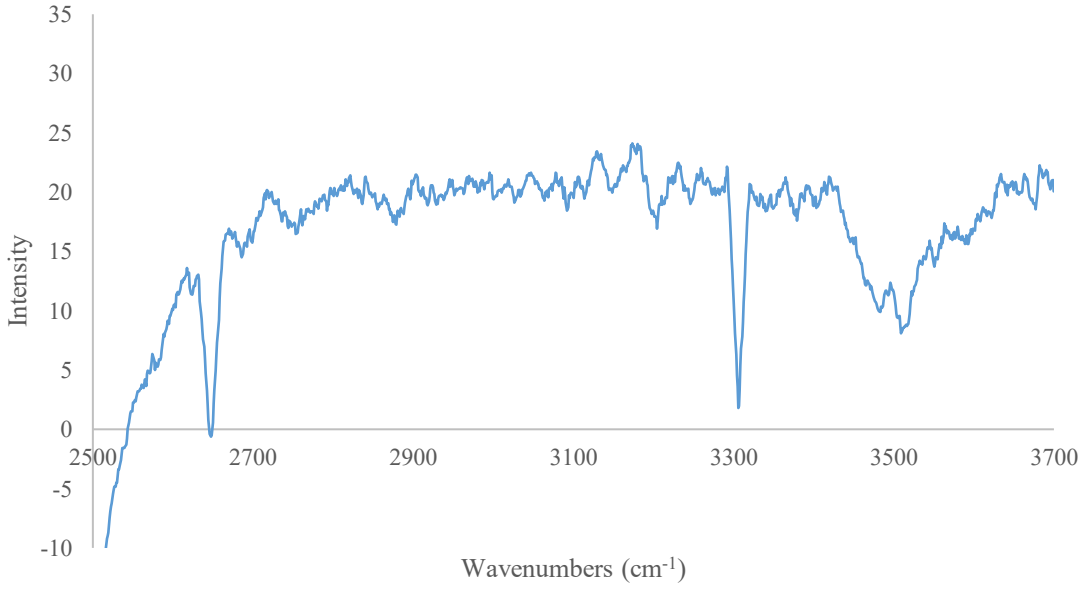

Figure B3. Raman spectrum of $SrCl_2$ control from 2500 to 3700 cm^{-1} using 785nm excitation wavelength

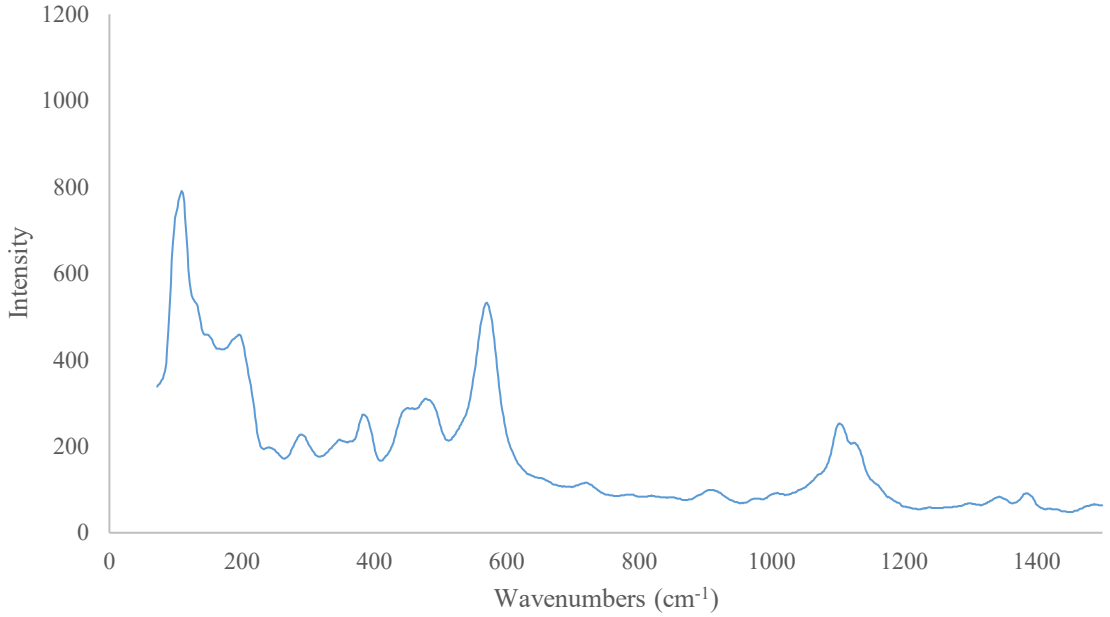

Figure B5. Raman spectrum of $SrCl_2$:CNC – 90:10 composite from 50 to 1500 cm^{-1} using 785nm excitation wavelength

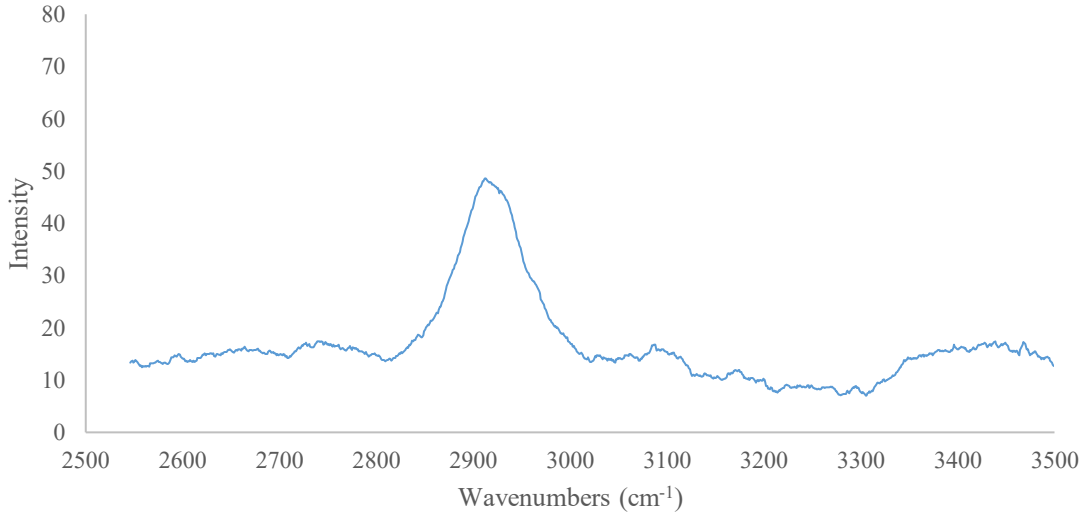

Figure B6. Raman spectrum of $SrCl_2$:CNC – 90:10 composite from 2500 to 3700 cm^{-1} using 785nm excitation wavelength

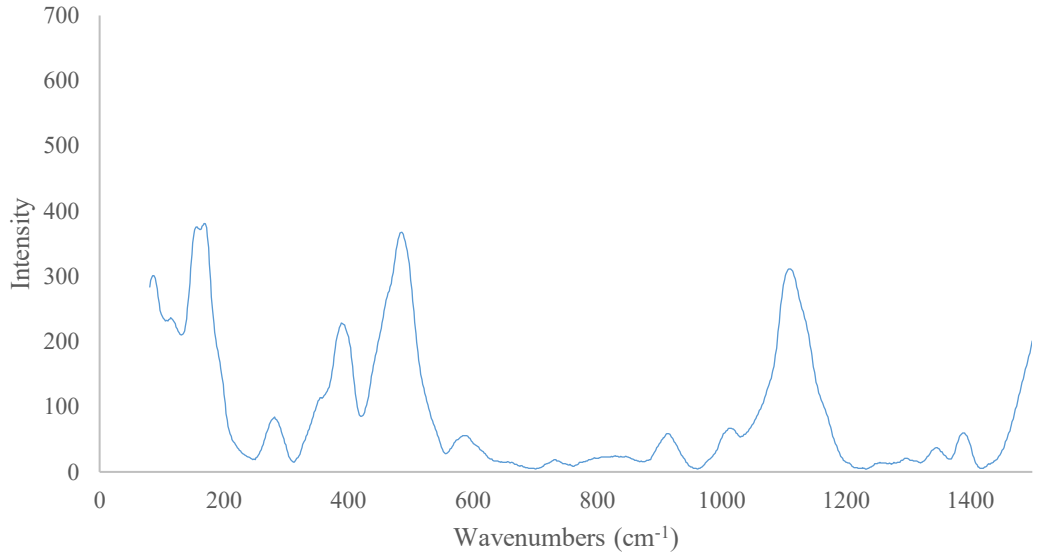

Figure B7. Raman spectrum of $SrCl_2$:CNC – 80:20 composite from 50 to 1500 cm^{-1}

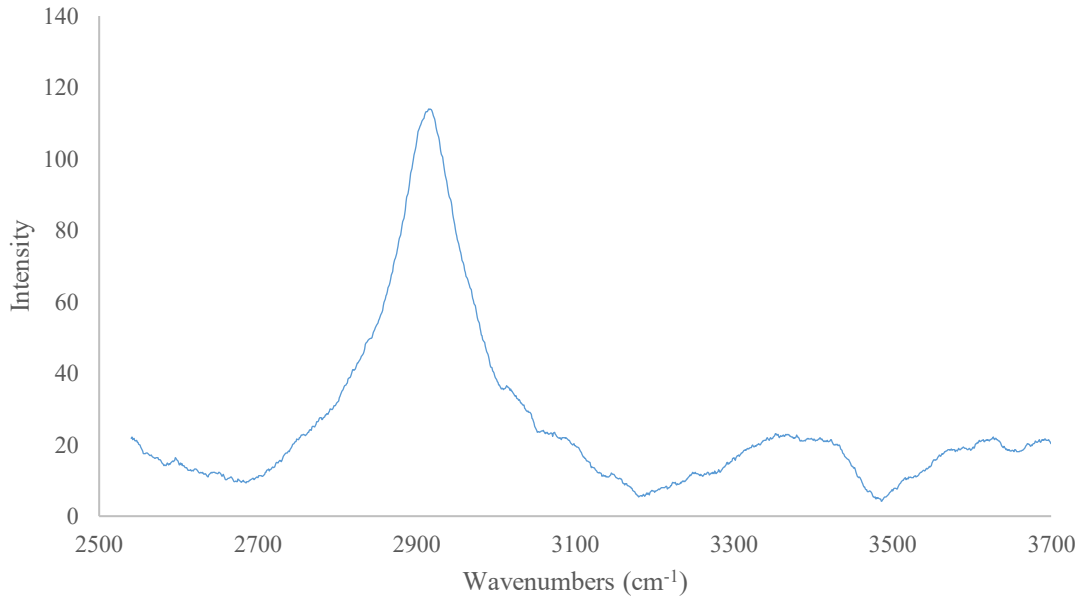

Figure B8. Raman spectrum of $SrCl_2$:CNC – 80:20 composite from 2500 to 3700 cm^{-1} using 785nm excitation wavelength

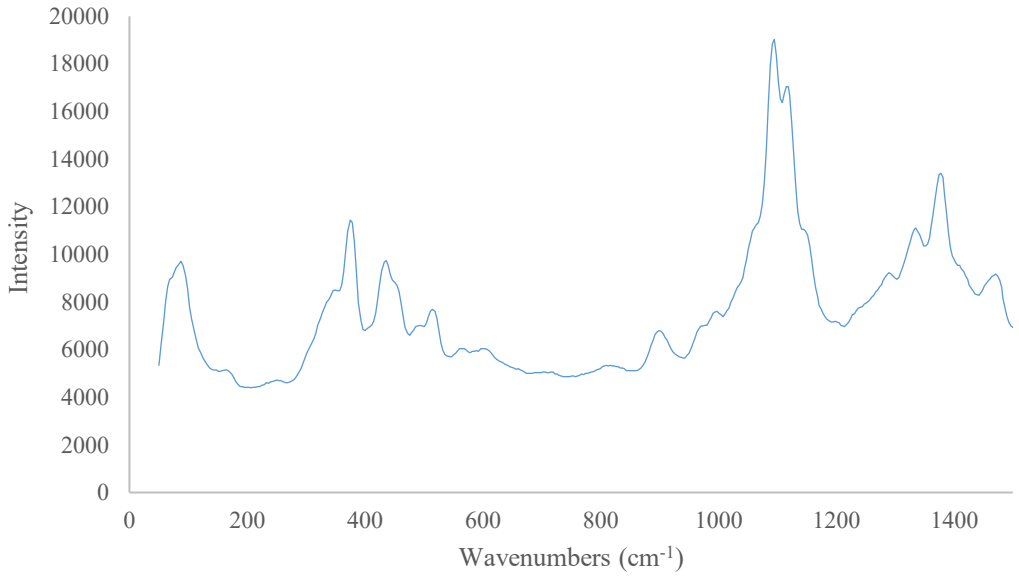

Figure B9. Raman spectrum of CNC control from 50 to 1500 cm^{-1} using 532nm excitation wavelength

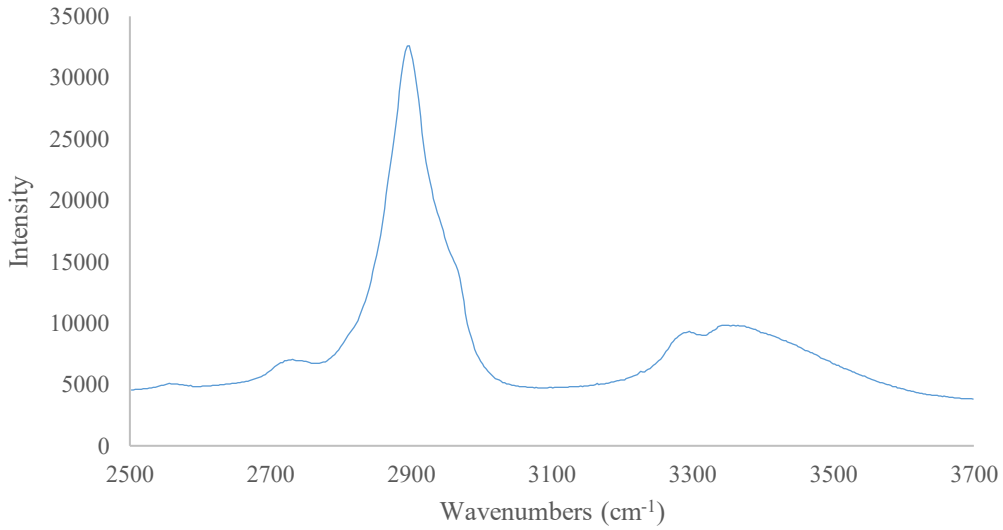

Figure B10. Raman spectrum of CNC control from 2500 to 3700 cm^{-1} using 532nm excitation wavelength

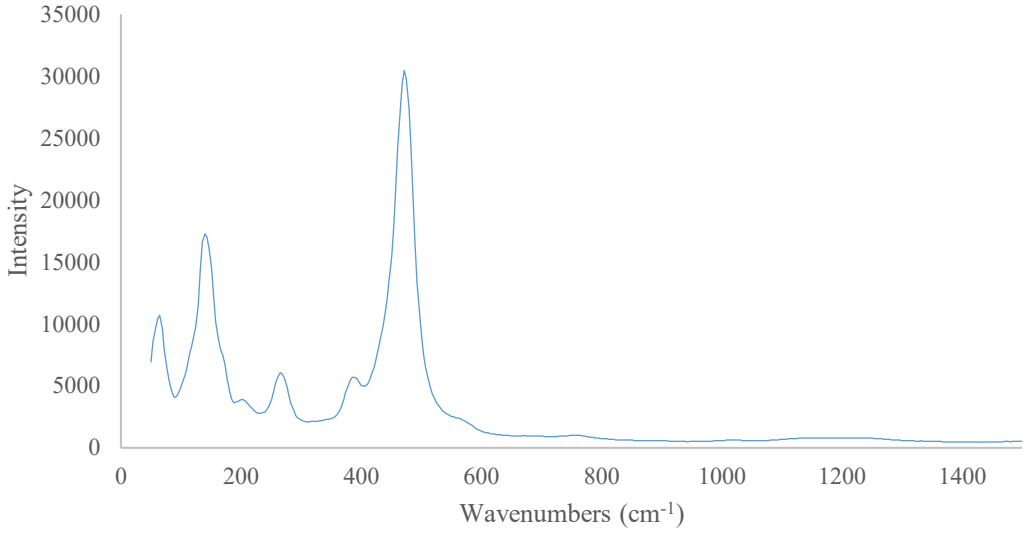

Figure B11. Raman spectrum of $SrCl_2$ control from 50 to 1500 cm^{-1} using 532nm excitation wavelength

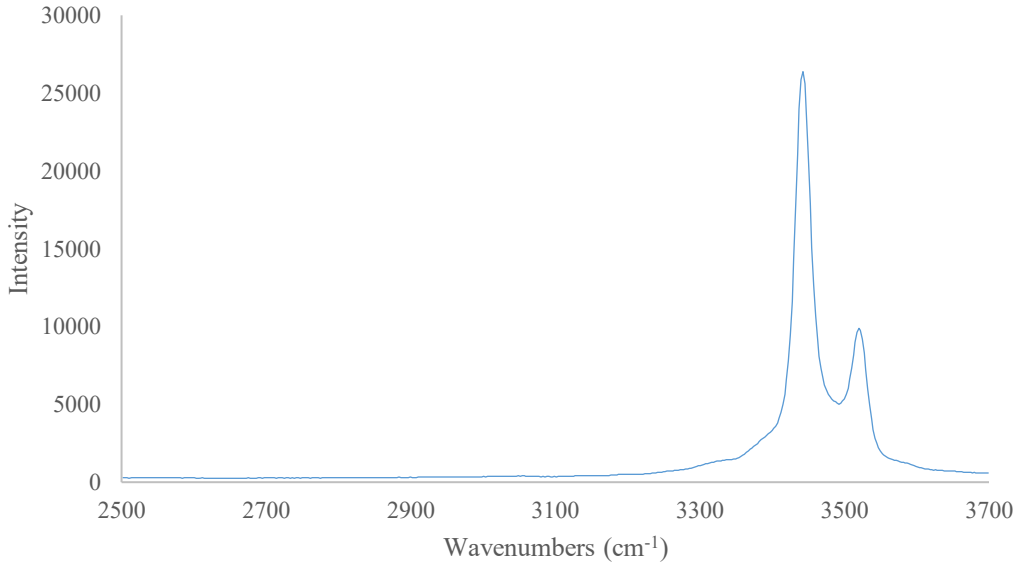

Figure B12. Raman spectrum of $SrCl_2$ control from 2500 to 3700 cm^{-1} using 532nm excitation wavelength

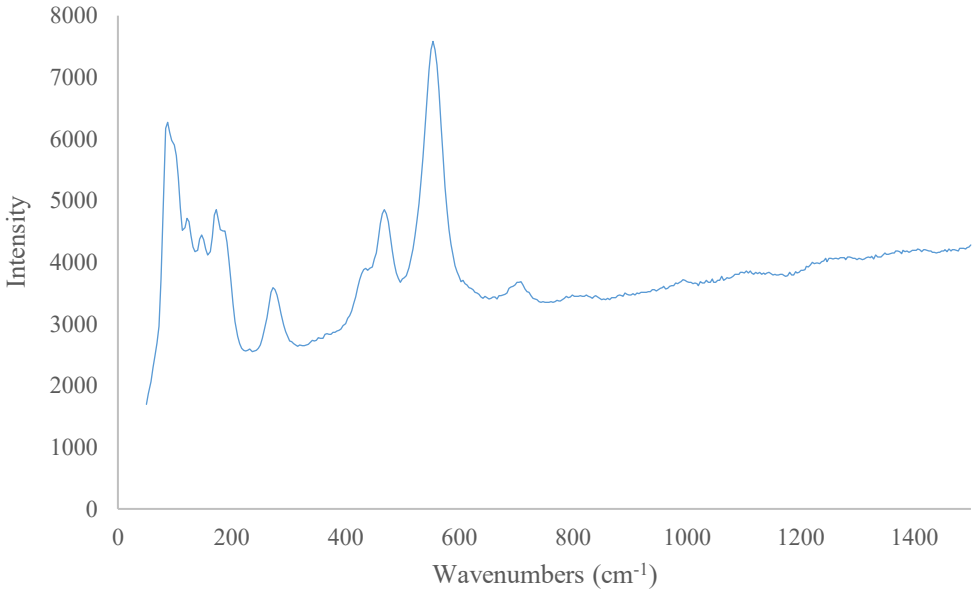

Figure B13. Raman spectrum of $SrCl_2$:CNC – 90:10 composite from 50 to 1500 cm^{-1} using 532nm excitation wavelength

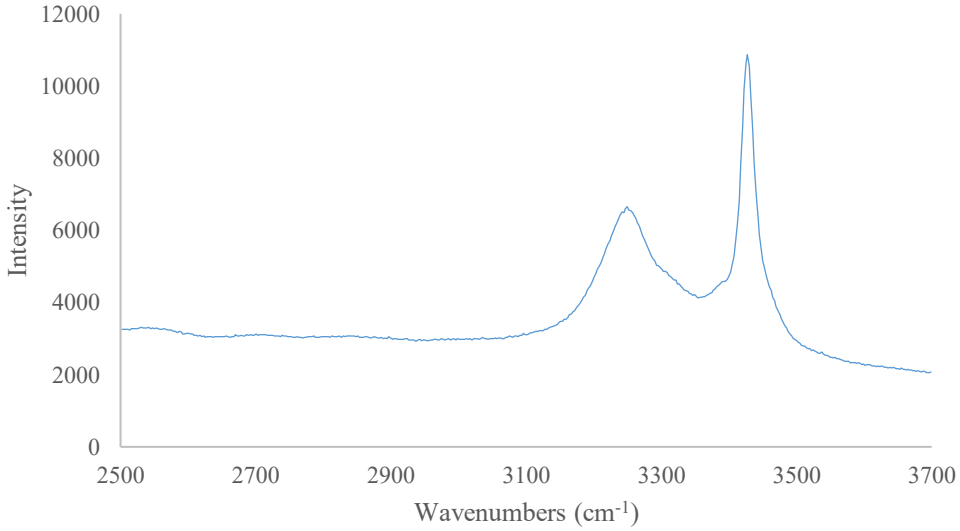

Figure B14. Raman spectrum of $SrCl_2$:CNC – 90:10 composite from 2500 to 3700 cm^{-1} using 532nm excitation wavelength

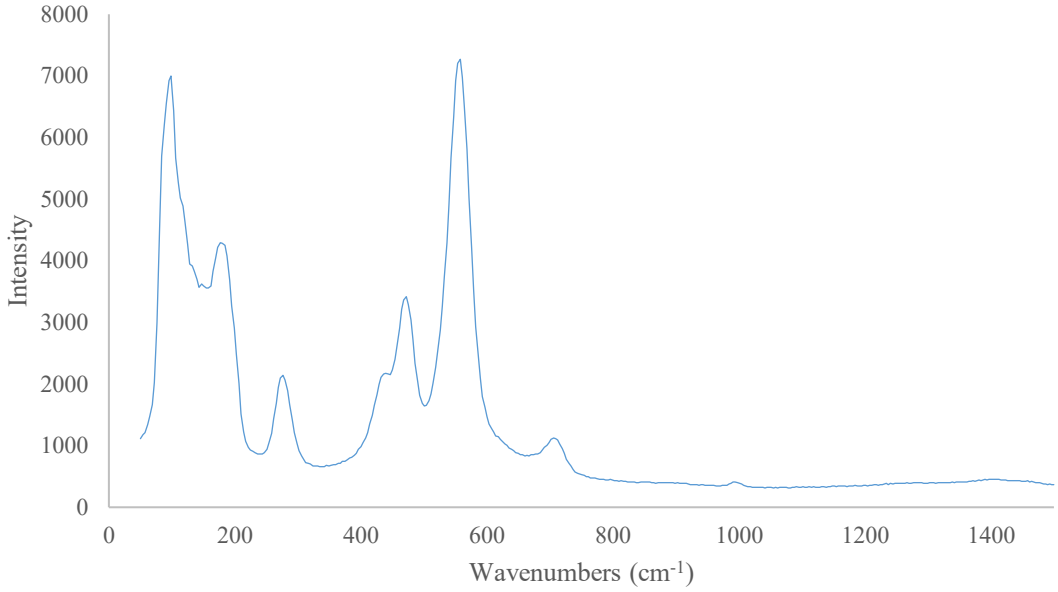

Figure B15. Raman spectrum of $SrCl_2$:CNC – 80:20 composite from 50 to 1500 cm^{-1} using 532nm excitation wavelength

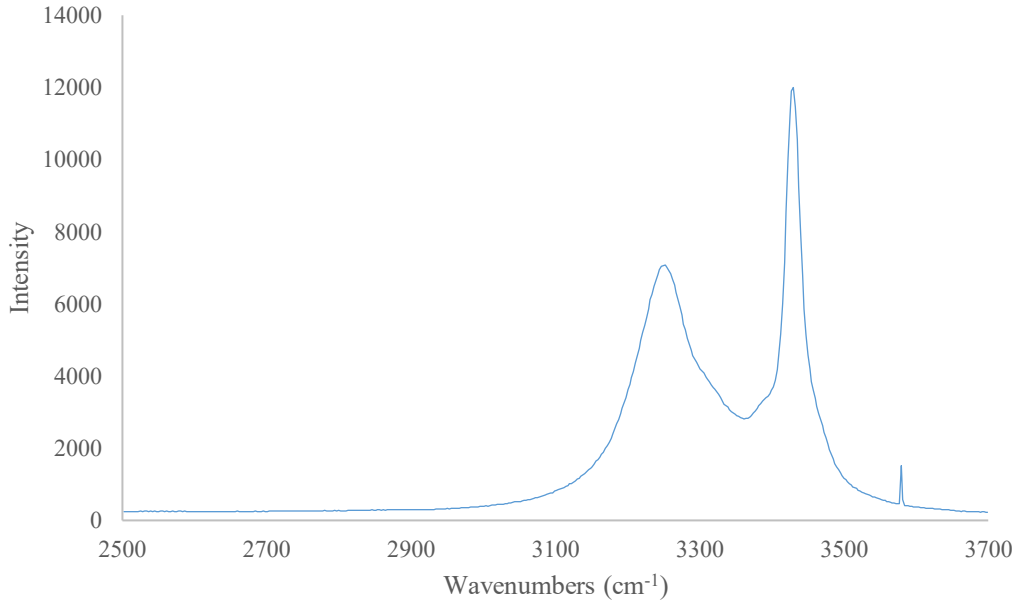

Figure B16. Raman spectrum of $SrCl_2$:CNC – 80:20 composite from 2500 to 3700 cm^{-1} using 532nm excitation wavelength

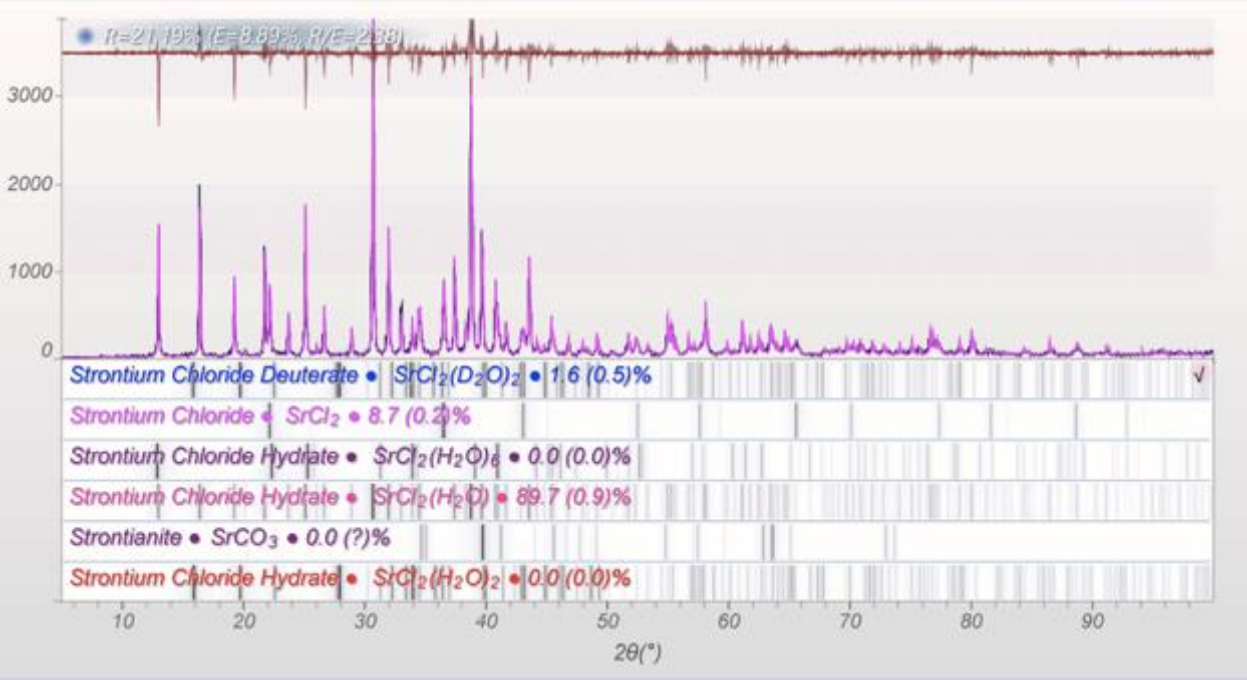

Figure B17. Rietveld refinement whole pattern fitting of dehydrated $SrCl_2$:CNC – 90:10 composite

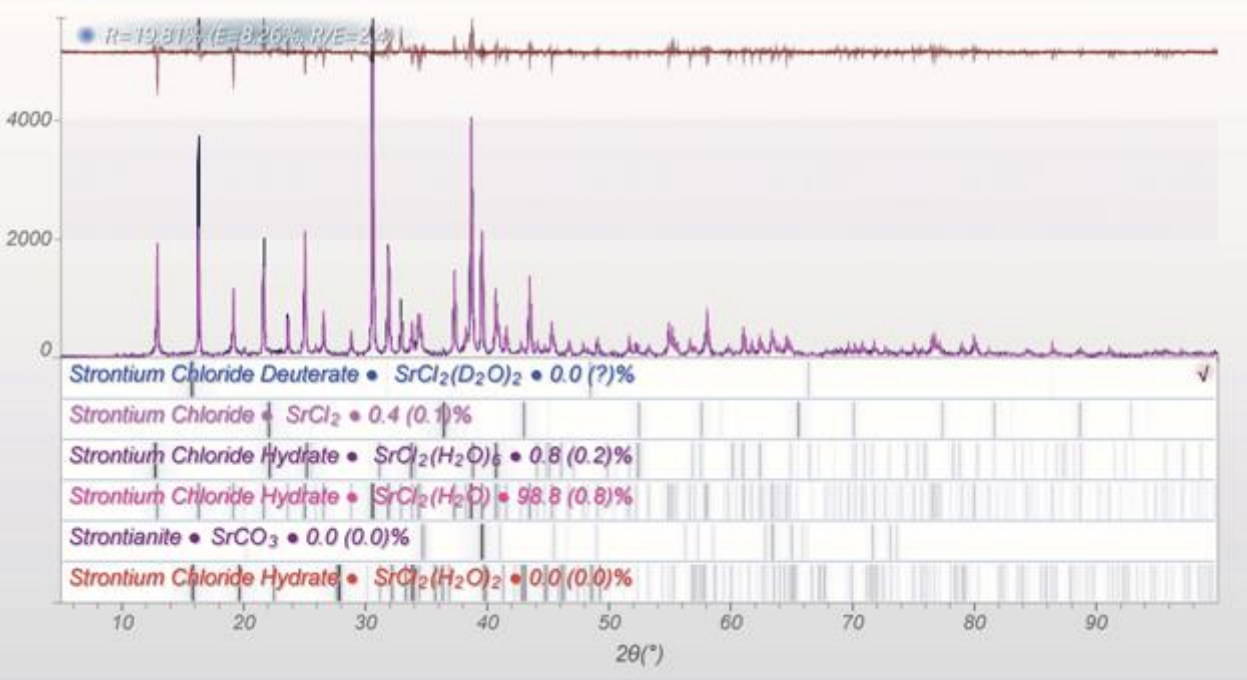

Figure B18. Rietveld refinement whole pattern fitting of dehydrated $SrCl_2$:CNC – 80:20 composite

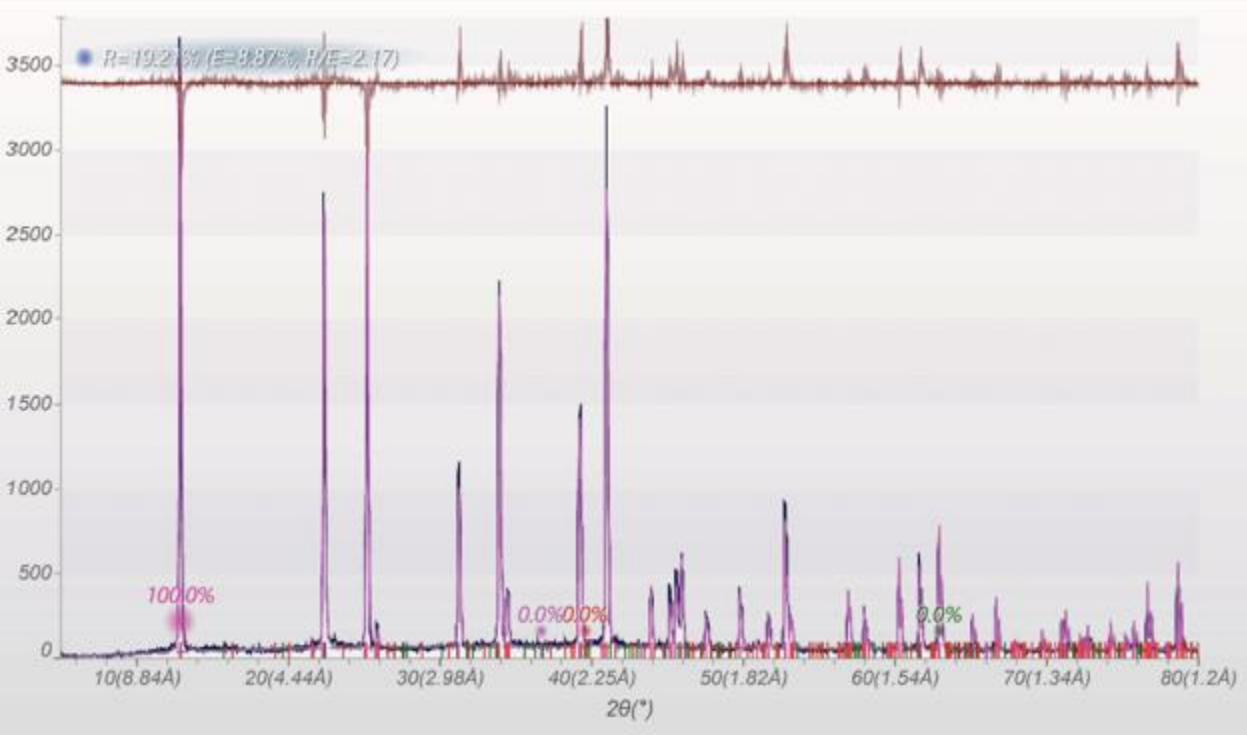

Figure B19. Rietveld refinement whole pattern fitting of hydrated $SrCl_2$:CNC – 90:10 composite

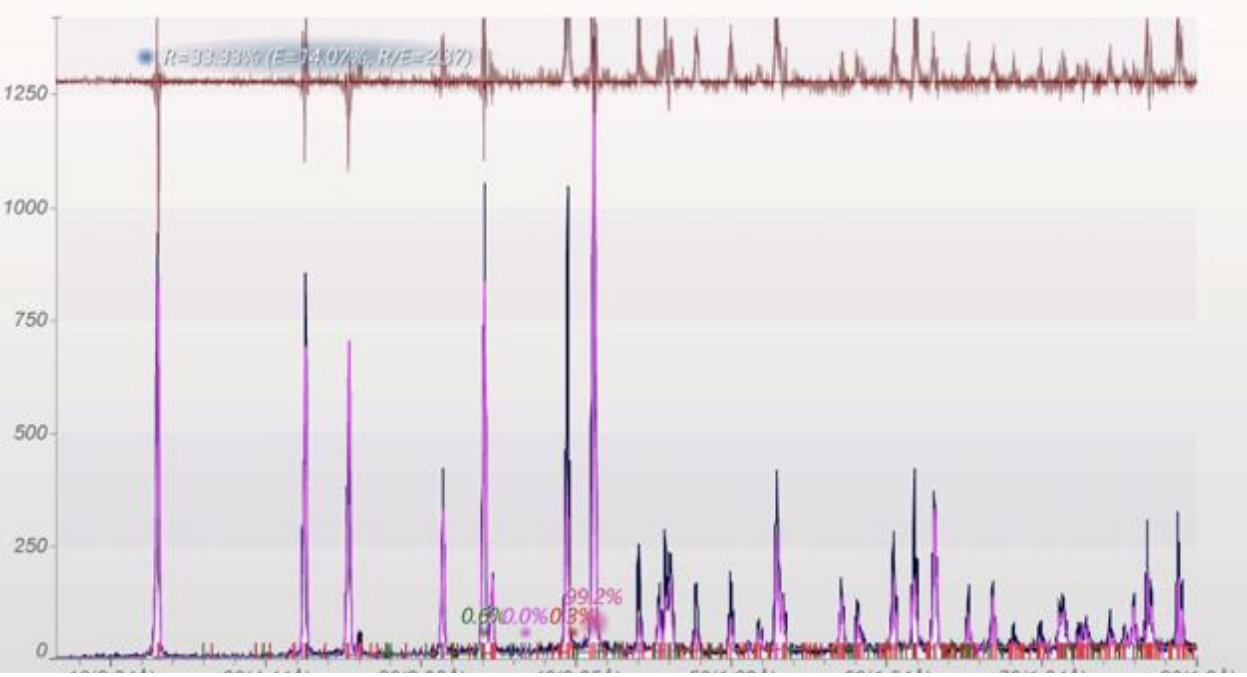

Figure B20. Rietveld refinement whole pattern fitting of hydrated $SrCl_2$ control salt

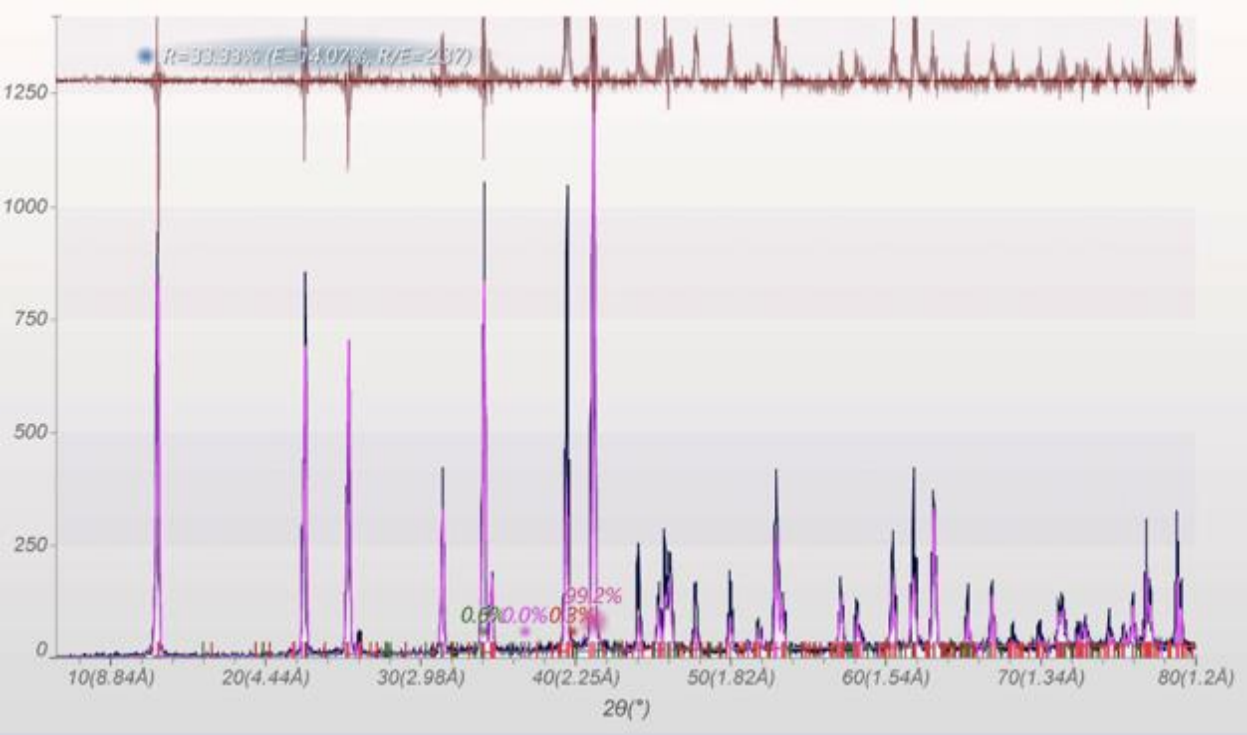

Figure B22. Rietveld refinement whole pattern fitting of dehydrated $SrCl_2$ control salt

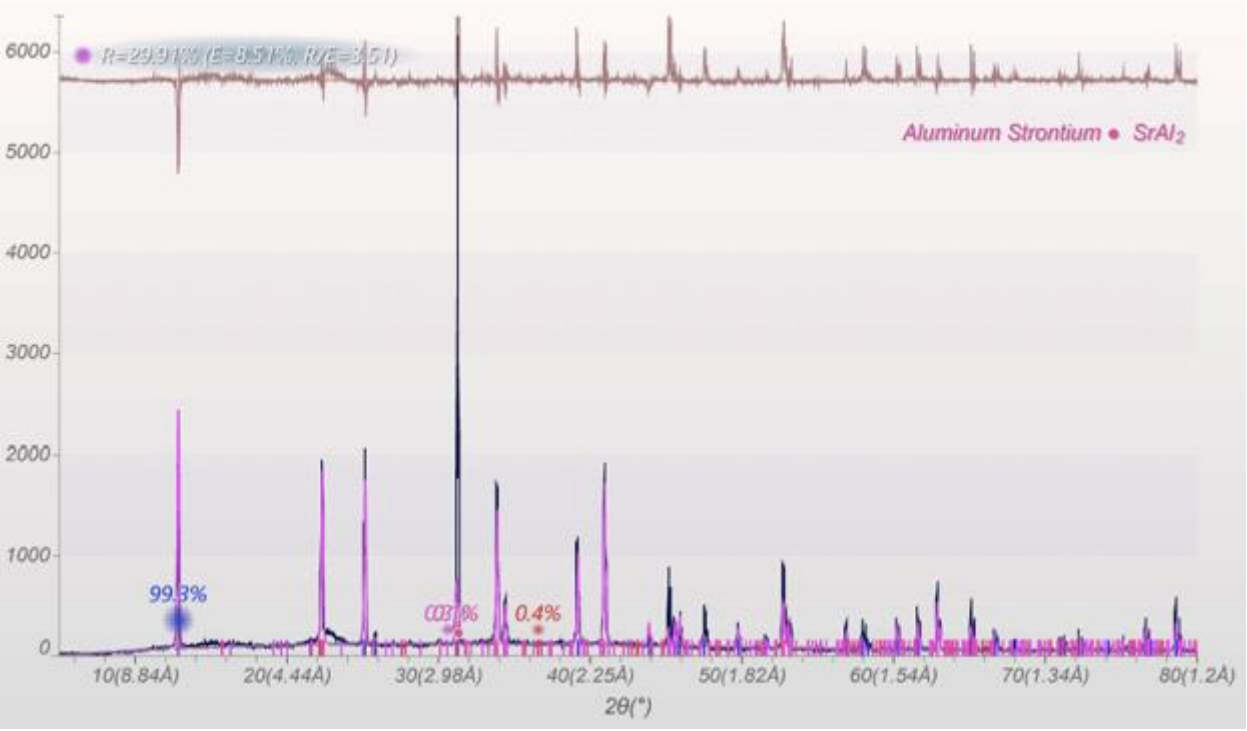

Figure B21. Rietveld refinement whole pattern fitting of hydrated $SrCl_2$:CNC – 80:20 composite

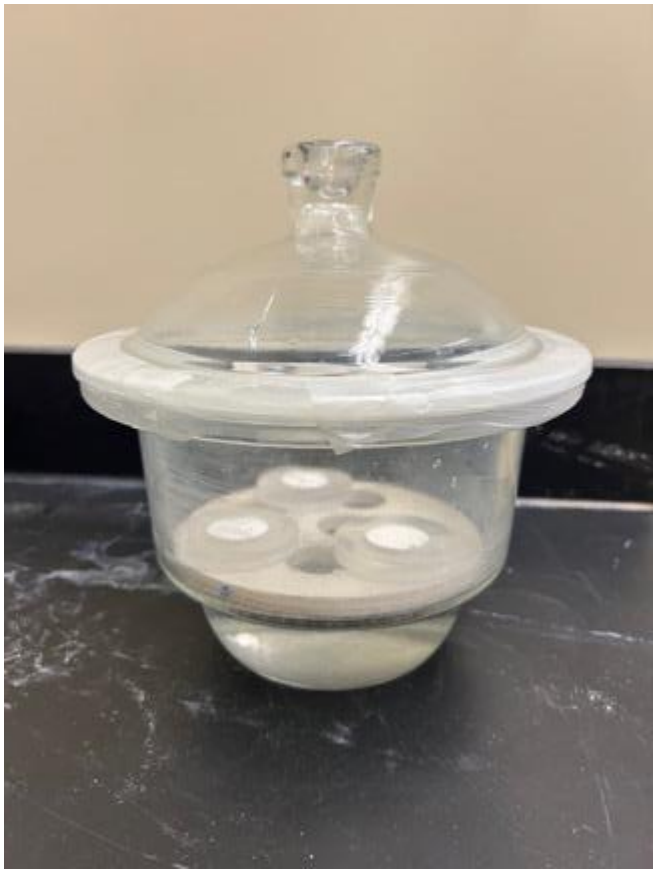

Figure B24. Experimental setup for hydration of samples for Rietveld refinement